

**OBSERVATIONS OF
BREAKING WAVES ON SLOPING BOTTOMS
BY USE OF
LASER DOPPLER VELOCIMETRY**

by
James Eric Skjelbreia

**W.M. Keck Laboratory of Hydraulics and Water Resources
Division of Engineering and Applied Science
CALIFORNIA INSTITUTE OF TECHNOLOGY
Pasadena, California**

OBSERVATIONS OF BREAKING WAVES ON SLOPING BOTTOMS

BY USE OF

LASER DOPPLER VELOCIMETRY

by

James Eric Skjelbreia

Project Supervisor:

Fredric Raichlen
Professor of Civil Engineering

Supported by:

National Science Foundation
Grant Numbers MSM83-11374, CEE83-11374
CEE79-12434

W. M. Keck Laboratory of Hydraulics and Water Resources
Division of Engineering and Applied Science
California Institute of Technology
Pasadena, California

©

James Eric Skjelbreia

All Rights Reserved

This thesis is dedicated to the ones who gave me the will to endure its challenge: my sons, Lars and Thor, and my wife, Helga.

ACKNOWLEDGEMENTS

My adviser, Fredric Raichlen, had constant involvement throughout this study and was a guiding influence for the work presented. He was responsible for arranging my support and for suggesting the topic of this thesis; for this, he is gratefully acknowledged.

Members of my thesis committee, Norman Brooks, Tom Caughey, John List, and Ted Wu, each of whom I came to know quite well through their excellent teachings, insightful discussions and joyful friendships, were a tremendous influence on me and helped shape the professional character that I have today. Gentlemen, it was my pleasure to have gotten to know each of you and to have had you all on my thesis committee; thanks for everything, you will not be forgotten.

Persons which might be categorized as support personnel for this study, but were really much more than that, at least to me, include: Elton Daly, Rich Eastvedt, Joe Fontana, Rayma Harrison, Gunilla Hastrup and Joan Mathews. How lucky it was to have had you around, and yes, it's true, this thesis would not have been possible without you. Thank you, thank you all.

Friends, each that know who they are, were so very important to me. All contributing to this thesis in one form or another and to a greater or lesser extent. Sharing good times and bad, we survived;

thanks for the help in pulling me through.

Caltech, I'd like to thank you, if such a thing is possible. You're a very special place and such a wonderful place to do one's graduate studies. Thank you very much Caltech for all the experiences you have given me.

This study was funded by the National Science Foundation under Grant Numbers MSM83-11374, CEE83-11374 and CEE79-12434.

This report is essentially the thesis of the same title submitted by the writer May 20, 1987 to the California Institute of Technology, in partial fulfillment of the requirements for the degree of Doctor of Philosophy in Civil Engineering.

ABSTRACT

Wave breaking is investigated experimentally by use of laser doppler velocimetry for two cases: a plunging breaker and a spilling breaker. Specifically, emphasis is given to the kinematics at breaking, the early breaking phase, and the turbulent wake generated from wave breaking. A significant contribution is provided on the amplitude behavior for a solitary wave on a beach, as it is the solitary wave that is used to conduct this study. Associated with the use of the solitary wave, a technique of flow field construction by repeated measurement with an LDV is presented.

Four well defined regions of the shoaling-through-breaking solitary wave on a beach are identified and termed according to the wave amplitude behavior within each region. They are: the zone of gradual shoaling, the zone of rapid shoaling, the zone of rapid decay and the zone of gradual decay. The plunging wave case studied exhibited a definite transitional zone, between the previously known $-1/4$ and -1 power laws, following a power law of $-3/5$.

Velocity fields for a plunger and a spiller at the point of breaking are measured and the corresponding acceleration fields are computed for each. The results show good qualitative comparison to those obtained by theoretical approaches, however, no clear mechanism is demonstrated to initiate breaking for the spilling breaker studied.

The existence of counter-rotating vortices, generated from breaking, is established from velocity measurements of the flow taken during the early breaking phase and within the turbulent wake of the plunging breaker studied. The measurements indicate that the size of the vortices are roughly the same as the undisturbed depth at the point of breaking. Turbulent intensities determined within the wake of the plunging breaker illustrate its character and show that level of turbulent intensity does not progressively decrease behind the turbulent source.

TABLE OF CONTENTS

	Page
ACKNOWLEDGEMENTS	iv
ABSTRACT	vi
TABLE OF CONTENTS	viii
LIST OF FIGURES	xi
LIST OF TABLES	xv
1.0 INTRODUCTION	1
1.1 Objectives and Scope of Study	3
2.0 BACKGROUND TO THIS STUDY	5
2.1 The General Nature of the Shoaling Solitary Wave	6
2.2 Kinematics at Breaking	13
2.3 Early Breaking	16
2.4 The Wake	19
3.0 EXPERIMENTAL CONSIDERATIONS	21
3.1 Velocity Measurements	21
3.2 The Choice of Wave Type	24
3.3 The Wave Breaker Classification	25
4.0 EXPERIMENTAL EQUIPMENT AND PROCEDURES	27
4.1 Wave Tank	27

4.2	Data Acquisition and Control	29
4.3	The Wave Generator	31
4.3.1	The Hydraulic System	34
4.3.2	Function Generator	35
4.3.3	Hydraulic System Controller	37
4.3.4	Trajectory Modification Technique	38
4.4	Water Particle Velocity Measurements	41
4.4.1	The Transmitting Optics	45
4.4.2	The Receiving Optics	49
4.4.3	Signal Processing	52
4.4.4	LDV Carriage	52
4.5	Water Surface Measurements	54
4.5.1	The Resistive Wire Wave Gage	54
4.5.2	Photographs	56
4.5.3	Water Mark	58
4.6	Other Experimental Procedures	60
5.0	PRESENTATION AND DISCUSSION OF RESULTS	62
5.1	The Reproducibility of the Generated Wave	67
5.2	The General Nature of the Solitary Wave on a Beach	72
5.2.1	Spilling Breaker	72
5.2.2	Plunging Breaker	78
5.3	Kinematics at Breaking	88
5.3.1	Formation of the Flow Field	88
5.3.2	Spilling Wave	90
5.3.3	Plunging Wave	95

5.4	Counter-rotating Vortices	104
5.4.1	Early Breaking	107
5.4.2	Filtering	111
5.4.3	Vortices in the Wake	117
5.5	Turbulent Intensities in the Wake	124
6.0	CONCLUSIONS AND RECOMMENDATIONS FOR FURTHER STUDY	131
6.1	The General Nature of the Solitary Wave	131
6.2	The Kinematics at Breaking	132
6.3	Counter-rotating Vortices	133
6.4	The Turbulent Wake	133
6.5	Recommendations for Further Study	134
	REFERENCES	136
	LIST OF SYMBOLS	141
	APPENDIX A—CONVERSION FACTORS	143
	APPENDIX B—MEASUREMENT LOCATIONS	144

LIST OF FIGURES

Figure	Page
2.1 Definition Sketch.	5
2.2 Four zones of shoaling-through-breaking.	10
2.3 Wave profiles of a plunging wave on a beach with $h_0=40$ cm, $H_0/h_0=0.2$, and $S=0.019$; (a) after breaking and (b) before breaking.	12
2.4 Sequence of photographs of a plunging wave in its early breaking stage.	18
4.1 Drawing of the wave tank.	28
4.2 Schematic drawing of the data acquisition and control equipment.	30
4.3 Photograph of wave generator.	32
4.4 Drawing of wave paddle wiper blade (after Goring, 1978).	33
4.5 Schematic drawing of the wave function generator.	36
4.6 Circuit diagram of the Hydraulic System Controller.	39
4.7 Wave paddle trajectories; (a) before modification, (b) after modification.	40
4.8 Illustration of the beam geometry for a conventional reference beam LDV.	43
4.9 Illustration of the beam geometry for the LDV used in this study.	44
4.10 Schematic drawing of the LDV's transmitting optics.	46
4.11 Photograph of the LDV's transmitting optics.	47
4.12 Circuit diagram of source for the Bragg cell drivers.	48
4.13 Schematic drawing of the LDV's receiving optics.	50
4.14 Photograph of the LDV's receiving optics.	51
4.15 Photograph of the LDV carriage.	53

Figure	Page
4.16 Drawing of typical wave gage (after Raichlen, 1965).	55
4.17 Circuit diagram for wave gage (after Raichlen, 1965).	55
4.18 Typical wave gage calibration.	57
4.19 Water mark and wave gage measurement.	59
5.1 Initial wave profiles; (a) $h_0=25.0$ cm, $H_0/h_0=0.2$, $S=0.0075$; (b) $h_0=27.65$ cm, $H_0/h_0=0.4$, $S=0.0062$; (c) $h_0=43.25$, $H_0/h_0=0.2$, $S=0.0192$.	64
5.2 Sketches of waves at breaking; (a) spilling breaker, (b) plunging breaker.	66
5.3 Demonstration of the reproducibility of the wave; horizontal and vertical velocity at locations vertically through the depth for the plunging wave at $h/h_0=0.30$.	69
5.4 Demonstration of the reproducibility of the wave; photographs of the plunger breaker.	70
5.5 Ten velocity time series used to show variability after breaking, plunging wave case at $h/h_0=0.17$ and $z/h=-0.67$.	71
5.6 Evolution of a solitary wave on a sloping bottom which breaks as spiller, case 2.	73
5.7 Maximum amplitude variation for a spilling wave, case 2, compared with Saeki <i>et al.</i> (1971).	75
5.8 Wave celerity for a spilling wave, case 2; (a) normalized by the local shallow water wave speed, (b) normalized by the offshore shallow water wave speed.	77
5.9 Maximum amplitude variation for a spilling wave, case 1.	79
5.10 Maximum amplitude variation for a spilling wave, case 1, normalized by the local depth.	80
5.11 Evolution of a solitary wave on a sloping bottom which breaks as plunger.	81
5.12 Maximum amplitude variation for the plunging wave compared with Saeki <i>et al.</i> (1971) and Camfield & Street (1969).	84

Figure	Page
5.13 Maximum amplitude variation, from water mark measurements, for the plunging wave case.	85
5.14 Wave celerity for the plunging wave case; (a) normalized by the local shallow water wave speed, (b) normalized by the offshore shallow water wave speed.	87
5.15 Overall view of flow field of a spilling wave, case 2, at breaking; (a) velocity, (b) acceleration.	91
5.16 Expanded view of flow field near crest of a spilling wave, case 2, at breaking; (a) velocity (b) acceleration.	92
5.17 Horizontal and vertical velocity distribution in the vicinity of the crest for a spilling wave, case 2, at breaking.	94
5.18 Surface elevation measured by a wave gage compared with a photograph of the plunging wave at breaking; $h/h_0=0.30$.	96
5.19 Overall view of flow field of the plunging wave at breaking; (a) velocity, (b) acceleration.	97
5.20 Expanded view of flow field near the crest of the plunging wave at breaking; (a) velocity, (b) acceleration.	98
5.21 Expanded view of flow field near the crest of the plunging wave at breaking; (a) velocity, (b) acceleration.	99
5.22 Expanded view of flow field near the crest of the plunging wave at breaking; (a) velocity, (b) acceleration.	100
5.23 Horizontal and vertical velocity distribution in the vicinity of the crest for the plunging wave at breaking.	103
5.24 Illustration of the counter-rotating vortices in the breaking tongue of a plunging wave.	105
5.25 Velocity vector rotation for various paths through counter-rotating vortices.	106
5.26 Velocity time series in the after breaking region of the plunging wave, $h/h_0=0.25$ and $z/h=-0.04$.	108

Figure	Page
5.27 Velocity fluctuations due to the presence of counter-rotating vortices in breaking tongue of the plunging wave.	110
5.28a Example of filter performance, $N_w=15$.	114
5.28b Example of filter performance, $N_w=35$.	115
5.28c Example of filter performance, $N_w=59$.	116
5.29 Illustration of vortices in plunging wave after breaking; (a) quasi-steady bore, (b) early breaking.	117
5.30 Velocity traces in the after breaking region of the plunging wave, $h/h_0=0.17$ and $z/h=-0.94$; (a) measured horizontal velocity, (b) bandpassed horizontal and vertical velocities, (c) cumulative vector angle rotation from filtered velocity signals.	119
5.31 Velocity traces in the after breaking region of the plunging wave, $h/h_0=0.21$ and $z/h=0.19$; (a) measured horizontal velocity, (b) bandpassed horizontal and vertical velocities, (c) cumulative vector angle rotation from filtered velocity signals.	120
5.32 Velocity traces in the after breaking region of the plunging wave, $h/h_0=0.21$ and $z/h=-0.54$; (a) measured horizontal velocity, (b) bandpassed horizontal and vertical velocities, (c) cumulative vector angle rotation from filtered velocity signals.	122
5.33a Turbulence intensity in the wake of the plunging wave $h/h_0=0.21$, line plot representation.	126
5.33b Turbulence intensity in the wake of the plunging wave $h/h_0=0.21$, gray scale representation.	127
5.34a Turbulence intensity in the wake of the plunging wave $h/h_0=0.19$, line plot representation.	129
5.34b Turbulence intensity in the wake of the plunging wave $h/h_0=0.19$, gray scale representation.	130

LIST OF TABLES

Table	Page
5.1 Wave parameters and type of measurement made.	62
5.2 Breaking parameter for this study.	67
5.3 Estimates of l_v .	123
B.1 Wave parameters.	144
B.2 Wave gage location coefficients.	145

CHAPTER 1

INTRODUCTION

One of Nature's most spectacular displays is the phenomenon of wave breaking—ubiquitous in our lakes, oceans and along our shorelines. For most people, mention of the breaking wave brings to mind the prominent overturning of a plunging wave and the seemingly chaotic splash and spray that ensue. There is, however, a range of breaker types, each type with its, at least conceptually, distinct character. Galvin (1972) introduced descriptive terms to characterize the breaker types as follows:

- Spilling* A broken water surface appears at the wave's crest and spills down the front face of the wave.
- Plunging* The upper portion of the wave's front face overturns and a jet impinges on the surface towards the leading base of the wave.
- Collapsing* The wave begins to overturn, somewhat like the plunging wave, then suddenly collapses on itself in relatively shallow water.
- Surging* There is no significant disturbance to the wave profile except for the broken water surface at the shoreline.

We proceed down the above list of breaker types with decreasing offshore energy density of the incoming wave and with increasing beach slope. While breaker types serve a useful conceptual purpose as idealizations, real breakers may exhibit characteristics of more than one distinct type. The types of breakers most studied are the spiller

and the plunger, both of which can occur in deep or shallow water.

The aesthetics of the breaking event have delighted and intrigued man for generations. This delight and intrigue are also accompanied by scientific and engineering concern; wave breaking is currently at the focus of many efforts directed towards a better understanding of the phenomenon. Knowledge of the flow in the breaking wave is of great importance, not only for the obvious need to compute wave loading on offshore and coastal structures, but also because wave breaking is central to nearly all coastal processes. Despite noteworthy advances in both theoretical and experimental studies, scientists and engineers alike still have only a vague understanding of the fundamental nature of the breaking wave.

At the most elementary level, why waves break, may be understood from a physical point of view. As a wave propagates up a beach, its energy density, at some instant, exceeds a critical value when the wave can no longer carry that level of energy density forward and must dissipate energy; it does this by breaking. Breaking dissipates organized wave energy through the generation of currents and turbulence. The steepness of a beach controls the rate at which energy density increases; this helps to explain why waves break differently on different beaches. Still, knowing why waves break and why they are different does not explain how they break. What is the mechanism which causes breaking, and what are the details of the flow at and after breaking? The answers to these questions are far from complete.

Cokelet (1977) points out that the majority of work done on breaking waves have considered either before breaking, or after the development of a quasi-steady bore, when the flow is more amenable to theoretical and experimental study. He also makes very clear the lack of knowledge between these two regions. Svendsen *et al.* (1978), recognizing the importance of this region, termed it the *outer breaking zone*. In this region, the wave undergoes a very rapid and drastic transition in form, when organized wave energy is lost to currents and to turbulence. The catastrophic event results in a large amplitude decrease and the generation of a turbulent wake behind the breaking front. Over the range of spilling and plunging breakers, these processes can be quite different.

1.1 *Objectives and Scope of Study*

By use of modern instrumentation and the development of new techniques, this study was intended to investigate some aspects of the underlying nature of wave breaking. In particular, emphasis was placed on three main areas which we list as:

- The kinematics at breaking.
- The existence of counter-rotating vortices, generated during early breaking.
- The turbulent wake.

The goals, set forth above, demand by their nature, investigation of the flow in the breaking wave within the region of rapid transition just after breaking, the region of breaking where the least is known.

Two types of breaking waves were studied: the spiller and the plunger. These breakers were created by generating solitary waves on a sloping bottom. The goal of this study was not to study solitary waves on a beach in particular; the solitary wave was used as a tool to look at wave breaking. The solitary wave offered a means of examining wave breaking without contamination from previous breaking events, as would be the case for periodic waves.

To conduct this study, some novel experimental equipment was designed and constructed, including: a laser doppler velocimeter, a wave function generator, and a hydraulic system controller. The laser doppler velocimeter had the capability to measure water particle velocity throughout most the flow, including the region above the undisturbed free surface, and to within approximately 1 mm of horizontal boundaries. The wave function generator and the hydraulic system controller made it possible to generate reproducible waves, a necessity for this study.

The background for this study and a discussion of the work of others are presented in Chapter 2. Chapter 3 discusses some important experimental concerns which one must consider before embarking on a study such as this. Chapter 4 describes the experimental equipment and procedures. The observations and results of this study are presented in Chapter 5. Finally, the conclusions and suggestions for further study are given in Chapter 6.

CHAPTER 2

BACKGROUND TO THIS STUDY

This chapter provides background to this study and discusses the works of others. Most previous studies of breaking waves have investigated periodic waves on beaches; this study is restricted to solitary waves on a beach. It is the accepted belief (Peregrine 1979), however, that the basic details of wave breaking throughout the spectrum, from deep water breakers to a solitary wave breaking on a beach, are similar for a given breaker type.

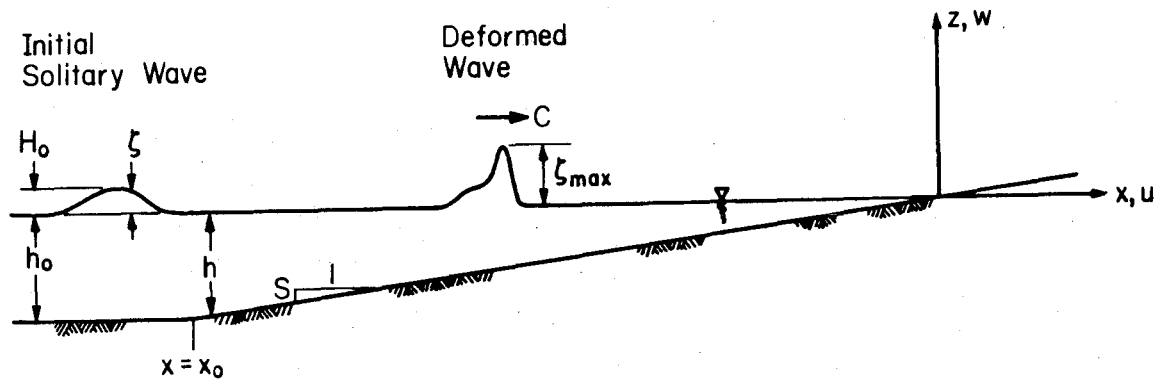


Fig. 2.1 Definition Sketch.

Fig. 2.1 is the definition sketch to be used in the discussion of this chapter and for the results to be presented in Chapter 5. The initial wave is a solitary wave and is defined on a horizontal bottom with depth, h_0 , (which, at times, will be termed the offshore depth)

and initial amplitude, H_0 . The wave propagates up an inclined bottom (often referred to as a beach) of slope S . The surface elevation is denoted by ζ and the maximum amplitude of the wave on the beach by ζ_{\max} . On the beach, the depth is denoted by h and the celerity of the wave by C . The spatial coordinates are measured from the shoreline with x horizontal and positive in the shoreward direction and z vertical and positive upward. The corresponding velocity components in the x and z directions are u and w respectively. The toe of the beach where the bottom changes from the horizontal to the sloping bottom is located at x_0 .

It should be noted that at some points in this chapter and others, the words *spilling breaker* and *plunging breaker*, are used when actually referring to the wave before it breaks but will eventually break in the manner described.

2.1 *The General Nature of the Shoaling Solitary Wave*

As mentioned earlier, the primary objective of this study is the investigation of the general flow behavior of a wave from the point of breaking and shoreward into the region of rapid transition. A brief discussion, however, will also be given of the nature of solitary wave as it evolves in propagating up a beach.

The study of solitary waves originated with Russell (1838, 1845); he found an empirical formula for the propagation speed of the solitary wave and also observed that breaking occurred when the amplitude was approximately the same as the depth on which it propagated. Theoretical considerations of a solitary wave on a bottom of decreasing depth were first studied by Boussinesq (1872). From his equations for a solitary wave on a constant depth, he wrote the relations for the amplitude of the wave and its volume in terms of its energy, E , and the depth, h_0 ; they are respectively:

$$H_0 = \frac{3}{4} E^{2/3} h_0^{-1} \quad , \quad (2.1)$$

and,

$$Q = 2 E^{1/3} h_0 \quad . \quad (2.2)$$

From these equations he realized that if the wave, now on a beach, were to retain its solitary wave character, then it could not simultaneously conserve both energy and volume. Based on Bazin's (1865) observations of solitary waves on a beach, his impression was that the wave apparently retained its basic solitary wave shape and suggested that its energy was mostly conserved, and thus its amplitude should vary with the inverse of the depth (i.e., $\zeta_{\max} \sim h^{-1}$) in accordance with Eq. 2.1. He also suggested that the excess volume of the shoaling solitary wave would be continuously carried away in the form of a reflected wave. Boussinesq's simple reasoning does indeed predict the approximate behavior of a solitary wave on a beach under certain circumstances, but the problem is a bit more complicated than he probably imagined — as we shall see later.

The behavior of the solitary wave near and through breaking cannot currently be described by any theoretical means; however there are predictions for its behavior before breaking. Miles (1980) gives an excellent review of studies on the shoaling solitary wave, a few of which we would like to mention here. Often used to describe the maximum amplitude behavior is an equation of the form:

$$\zeta_{\max} \sim h^{-a}. \quad (2.3)$$

Most theoretical results predict the value of a to be $1/4$ or 1 , but an exception is that due to Leibovich & Randall (1973) who obtained a value of $1/3$. The value of $1/4$ corresponds to Green's Law, which, for periodic waves, can be derived from the linearized equations of motion and is based on the conservation of energy flux. It also arises in equations for a solitary wave on a beach when dispersion is neglected, as shown by Johnson (1973) and Shuto (1973). The result, $a=1$ can be directly related to the energy conservation arguments used by Boussinesq and, as Miles (1980) points out, has been rediscovered by many, usually by more elaborate means.

Shuto (1973,1974) predicts the value of a to be either $1/4$ or 1 , according to the relative importance of the terms in the equation he considered. He compared his results to the experimental work of Ippen & Kulin (1954,1955), Kishi & Saeki (1966), Street & Camfield (1966), Camfield & Street (1969), and Saeki *et al.* (1971). He found that, for sufficiently small amplitude and sufficiently large slope, the $1/4$

trend in a prevailed, and that, on sufficiently small slopes, the $a=1$ trend would eventually appear. Shuto also noted that, in the data of Camfield & Street, there is a narrow region just before breaking that the value of a exceeds 1.

Studies of the maximum amplitude variation after breaking include: the experiments of Kishi & Saeki (1966), Camfield & Street (1967) and Saeki *et al.* (1971). Only Saeki *et al.* recognized distinct regions after breaking (surprisingly though, not before breaking) where the amplitude of the wave exhibited similar trends. They did not discuss the rates of decay in these regions although such rates may be deduced from their data. These show a very rapid amplitude decay just after breaking which is the result of organized wave energy being lost to the generation of turbulence. This region is the analog of the *outer region* of Svendsen *et al.* (1978) in their description of periodic waves just after breaking. At some point after breaking when the amplitude has diminished sufficiently, Saeki *et al.*'s data show a less gradual decay corresponding to Svendsen *et al.*'s *inner region*.

It appears that there are at least four distinct regimes for the amplitude behavior of the shoaling-through-breaking solitary wave. These regimes shall be termed, the *zone of gradual shoaling* (ZGS), the *zone of rapid shoaling* (ZRS), the *zone of rapid decay* (ZRD), and the *zone of gradual decay* (ZGD). Fig. 2.2 shows schematically these four zones. The limits of each zone are defined by the parameter a . The ZGS can be thought of as the region along the beach, before breaking,

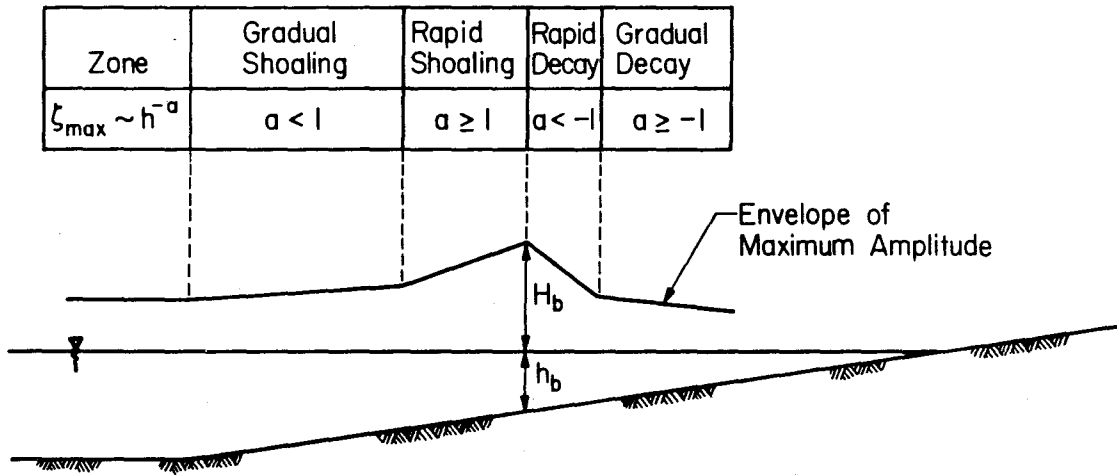


Fig. 2.2 Four zones of shoaling-through-breaking.

where the growth in ζ_{\max} proceeds at a lesser rate (in a power sense) than the rate at which the depth decreases. Similarly the ZRS can be thought of as the region where ζ_{\max} increases at an equal or faster rate than the rate at which the depth decreases. After breaking, ζ_{\max} 's rate of decrease in the ZRD proceeds faster than the rate of decrease in the depth and in the ZGD at an equal or slower rate than the decrease in the depth. The line depicting the envelope of the maximum wave amplitude in the Fig. 2.2 is by no means meant to be exact, but rather, it gives an indication of the behavior for a solitary wave on a beach in each regime. The width of each zone may vary (or not even exist at all) according to the beach slope, S , and the initial amplitude ratio, H_0/h_0 . The parameters H_b and h_b are the maximum amplitude of the wave and the depth of water at breaking respectively. The results of the wave amplitude behavior for this study

and those of others will be presented in Chapter 5.

The behavior of a solitary wave on a beach is conveniently illustrated by wave profiles measured as time series at various locations in a wave tank with a sloping bottom. Fig. 2.3 shows such time series for a solitary wave which breaks as a plunger; the parameters which characterize the initial wave and the beach are $h_0 = 40$ cm, $H_0/h_0 = 0.2$, and $S = 0.019$. For a solitary wave which changes in form as it propagates up a beach, the time series will not strictly be the same as instantaneous spatial profiles, but they will be similar. The measurement location of each time series is given as the ratio of the depth at the measurement point to the offshore depth. Time is shown running positive from right to left, which gives the profiles the appearance of spatial profiles measured in x . In Fig. 2.3b are wave profiles measured before breaking. At $h/h_0 = 0.62$ we see that the wave still has somewhat of a solitary wave shape but a tail, emerging from the rear of the wave, is obvious. This tail is not the reflected wave imagined by Boussinesq; it is traveling shoreward. One convinces himself of this by examining the profiles in Fig. 2.3b. A characteristic, drawn connecting the points of each profile where the amplitude of the tail is nearing zero, show that the tail is moving in the same direction as the wave. The celerity of the wave is nearly constant between $h/h_0 = 0.62$ and 0.43 and hence the tail has roughly doubled in length over that span. As the tail grows, the maximum amplitude increases and the wave steepens. The wave eventually breaks at $h/h_0 \sim 0.30$. There is currently some controversy over the nature of

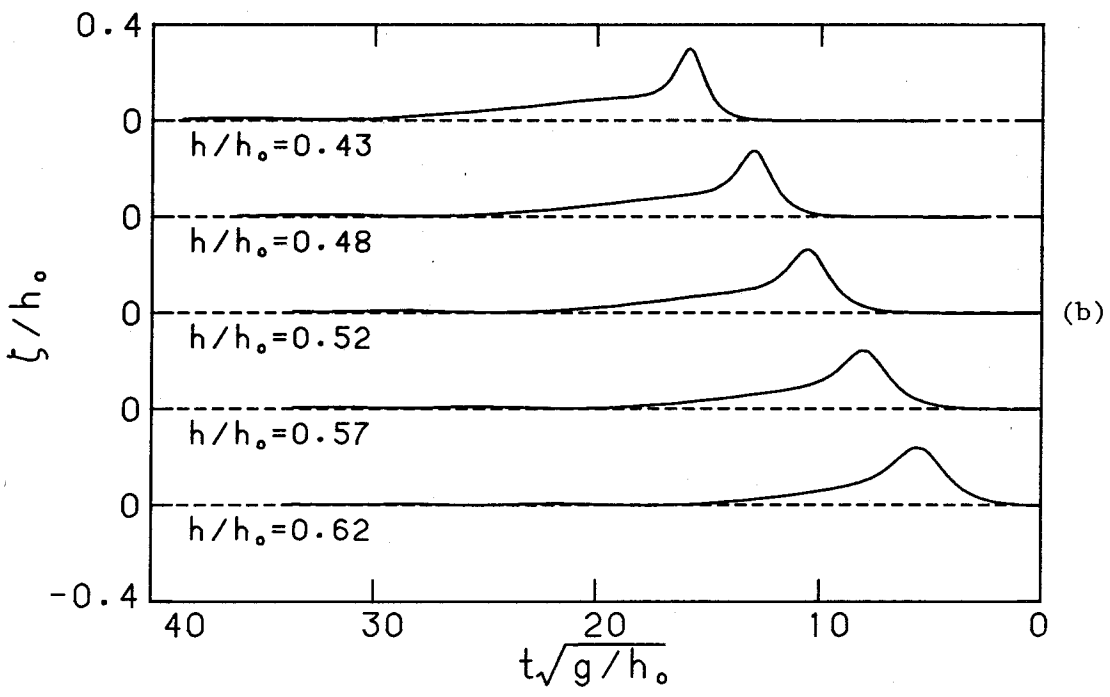
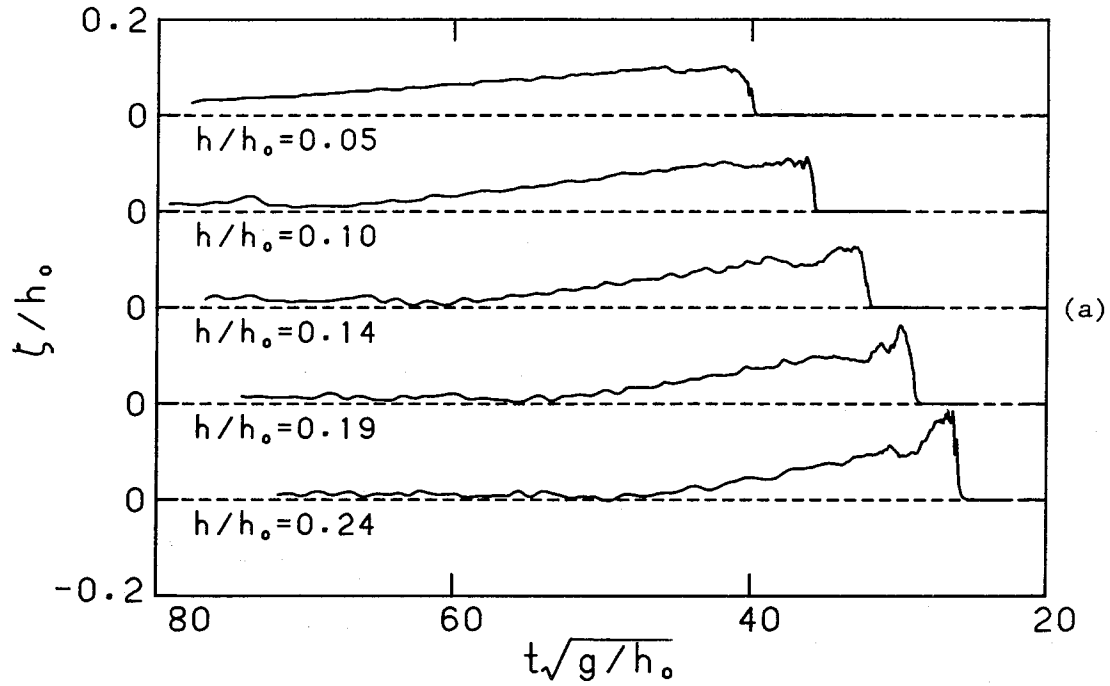


Fig. 2.3 Wave profiles of a plunging wave on a beach with $h_0=40$ cm, $H_0/h_0=0.2$, and $S=0.019$; (a) after breaking and (b) before breaking.

the tail which travels with the wave and the reflected wave. Smyth (1984) and Knickerbocker & Newell (1985) provide more discussion. The reflected wave is not dismissed here, in fact, some results from this study may support its existence.

Profiles taken after breaking in the ZGD are shown in Fig. 2.3a. The wave celerity throughout this figure cannot be considered constant and hence comparisons of horizontal lengths, based on the presented time series, cannot be made. We do, however, see the basic features of the wave after breaking. The wave in this region takes the form of a triangular wave and is referred to as a quasi-steady bore. The wave amplitude can be seen to decay as it propagates up the beach.

It should be noted that, although Fig. 2.3 describes the typical behavior of a solitary wave on a beach, there will be differences for differing wave and beach parameters. For instance, a solitary which breaks as a spiller does so at an amplitude ratio that is less than a plunger and the relative size of the tail is smaller.

2.2 *Kinematics at Breaking*

There is currently some uncertainty as to the mechanism which causes breaking and whether the mechanism differs between breaker types. An often used criterion for breaking is that the fluid velocity at the crest exceeds the celerity of the wave. This is obvious for plunging breakers since the fluid in the jet which is ejected from the

front face of the wave must exceed the speed of the wave's advance. This interpretation of the flow at the crest exceeding the celerity of the wave and that this being the mechanism for breaking may actually be too simplistic; at breaking the meaning of wave celerity is somewhat nebulous owing to the rapidly changing shape of the wave. Peregrine (1983) mentions the possibility of a Rayleigh-Taylor instability as a mechanism for breaking. This will occur if fluid accelerations directed into the fluid near the surface exceed the component of acceleration due to gravity normal to the surface. Because the Rayleigh-Taylor instability can lead to a highly convoluted surface, which is certainly the case for a breaking wave, it is an attractive hypothesis. Numerical studies, such as those by Peregrine et al. (1980) and Vinje & Brevig (1980), have begun to give a picture of the flow at breaking, but they have yet to be verified by experimental measurements.

The only known velocity measurements of the flow in a solitary wave at breaking are those of Ippen & Kulin (1954,1955). They looked at waves on slopes of 0.023 and 0.065 which produced spilling and plunging breakers respectively. Their goal was to ascertain whether there are differences in the flow field for the two cases; from the information they obtained they could not conclude any. They encountered difficulties in inferring velocities in the flow from finite-sized droplets tracked by consecutive movie frames taken 1/20 s apart. The results of both cases indicated that the water particle velocities at the crest did not exceed the measured celerity of the

wave. These results give a very interesting overall view of the flow in the wave at breaking, but, given the crude means by which they were obtained, they must be considered limited.

There are a number of experimental studies in which velocity measurements were made in periodic waves at breaking. Cokelet (1977) and Peregrine (1983) list many of these studies, but here and in the next section we will concern ourselves with the more recent ones. Generally the results of past studies were often limited due to inadequate instrumentation. This situation is changing with the development of new measuring techniques such as the ones used in this study (see Chapter 4).

A clearer picture of the flow in a wave at breaking is beginning to emerge. Studies such as those of Divoky *et al.* (1970) and Van Dorn (1978) have presented profiles of maximum horizontal velocities at breaking measured at locations throughout the depth. These profiles can be misleading in the sense that they are not synoptic for a given instant; we now know that there is a phase lag at the crest of a breaker as we move down in the flow from top to bottom. As a result, the maximum velocities through the depth, at the location of breaking, do not occur simultaneously. This phase lag has been observed by Thornton *et al.* (1976), Kjeldsen & Myrhaug (1980), and Flick *et al.* (1981). Recent work by Easson & Greated (1984) using laser doppler velocimetry (LDV) and computer control have measured flow velocities in the crest of a breaking wave. Their limited results show the phase lag

and compare reasonably well, in a qualitative sense, with the numerical results of Cokelet (1979). The impression one gets from previous studies is that little is known about the kinematics at breaking and there is still much to be learned.

2.3 *Early Breaking*

Numerical models, such as those by Longuet-Higgins & Cokelet (1976) and Vinje & Brevig (1981), can describe the motion of a breaking wave up to the time the jet impinges on the forward face of the wave; predictions about subsequent events cannot be made. When the over-turning jet from a plunging breaker impinges on its forward face, a splash-up occurs. The splash-up may be in the form of a jet and can itself produce a subsequent splash-up. Miller (1976) observed a single breaking event which produced a series of five successive splash-ups. The generation of the series of splash-ups is very rapid and quickly advances forward ahead of the original wave crest. This advance of splash-ups will be termed the *breaking tongue*, since it has the appearance of a tongue shooting forward from the crest. In addition to the air trapped by the over-turning jet, there is a considerable amount of air entrained by each of the splash-ups. Initially the *breaking tongue* appears to be surface-limited with little depth penetration. Eventually the leading edge of the tongue becomes the new wave front and air bubbles are evident at some depth below the surface.

Fig. 2.4 shows various stages of the early breaking phase. This sequence of photographs was made using six waves of slightly differing amplitude and was not done under the controlled conditions used for the experiments of this study. The splash-up can be seen in Fig. 2.4a,b,c and the rapid advance of the *breaking tongue* in Fig. 2.4c,d,e. The original crest of the plunger is indicated by an arrow in Fig. 2.4d,f. The leading edge of the *breaking tongue* will subsequently become the front of the quasi-steady bore. The time between Figures 2.4a and 2.4f is approximately 0.5 s (illustrating the short life of the breaking tongue) and the original crest translates forward the equivalent of roughly 5 depths, measured at the point of breaking.

While the fluid motions during the early phase of breaking in the aerated breaking tongue are not obvious, Peregrine (1983) and Basco (1985) speculate and give their thoughts on the process. Measurements of any type are extremely limited in this upper area of breaking because of experimental difficulties due to air entrainment. Jansen (1986) has been successful in using a fluorescent tracer-particle technique to visualize the flow in the *breaking tongue*, and found that the trajectories of the tracers were surprisingly smooth in this region. It is generally thought that a series of co-rotating vortices (first suggested by Miller, 1976) are generated by the splash-ups. Large shear between the vortices would then give some account of the large amplitude decay just after breaking. The suggestion that co-rotating vortices are generated during early breaking, raises the question: where does the net increase in angular momentum originate,

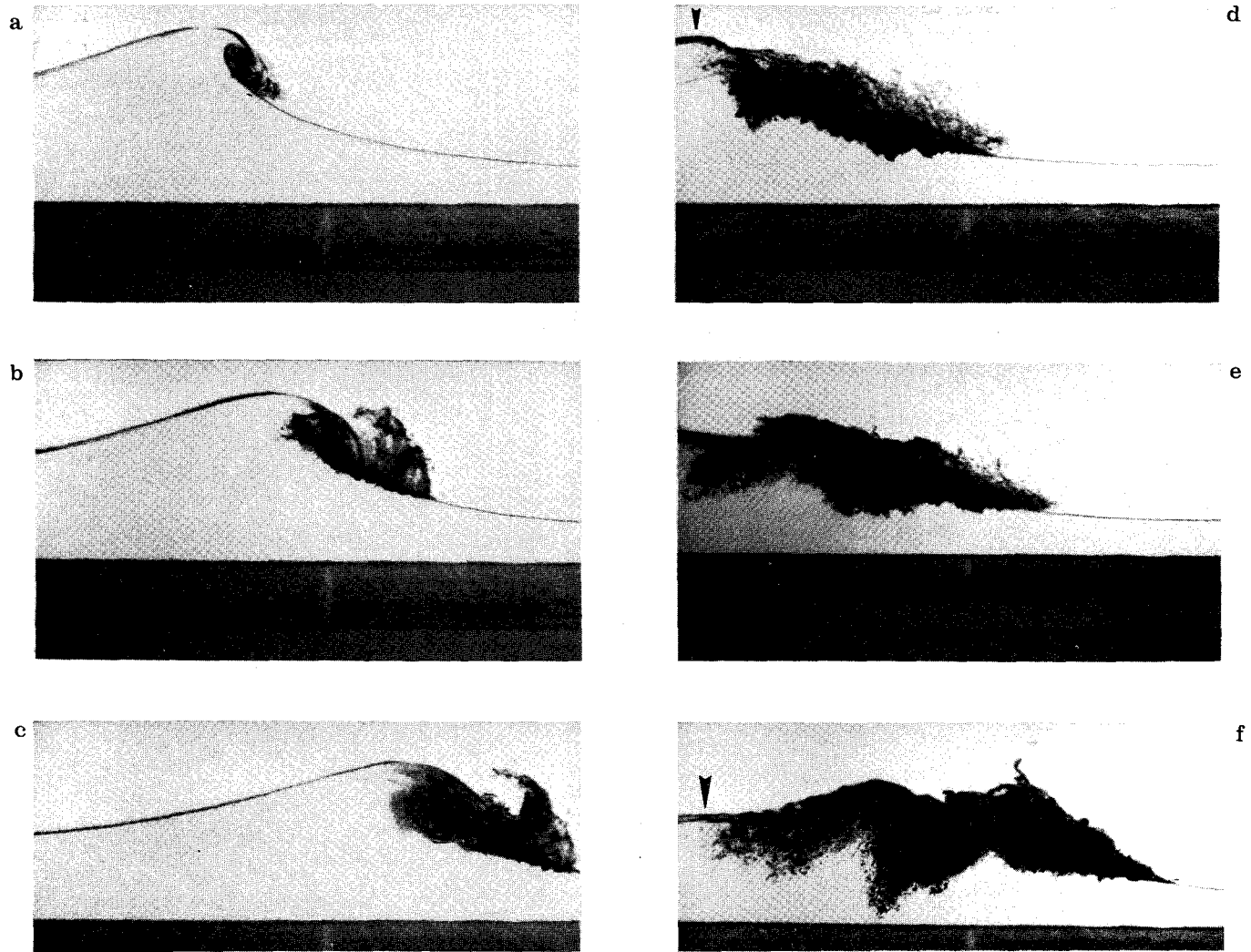


Fig. 2.4 Sequence of photographs of a plunging wave in its early breaking stage.

when there are no apparent external moments acting on the fluid? As we shall see in Chapter 5, the vortices generated during early breaking are actually counter-rotating.

2.4 *The Wake*

A turbulent wake forms behind the highly turbulent *breaking tongue* generated during the early breaking phase. Initially the source of turbulence for the wake is the vorticity contained within the tongue. As the wave front approaches the end of the ZRD, the *breaking tongue* itself and the rollers it contains become part of the wake. The scale of the turbulence in the wake depends on the type breaker: smaller for gentle spillers and larger for strong plungers.

Banner & Phillips (1974) used flow visualization to show the existence of a wake behind a steady breaker created in a steady stream with an obstacle placed in the flow. Peregrine & Svendsen (1978) also used flow visualization to look at the wake created by a breaking wave on a beach, they pointed out the similarity of the wake to both a mixing layer and a two dimensional wake. Subsequent velocity measurements of the turbulent region behind the *breaking tongue* have verified its two dimensional wake character. Duncan (1978,1981) towed a hydrofoil in a still fluid, thus creating a steady spilling breaker that moved with the hydrofoil at the same speed; from photographs he measured the movement of flow tracers to infer flow velocities. He obtained information about the velocity distribution in the wake and

its growth: Battjes & Sakai (1981), in a similar experiment but with a fixed hydrofoil and a moving stream, used the LDV technique to clearly show the two dimensional wake nature to the rear of the stationary breaking front. Stive (1980) also used the LDV technique to show the two dimensional wake nature in the ZGD of a spilling beaker on a beach.

To date, the velocity measurements in the wake region of a breaker have been made for relatively gentle breakers. In Chapter 5 we show some measurements in the wake of a plunging breaker.

CHAPTER 3

EXPERIMENTAL CONSIDERATIONS

Here we review some of the more important aspects involved in conducting this type of study. The topics covered are central to the design of a good experimental investigation on breaking waves. They include: velocity measurements, choice of wave, and class of breaker.

3.1 *Velocity Measurements*

The flow situation in a breaking wave is very complex and it is a great challenge to obtain flow measurements which may have some usefulness. For instance, at breaking the free surface is rapidly changing and becomes highly distorted with a near-vertical front face. A Eulerian measurement of the velocity in this type of flow will contain very high frequencies and thus would require a measuring instrument with a sufficiently high frequency response. A Lagrangian type measurement would require sufficiently small tracer particles with a density very near to that of the water used due to the large velocity gradients and the high fluid accelerations. Ideally, the instrument of choice for the velocity measurements would give us a "snapshot" of the flow and would have the following features:

1. High spatial resolution $\sim h/100$.
2. High frequency response $\sim 100\sqrt{g/h}$.
3. Operative in aerated flows.
4. Operative above the undisturbed free surface.

where for a study on breaking waves, h might be the undisturbed water depth at breaking.

Such an instrument, as described above, currently does not exist and possibly will never be realized. An instrument that approaches our "ideal" instrument, at least in concept, are photographs of flow tracers, i.e. streak photography. With good optics and good tracers, one can make considerable accomplishments with this type of instrument. There are trade offs, however. To approach the spatial resolution and the frequency response we desire, the field of view of the flow would be limited. A problem arising with the aerated regions (a problem for all types instruments) in the flow, regardless of the type of illumination, is that the air bubbles bend and distort the light emitted or scattered from the flow tracers. This diminishes the spatial resolution as well as the accuracy of flow measurement. Also, with photographs one has to "take what you get", meaning the flow tracers may not be nicely distributed in the region of interest. The above reasons lead us away from using photographs to measure flow velocities in this study, however, it is believed that this technique should not be completely disregarded. A companion technique to photographs is holography, which has the capability to measure flow velocity in three dimensions. Although considerably more complicated, arguments for and against holography can be considered in a similar light as photography.

Relaxing our desire for a *snapshot* of the flow we can consider single point measuring techniques. There are a number of instruments available of this type and can be classified as either intrusive, semi-intrusive or non-intrusive.

Instruments of the intrusive type such as the pitot tube, propeller meter, or hot-film, would, in general, not be suitable for our type of flow measurement. Aside from the fact that this type of instrument disturbs the flow, the major difficulty arises when attempting to make flow measurements above the undisturbed free-surface. Given the finite size of intrusive instruments, it is not easy to construct a probe which will give good spatial resolution in two dimensions. Examples of the semi-intrusive type instrument are the magnetometer and acoustic meter. These types of instruments have poor spatial resolution and it is difficult to obtain two dimensional measurements on small scales.

Most notable of the non-intrusive type instruments is the laser doppler velocimeter (LDV), it has high spatial resolution for two dimensional measurements and high frequency response. The LDV has no problems above the free surface and the extent in which it can probe the flow is a function of the beam geometry. Like all the other instruments, the LDV is plagued by air entrainment in the breaking wave. A single bubble blocking any of the beams can cause signal drop-out.

Based on this review of the available flow measuring instruments the LDV was chosen for this study. The disadvantage of the LDV being able to only measure flow velocities at a single point was overcome by other experimental techniques (see Section 5.1). The design adopted for this study (see Section 4.4) easily allowed for flow measurements as close as 1 mm from a horizontal surface.

3.2 *The Choice of Wave Type*

The best approach, it was felt, to study the fundamental nature of the flow in a breaking wave, was to look at an individual event. In other words, examine the breaking phenomena in a surf zone free of contamination from previous breaking events. Also keeping in mind that the LDV chosen to measure the flow could only do so at a single point, required that the wave should be highly reproducible so that sufficient information could be constructed of the flow by repeated measurements.

It is difficult to perceive of periodic waves, of any type, fulfilling the above mentioned requirements. The leading wave, of a group or train of waves, propagating into still water, tends to be small and of ill-defined character. It is unlikely that the leading wave, or waves, would break in a consistent and reproducible manner, at least to a sufficient accuracy required for this study.

The solitary wave, however, satisfied our requirements in a most elegant way, not just from its intrinsic physical beauty, but more so from the ease and simplicity of generating it and the ability in which its breaking could be controlled. The solitary wave, by proper choice of beach slope and initial amplitude ratio, will exhibit all the characteristics of the types of breakers described in Chapter 1. The notion of using a solitary wave for surf zone investigations is not new; Munk (1949) observed that periodic waves on a beach took on characteristics similar to solitary waves and suggested their use in breaking wave studies. There have been some studies that have utilized the solitary wave to examine wave breaking (e.g. Ippen & Kulin, 1954), but its use has been limited.

3.3 *The Wave Breaker Classification*

The two classes of wave breakers of most concern to engineers are the spilling and plunging breakers. With the intent of this study lying more on the fundamental nature of breaking, it was sought to investigate these two breaker types by "representative" breakers. Information provided by Camfield & Street (1969) defines regions for the various types of breakers for solitary waves for a given beach slope and initial amplitude ratio. Parameters could be chosen to obtain a breaker which was centrally located in its respective region of classification, this is what is meant by "representative."

One should keep in mind, that the descriptive terms, "spiller" and "plunger", are subjective, and that the way a wave breaks for a given set of parameters may vary from facility to facility. Hopefully, with the choice of waves made, some of the important mechanisms have been isolated within the two studied regimes of breaking.

CHAPTER 4

EXPERIMENTAL EQUIPMENT AND PROCEDURES

This chapter describes the experimental equipment and its use in the present investigation. Most of the equipment was designed and specified by the manufacturer using *U.S. Customary* units, the experimental data, however, was taken using *Système International* (SI) units. Being that it is awkward to have a consistent set of units, for both the experimental equipment and data, the choice of units used to describe a particular piece of equipment will be based on the unit used to design or specify it; if the description is not in SI units, the appropriate value in SI units will follow immediately in parentheses. A table of conversion factors between unit systems is provided in Appendix A.

4.1 Wave Tank

Experiments for this study were conducted in the 40 meter precision tilting flume located in the W.M. Keck Hydraulics Laboratory, shown schematically in Fig. 4.1. The flume was modified to be used as a wave tank with the installation of a piston type wave generator at the end of the tank. The tank has a length of 130 ft. (39.6 m) and a cross-section of 43 in. (1.09 m) wide by 24 in. (0.61 m) deep. The tank is constructed with a stainless steel plate bottom and with plate glass walls, 0.5 in. (1.3 cm) thick in 5 ft. (1.53 m) sections. Wave gage carriages are supported above the tank by two stainless steel

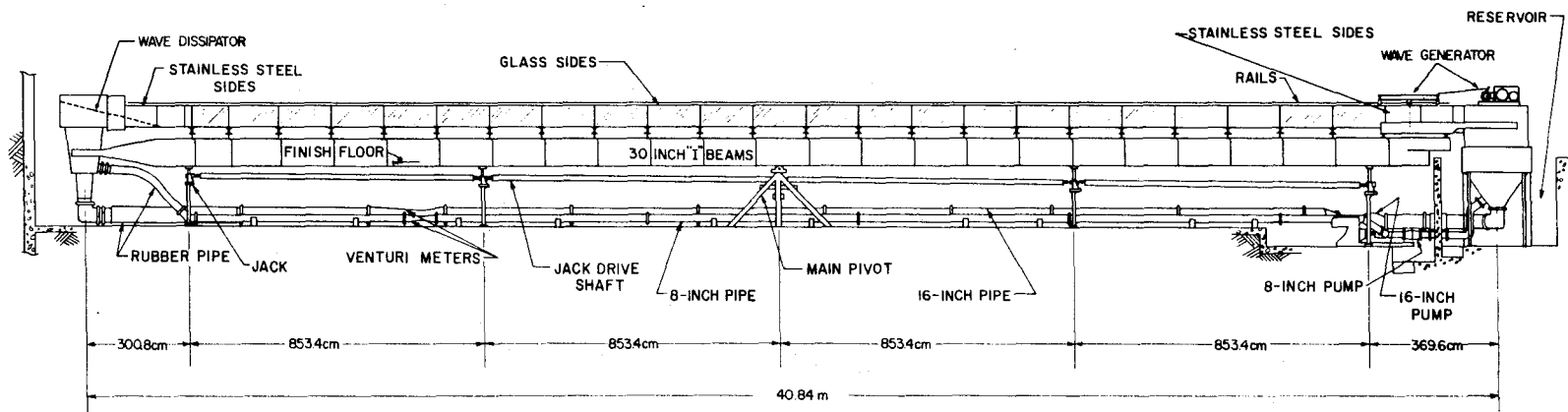
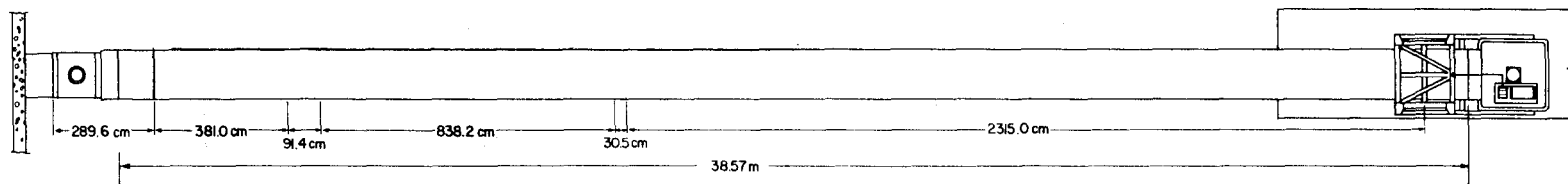


Fig. 4.1 Drawing of the wave tank.

rails, 1.5 in. (3.8 cm) diameter, mounted to the tank with adjustable studs at 2 ft. (0.61 m) intervals. When the tank is horizontal these rails are parallel to the water surface to within ± 0.3 mm. The tank is pivoted at the center and supported on either side of the pivot by two power driven screw-jacks and can be tilted from the horizontal to a maximum slope of approximately 1 vertical to 50 horizontal. Other details of the tank are more completely described by Vanoni *et al.* (1967).

4.2 Data Acquisition and Control

A Digital Equipment Corporation (DEC) LSI-11/23 based minicomputer running RT-11 V4.0 was used to acquire data and to control some of the experimental equipment. The complete system consisted of a DEC LSI-11/23 CPU; 256K bytes RAM; a DEC DLV11-J RS-232 serial line interface; a DEC DRV11-J 64 line parallel interface; an A/D-D/A board (Datel Model ST-LSI) which included 32 A/D inputs, 2 D/A outputs, and 4 TTL control lines; and a 30M byte winchester and 1M byte floppy storage system (Data System Design Model 880/30). The central role of the minicomputer is shown in Fig. 4.2. With the exception of the graphics display and the other computers, all the equipment in the figure will be discussed in the following sections of this chapter.

The graphics display, which was actually an oscilloscope (Hewlett Packard Model 1715A), was driven by the minicomputer through its X, Y, and Z axes inputs. The graphics display provided a qualitative view of

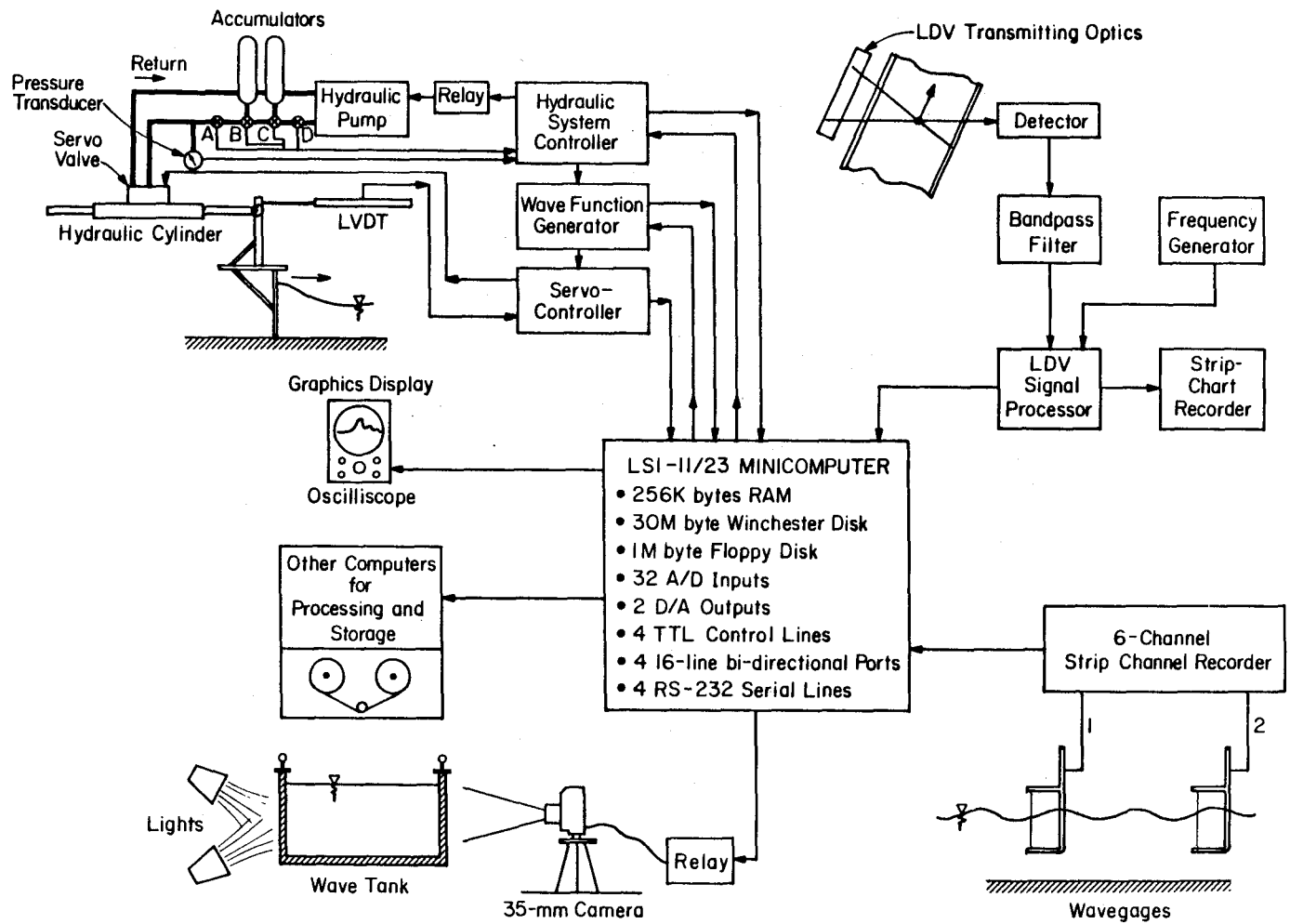


Fig. 4.2 Schematic drawing of the data acquisition and control equipment.

the LDV output (see section 4.4) and wave gage signals. Data were transferred to other computers via diskette or an RS-232 serial line. The other computers, used for analysis and plotting, were a VAX 750, a VAX 730 and a PDP-11/24.

4.3 *The Wave Generator*

A piston type wave generator was installed at one end of the of the wave tank, a photograph of it is shown in Fig. 4.3. The piston generator was made of 0.25 in. (6.4 mm) thick aluminum plate with dimensions slightly smaller than the inside dimensions of the wave tank. To prevent leakage around the paddle, during wave generation, windshield wiper blades were installed at the bottom and the two sides of the paddle. A drawing of the wiper blade arrangement is shown schematically in Fig. 4.4. The paddle was mounted to an aluminum frame, which rode on a carriage supported by 1.5 in. (3.8 cm) rails that traveled on linear ball bushings. The paddle carriage was actuated by a hydraulic cylinder (Miller Model DR-77B) attached to the wave tank frame. Hydraulic accumulators were mounted to the side of the wave tank with the feed and return lines running underneath and along the length of the tank to its central pivot, there, flexible tube connections were made to lines fixed to the floor of the building that continued to run to the Laboratory's hydraulic pump.

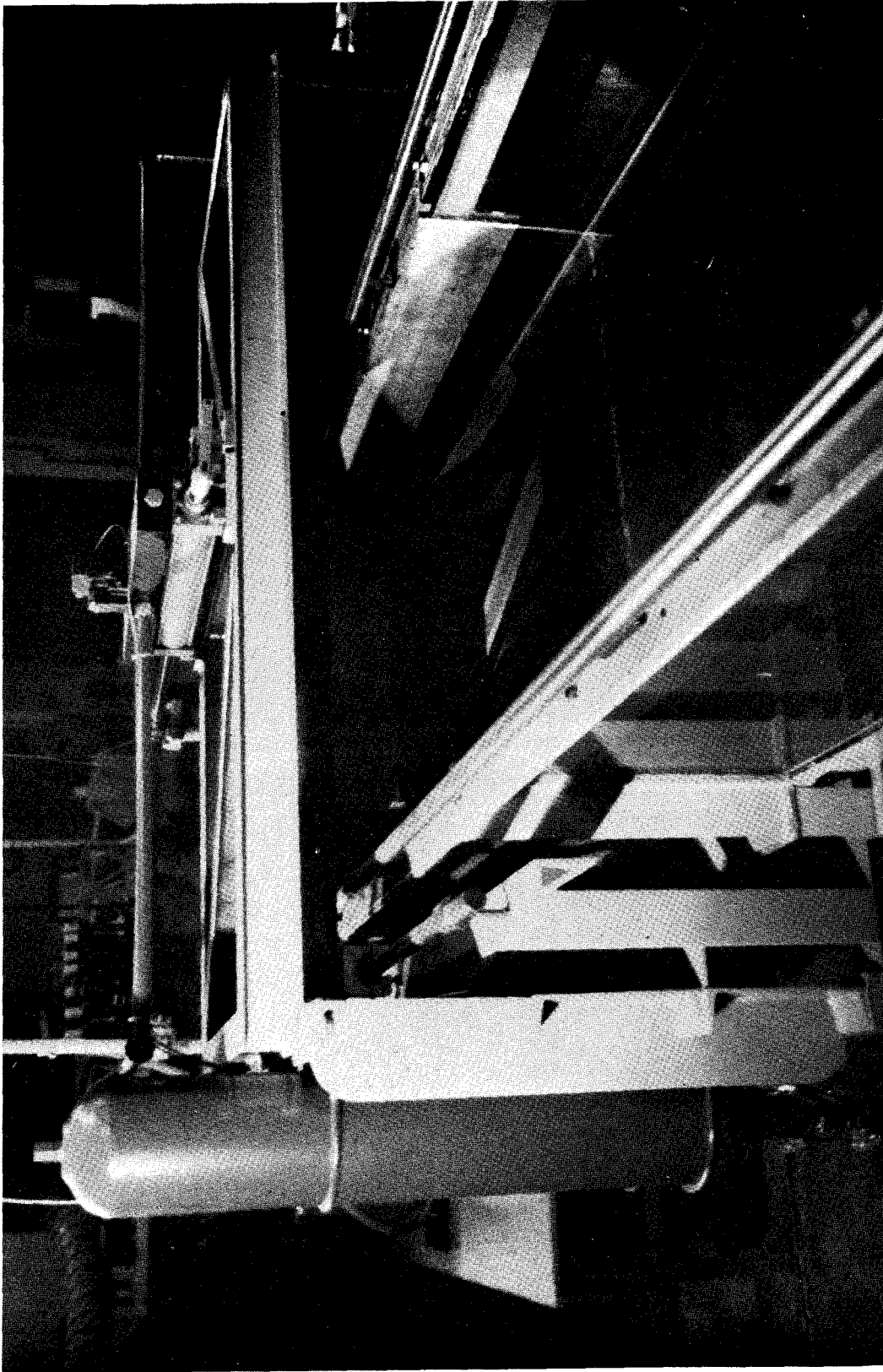


Fig. 4.3 Photograph of wave generator.

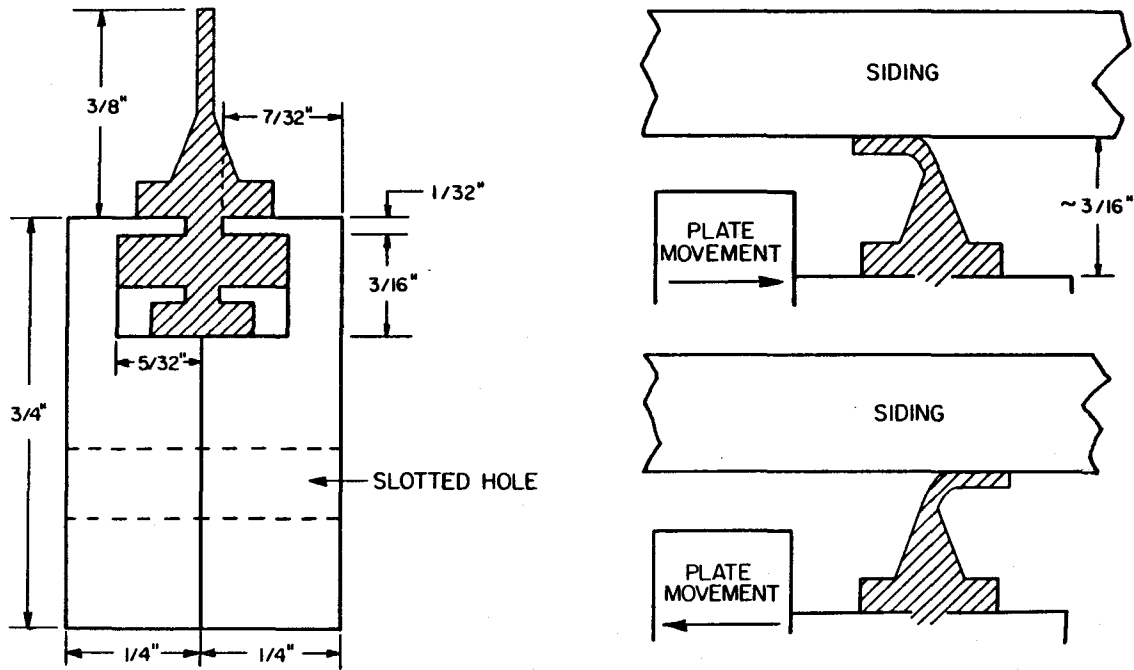


Fig. 4.4 Drawing of wave paddle wiper blade (after Goring, 1978).

The position of the paddle was monitored by an LVDT (Linearly Variable Differential Transformer, Collins Model LMT-811T41) mounted along the side and attached to one end of the hydraulic piston. The control of the hydraulic piston was handled by a servo-valve (Moog Model 72-103) and servo-controller (Moog Model 82D300). Specific details of the hydraulic system, and its control, follows.

4.3.1 *The Hydraulic System*

The complete hydraulic system consists of an oil reservoir, a pump, a filter, an unloading valve, a check valve, three accumulators, a second filter, a hydraulic cylinder, and the servo-valve mentioned earlier. The pump used to charge the accumulators is a Denison constant volume axial-piston type, rated at 2.9 gpm ($0.00018 \text{ m}^3/\text{s}$) at 3000 psi ($20,000 \text{ kN/m}^2$). It was supplied by a 40 gal. (0.152 m^3) reservoir and powered by a 7.5 hp (5.6 kW) electric motor operating at 1800 rpm (30 s^{-1}). A filter, with nominal particle rating of $5 \mu\text{m}$, followed by an unloading valve and a check valve, was located downstream from the pump. The by-pass pressure of the unloading valve was set to 2500 psi ($17,000 \text{ kN/m}^2$); the check valve prevented a reverse flow through the pump from the pressurized system when the pump was not operating. Two 7 gal. (0.027 m^3) accumulators provided operating conditions between 2500 psi ($17,000 \text{ kN/m}^2$), corresponding to the maximum pressure allowed by the unloading valve, and 450 psi ($3,000 \text{ kN/m}^2$), corresponding to the precharged pressure of the accumulators. The servo-valve directed the flow to either end of the hydraulic cylinder and was rated at 60 gpm ($0.0037 \text{ m}^3/\text{s}$) for 40 mA applied current to the valve. One 1.5 gal. (0.0057 m^3) accumulator was installed downstream of the servo-valve to reduce hydraulic transients should rapid changes occur in the flow rate through the servo-valve. A check valve, activated at 14 psi (100 kN/m^2), was placed before the oil reservoir to keep the return line full.

4.3.2 *Function Generator*

The analog command signal fed to the servo-controller was provided by a microprocessor controlled function generator, which was built around the Intel SKD-85 system design kit. A schematic of the function generator and the devices connected to it are shown in Fig. 4.5. Operation of this kit is completely described in the SKD-85 User's Manual (1978). Added to the basic SKD-85 was a 12 bit D/A converter (Datel model DAC-6912B) and 8K bytes of static RAM for storing the wave paddle trajectory. This combination provided 4096 discrete voltage levels for an output time series of 4096 points. The function generator was interfaced with the minicomputer used for this study via a parallel interface (DEC model DRV11-J). Wave paddle trajectories, in digital form, were loaded into the function generator from the minicomputer, after which, the function generator could operate in an unattended mode.

The function generator could be operated manually or by remote control by either the Hydraulic System Controller (see next section) or the minicomputer; only the command signal from the Hydraulic System Controller was used for the present study.

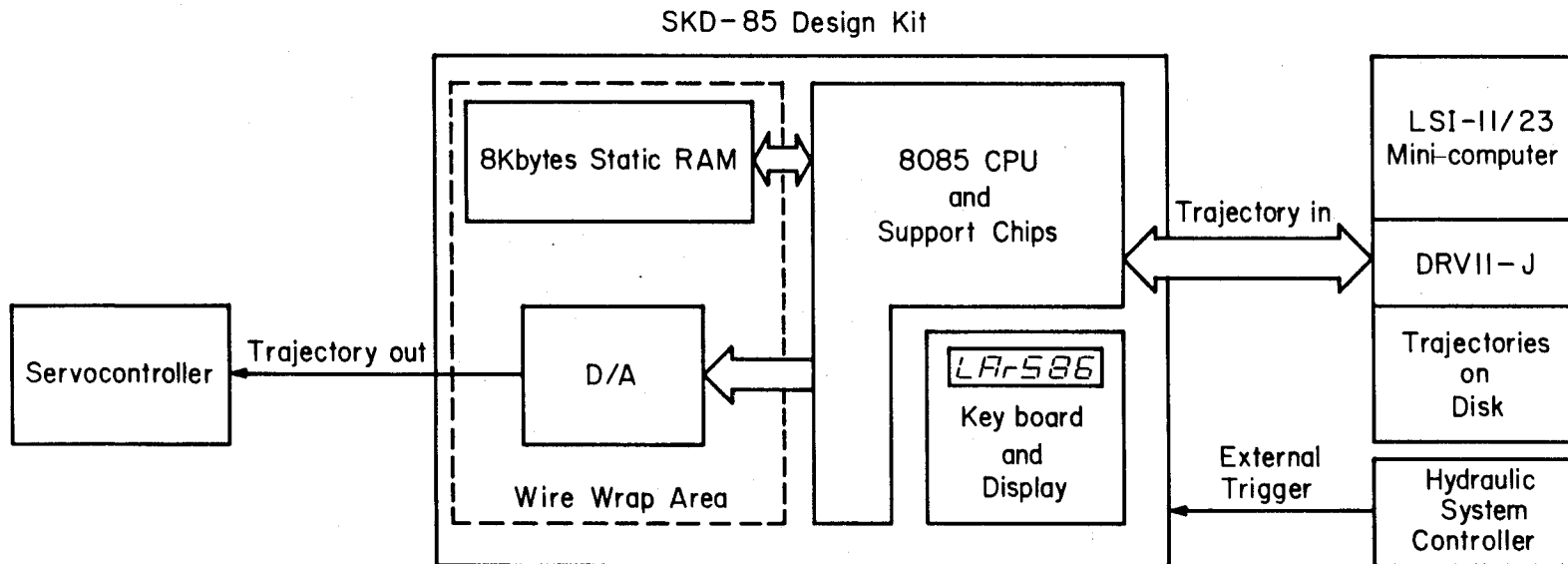


Fig. 4.5 Schematic drawing of the wave function generator.

4.3.3 *Hydraulic System Controller*

The Hydraulic System Controller (HSC) handled the functions of: charging the accumulators to a preset pressure on demand, providing an output command signal when a preset pressure was reached after charging, and automatic charging of the accumulators if the pressure dropped below a preset level.

The transfer function, relating the input signal provided to the servo-controller to the actual trajectory of the wave paddle, was a function of the pressure in the accumulator at the time of generation. As mentioned in Chapter 3, to conduct this study it was essential to have a means of generating reproducible waves; this was the primary function of the HSC. The HSC could receive a command signal, either manually from its front panel or by the minicomputer, to start the hydraulic pump and charge the accumulators to 2250 psi (15,500 kN/m²) at which point it would stop the pump. Monitoring the pressure, when it dropped to 2000 psi (14,000 kN/m²) (due to the dither on the servo-valve), the HSC issued a trigger signal to the function generator and the minicomputer, provided the trigger was armed (either manually from the HSC front panel or by the minicomputer). The trigger signal instructed the function generator to initiate the output of the trajectory to the servo-controller, and simultaneously, was also used by the minicomputer to synchronize the timing of the data acquisition with wave generation. The HSC monitored the pressure in the accumulators at all times, if the pressured dropped below 500 psi (3,500 kN/m²), the HSC started the pump and charged the accumulators to

2250 psi (15,500 kN/m²) at which point it stopped the pump.

The HSC would operate the pump only if all four valves in the hydraulic system were open. The state of the valves was determined by mercury switches attached to the handle of each valve. Pressure in the accumulators was monitored by a resistance type pressure transducer (Bourns Model 726) rated at 4000 psi (27,500 kN/m²) with a repeatability of $\pm 0.15\%$. The hydraulic pump was controlled by relays attached to the manual operation buttons for the pump. A electronic component schematic of the HSC is shown in Fig. 4.6, all external components of the system are shown inside dashed lines.

4.3.4 Trajectory Modification Technique

The overall transfer function of the generation system resulted in there being differences existing between the desired plate trajectory and the actual trajectory produced as shown in Fig. 4.7a. In this figure, ξ is the position of the wave plate, ξ_{\max} is the maximum excursion of the plate, t is time and T is the period over which a signal was applied to move the plate. Because it was impractical to determine the transfer function of the system, a technique was developed to modify the trajectory signal supplied to the servo-controller so that the desired trajectory would be obtained. The technique consisted of a simple feedback loop that took the difference of the actual trajectory from the desired trajectory and added it to the input signal of the servo-controller. This feedback loop did not

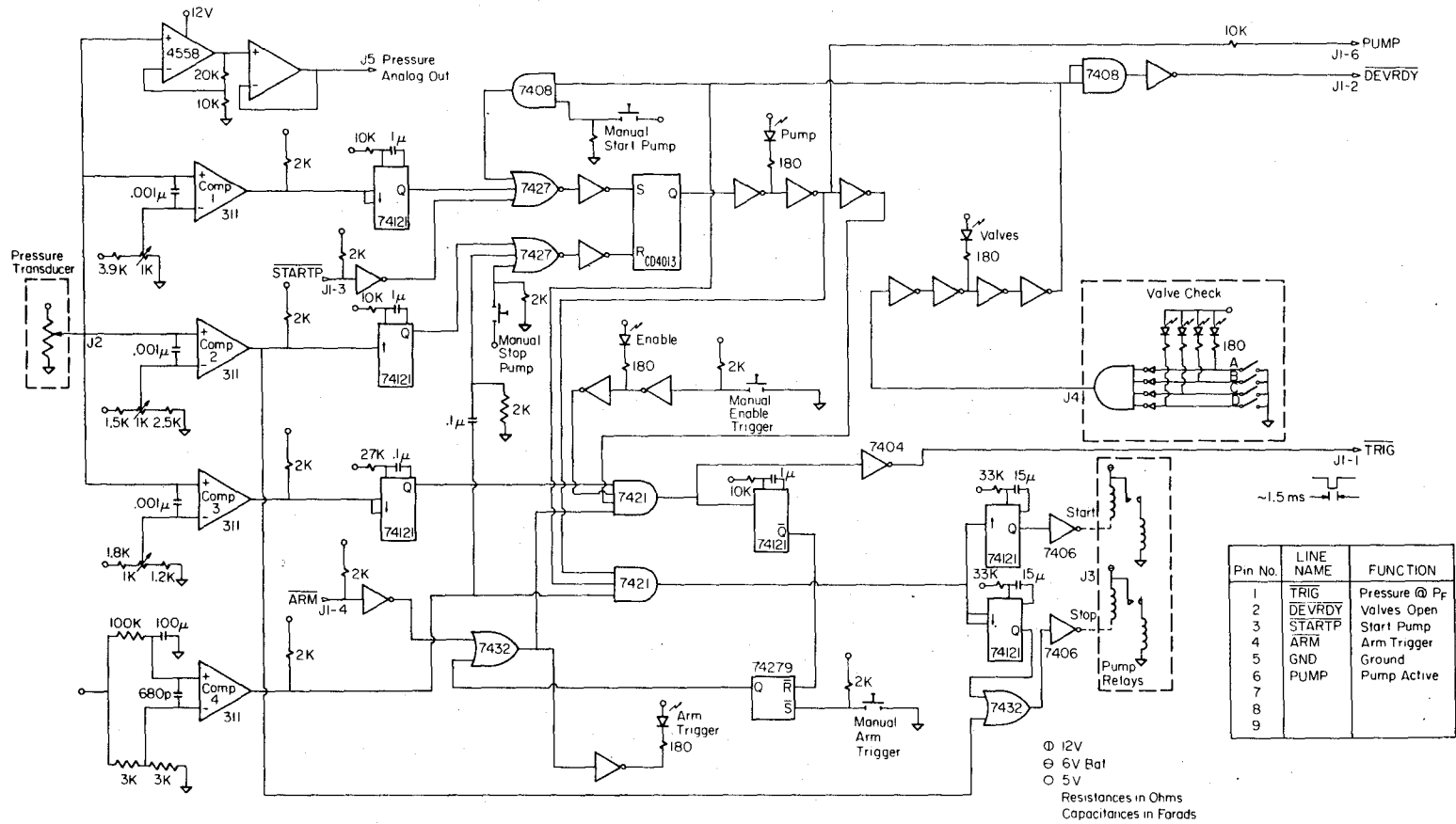


Fig. 4.6 Circuit diagram of the Hydraulic System Controller.

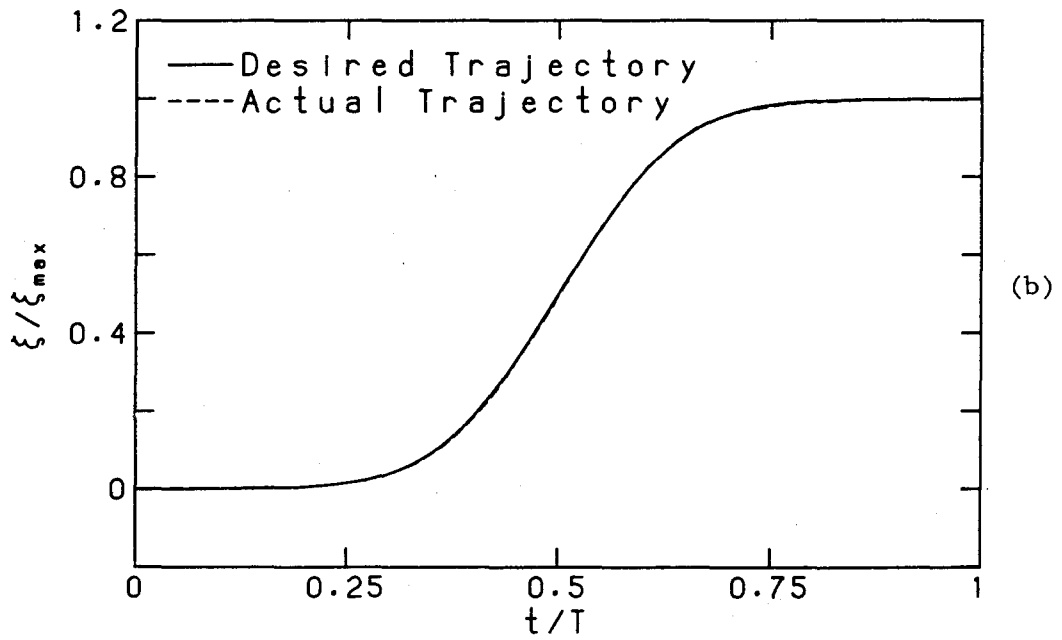
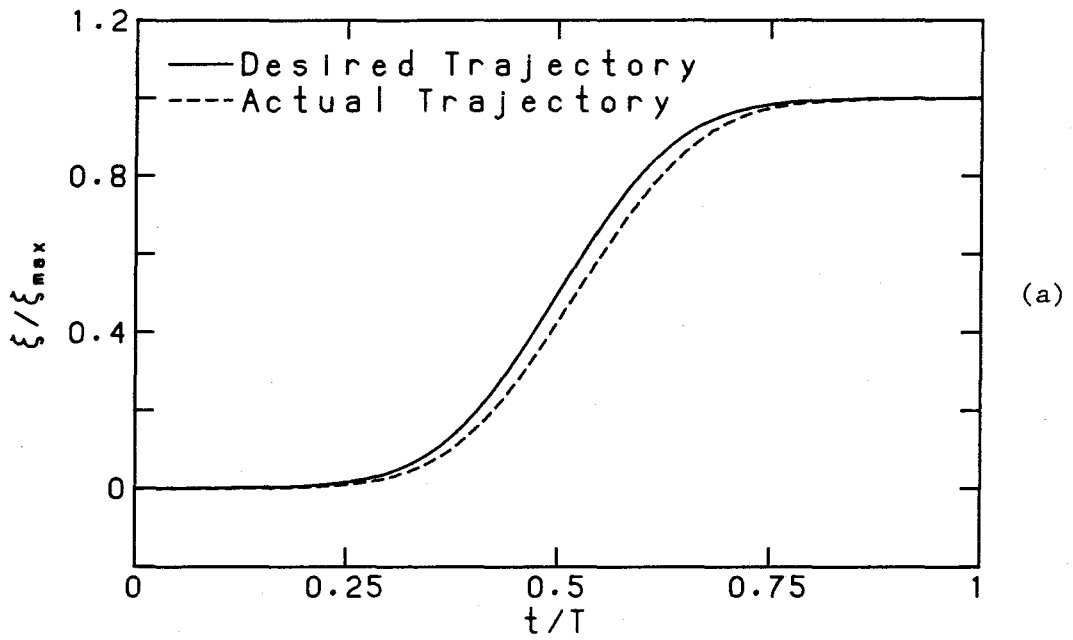


Fig. 4.7 Wave paddle trajectories; (a) before modification, (b) after modification.

operate in real time, instead, a signal was fed to the servo-controller and the output was monitored with the minicomputer. A new updated signal was computed and loaded into the wave function generator. This process was repeated until the desired convergence was achieved.

We can represent this process as follows: let $D(t)$ represent the desired trajectory and $I_k(t)$ and $O_k(t)$ the k^{th} input and actual output trajectory respectively. The technique is then described by:

$$I_k(t) = I_{k-1}(t) + (D(t) - O_{k-1}(t)) \quad k = 1, n \quad , \quad (4.1)$$

where,

$$I_0(t) = D(t). \quad (4.2)$$

Typically, for the type of trajectories used in this study, three iterations were sufficient to obtain good agreement with the desired trajectory as shown in Fig. 4.7b.

4.4 Water Particle Velocity Measurements

The water particle velocity was measured using a non-conventional reference beam laser doppler velocimeter (LDV); non-conventional in the sense that, the beams did not intersect within the flow (the first demonstrated LDV, designed by Yeh & Cummins 1964, was of similar type). The particular design of the LDV used had the advantage of allowing two velocity component measurements near boundaries, i.e., the free surface and the bottom. The LDV employed frequency shifting, allowing for directional velocity measurements. Details of the LDV, developed for

this study; follow. No attempt will be made to explain the principles of LDV operation; excellent references for this are the textbooks by Durst *et al.* (1983) or Drain (1979).

The advantages of the present LDV are best illustrated by comparing it to a conventional two component reference beam LDV. The axial view of the conventional LDV in Fig. 4.8 shows what might be a typical arrangement of the reference and scattering beams as they appear on, say, the glass-water interface of the wave tank. These beams all focus to a single point within the flow and form the measurement volume of the instrument as seen in the side view. There is some minimum distance that the conventional LDV can approach the free surface or any fixed boundary which spans the entire width of the flow since all beams must be encased in the water (the fate of the scatter beam is of no importance after it passes the measuring point, since it is no longer needed). The minimum distance is a function of the beam geometry and the width of the tank, approximately 5 cm for a 1 m wide tank.

The present LDV passes a scattering beam and a single reference beam across the wave tank and operates in one of two modes: an *upward looking* mode or a *downward looking* mode. In the upward looking mode, the reference beam is located below the scattering beam, and, in the downward looking mode, it is above the scattering beam, as shown in Fig. 4.9. On the receiving side of the LDV, the reference beam is mixed with the scattered light from the measurement point, then

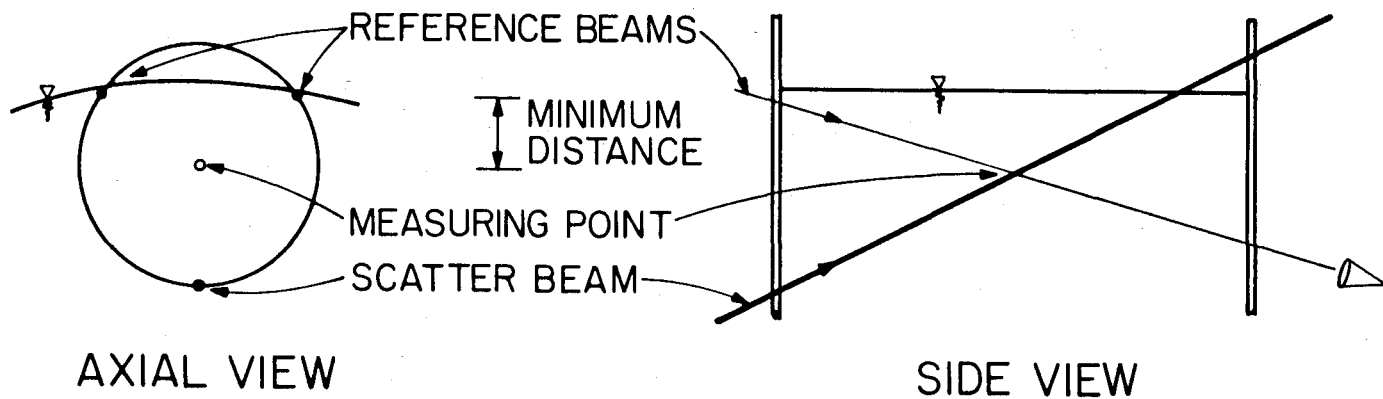


Fig. 4.8 Illustration of the beam geometry for a conventional reference beam LDV.

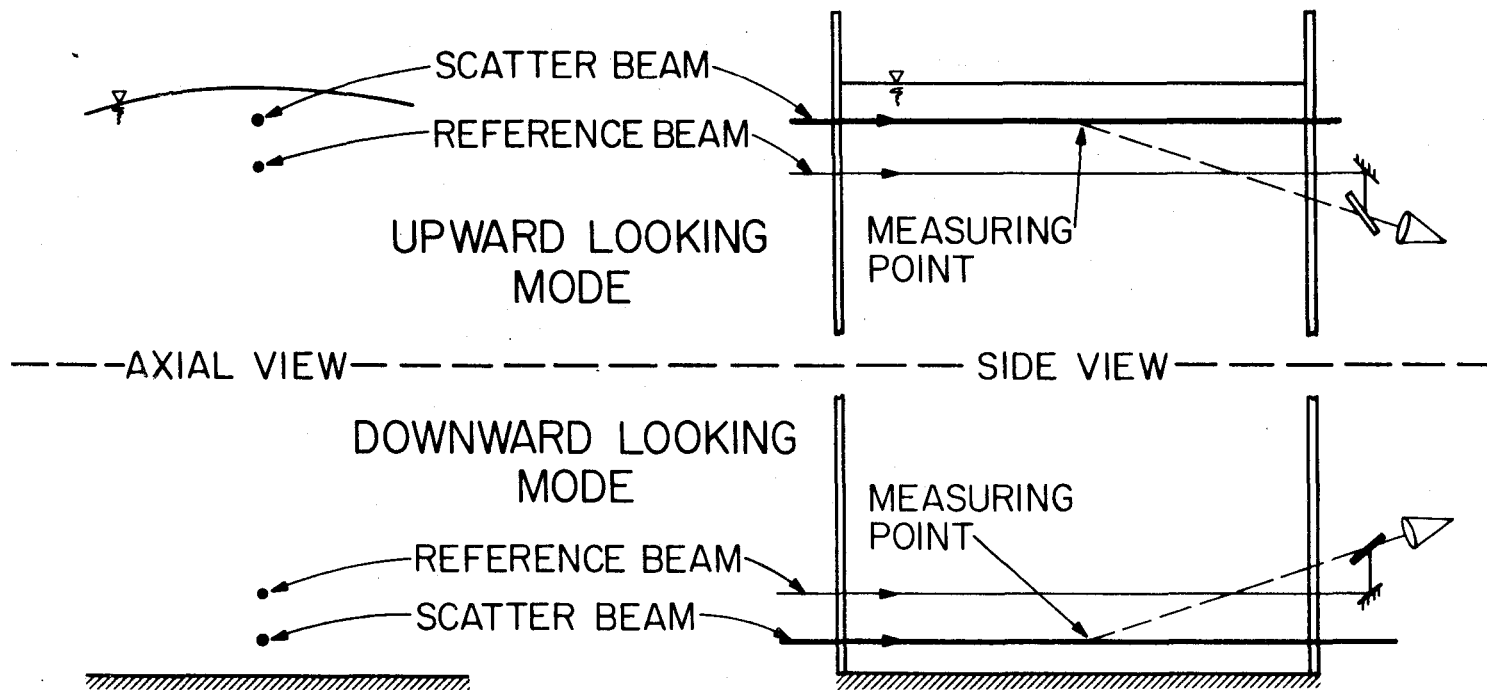


Fig. 4.9 Illustration of the beam geometry for the LDV used in this study.

heterodyned on a photodetector. This arrangement allowed measurements to within 1 mm from a horizontal surface. The LDV used in the present investigation was arranged in two principal units: the transmitting optics and the receiving optics; a discussion of each follows.

4.4.1 *The Transmitting Optics*

The transmitting optics of the LDV are shown schematically in Fig. 4.10, and consist of: two 5 mw He-Ne velocimeter and alignment lasers (Melles Griot Model 05-LHP-151), a polarizing beamsplitter, Bragg cells (Coherent Model 305), a focusing lens, a 1 to 4 beamsplitter (made up discrete beamsplitters and mirrors), right angle prisms, and mirrors. All optical components have a precision of $\lambda/8$ or better. A photograph of the transmitting optics is shown in Fig. 4.11.

The scatter and reference beams are created from the velocimeter laser; the originating laser beam is split by a polarizing beamsplitter, then, each beam is passed through separate Bragg cells, focused and directed into the flow. The polarizing beam splitter offered a convenient means of distributing the laser power between the scatter beam (~90%) and reference beam (~10%) since the laser was cylindrical and could be rotated in its mount. Each Bragg cell was driven by an RF power amplifier (EIN Model 300L) that used the circuit shown in Fig. 4.12 as its source. One Bragg cell was driven at 40 MHz and the other at 40.5 MHz, for a net frequency shift of 500 KHz between the scatter and reference beams. The reference beam could be directed

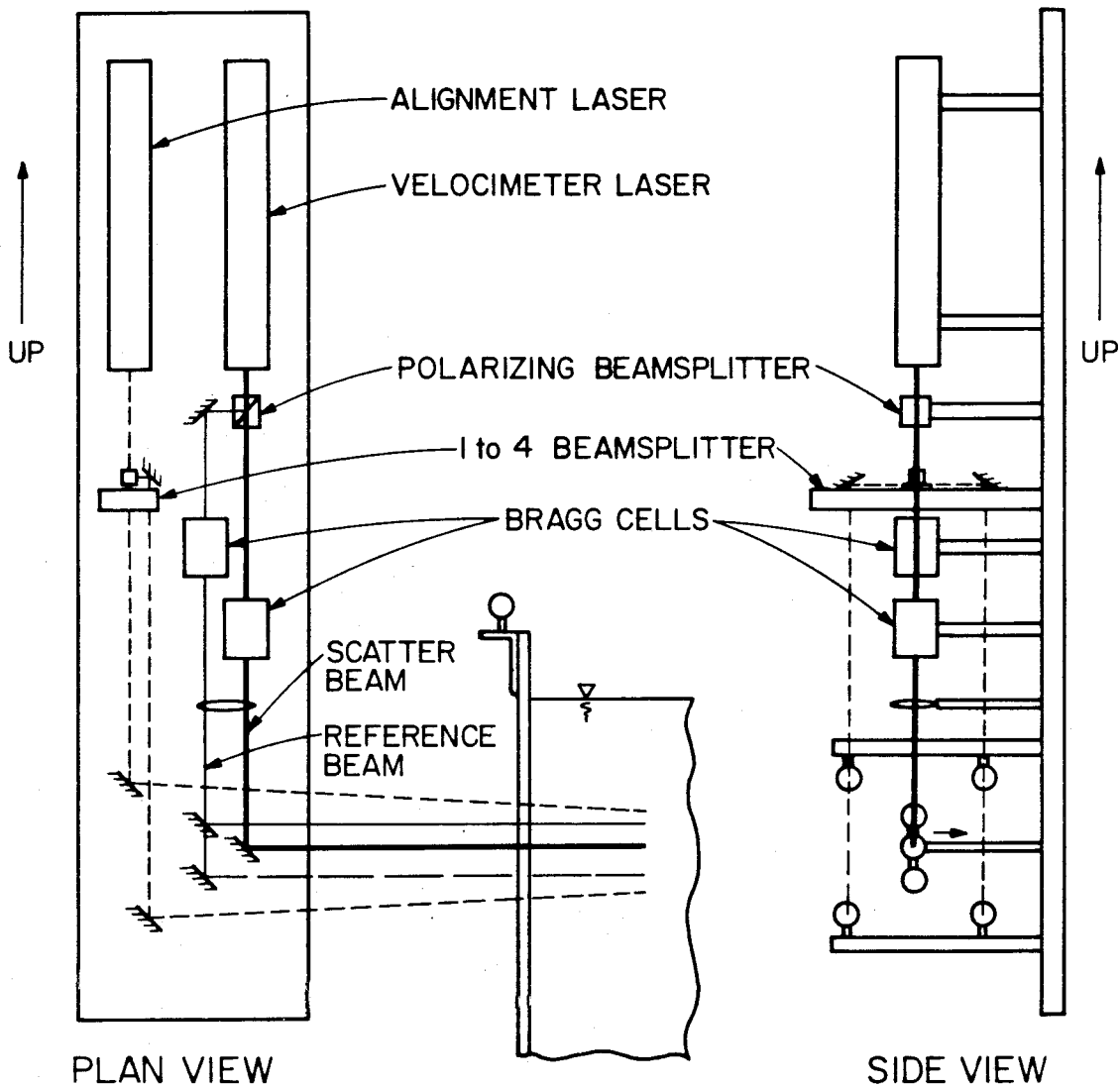


Fig. 4.10 Schematic drawing of the LDV's transmitting optics.

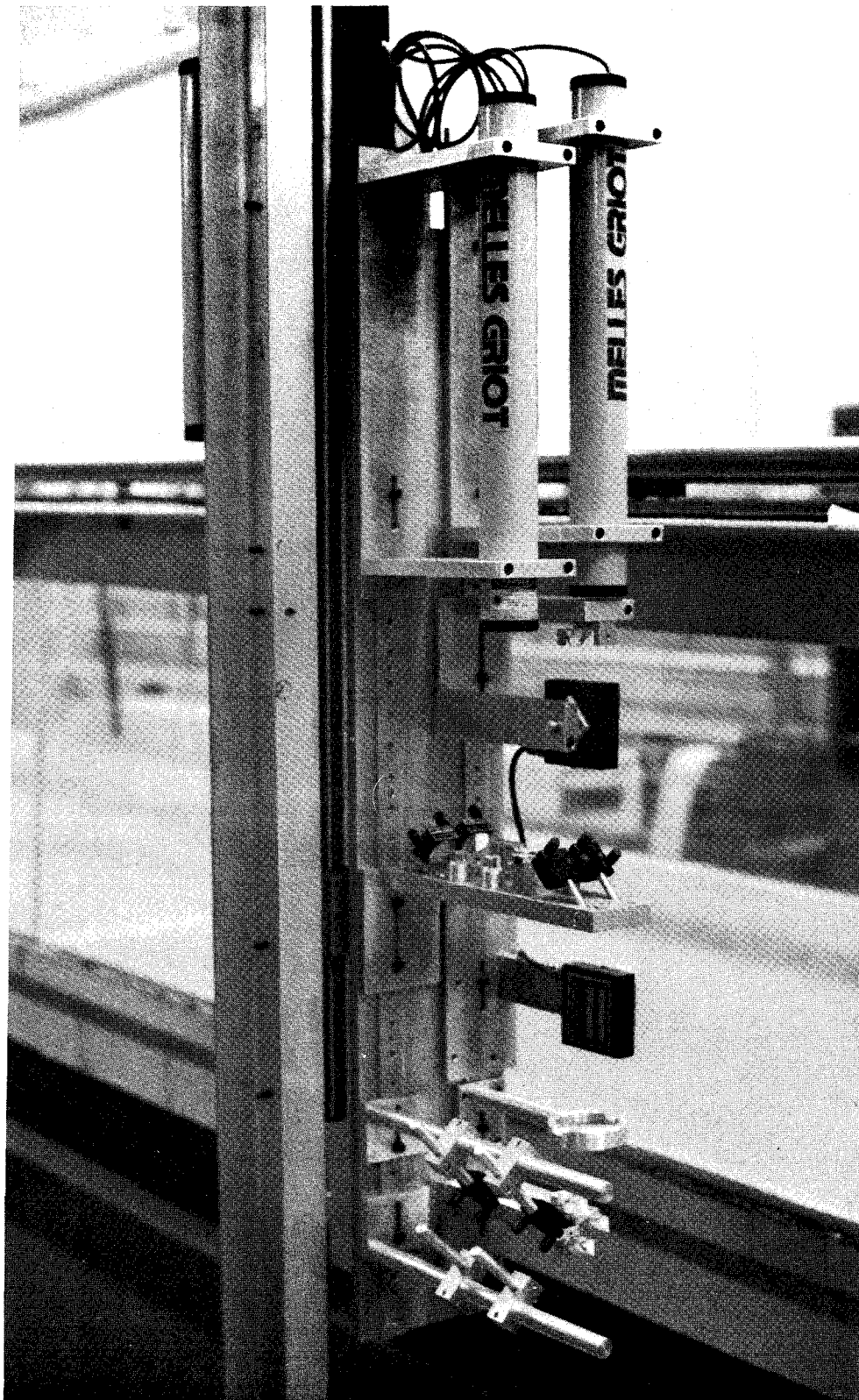


Fig. 4.11 Photograph of the LDV's transmitting optics.

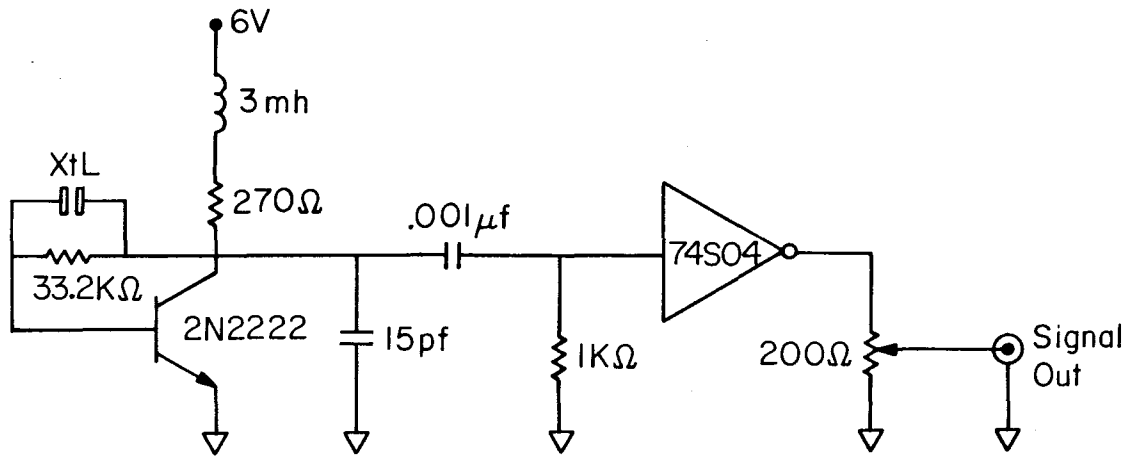


Fig. 4.12 Circuit diagram of source for the Bragg cell drivers.

above or below the scatter beam by sliding a prism in or out of its path.

The alignment beams, shown with short dashed lines in Fig. 4.10, all intersect the scatter beam at the same point within the tank, providing the means by which the receiving optics could be aligned — the reference beams of a conventional LDV normally serve this purpose. The intersection point of all beams defined the location of the measurement volume and could be positioned breadth-wise across the tank, in this study the measurement volume was always at the center of the tank. During the actual operation of the LDV, the alignment beams were switched off.

4.4.2 *The Receiving Optics*

The receiving optics are shown schematically in Fig. 4.13, and consist of: photo-detectors, apertures, focusing lenses, beam splitters, half-wave plates, and mirrors. Like the receiving optics, all optical components have a precision of $\lambda/8$ or better. A photograph of the receiving optics is shown in Fig. 4.14.

As mentioned earlier, the LDV operated in one of two modes, either upward or downward looking. In plan, the two modes appear the same for the receiving optics, illustrating the common use of the optical components. This was accomplished by bringing the scattered light and the reference beam to a common elevation after the first reflection. Considering now a single component: scattered light, from particles in the measurement volume and in the direction of an alignment beam, was directed to the common beam elevation and then redirected and imaged on an aperture placed before the photo-detector. The reference beam, also directed to the common beam level, was split to form two beams, one for each component. The reference beams were then passed through half-wave plates, the half-wave plates being oriented in such a way that the beams would have the same polarization as the scattered light. After the half-wave plates, a 4% reflection was then achieved from the plain glass beam splitter, which was used to direct the beam to the photo-detector to be combined with the scattered light. The photo-detectors were the same as those used by Lang (1985), except for the photo-diode, EG & G Model DT-25-8237 was used in this study. The photo-detectors exhibited excellent gain and low noise characteristics

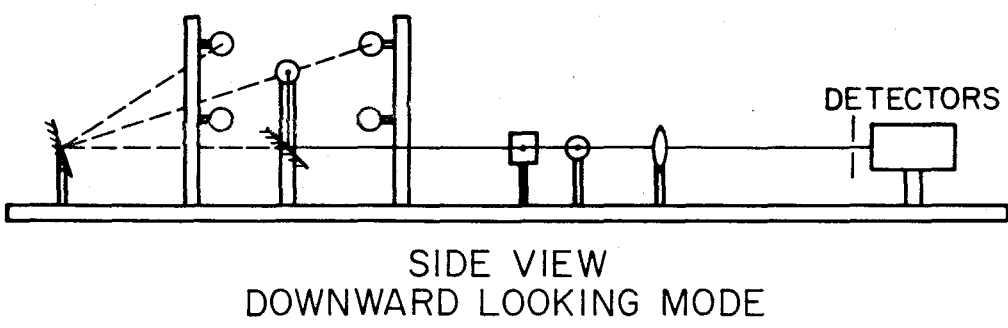
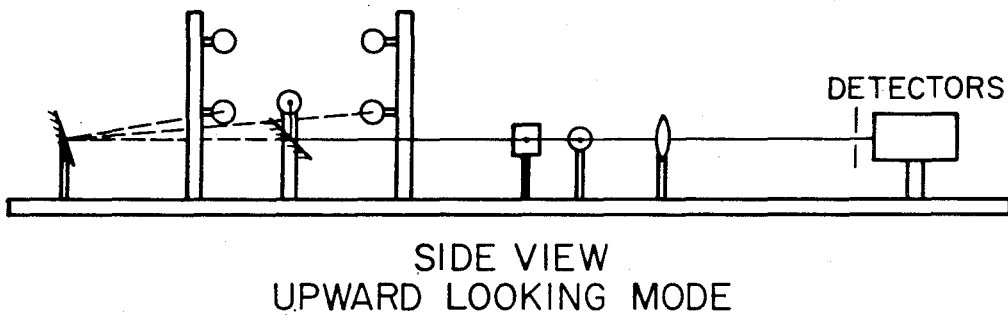
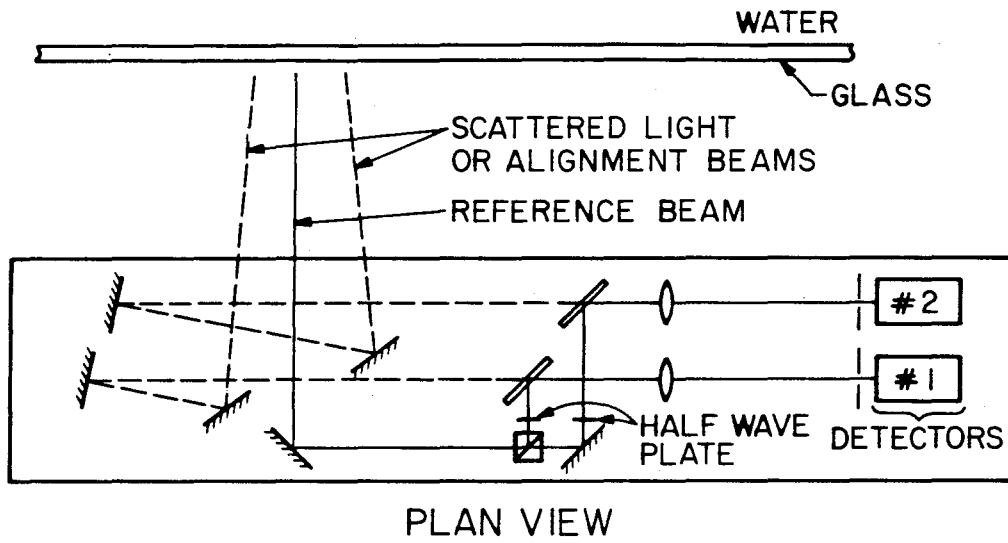


Fig. 4.13 Schematic drawing of the LDV's receiving optics.

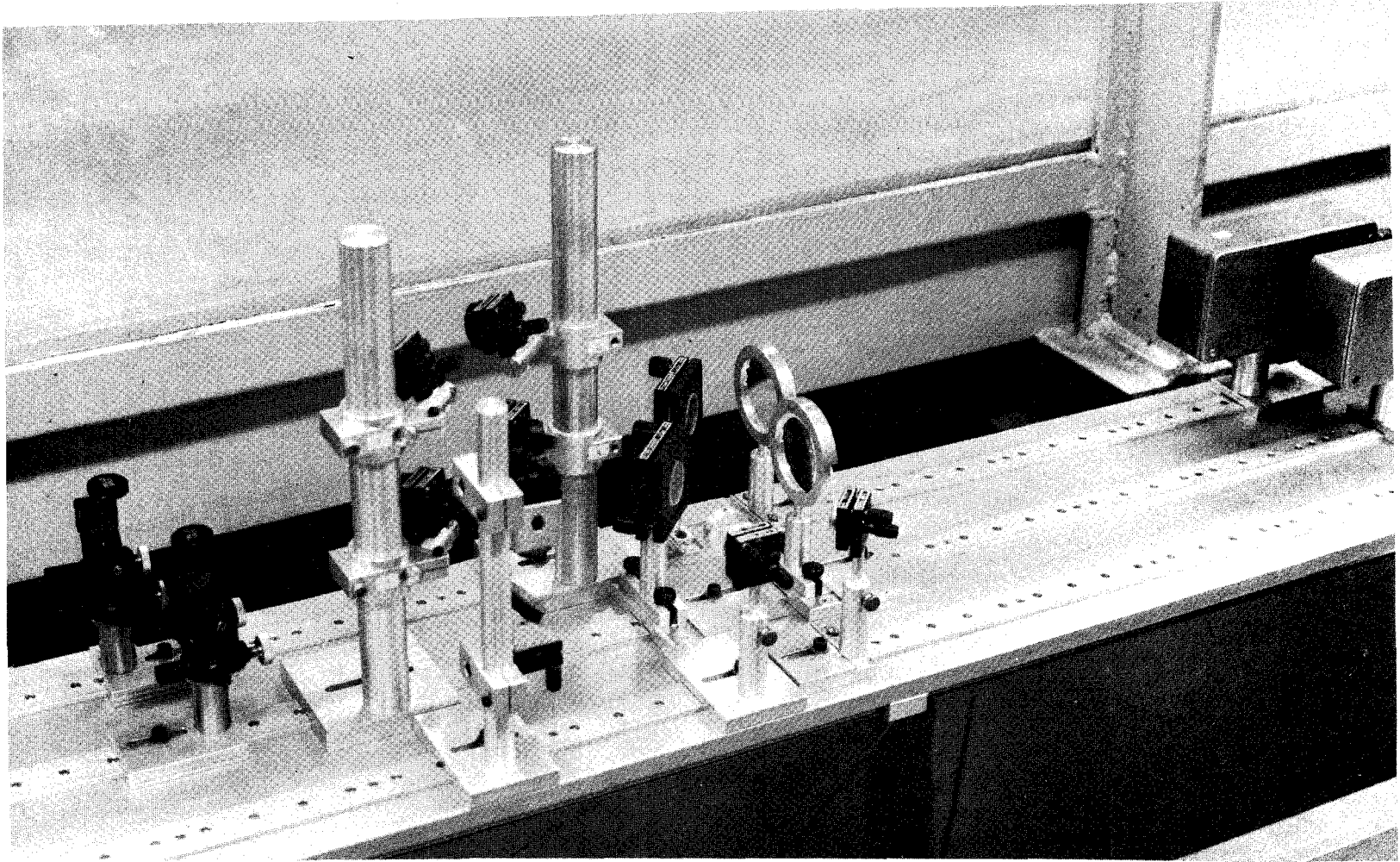


Fig. 4.14 Photograph of the LDV's receiving optics.

and a bandwidth in excess of 1.5 MHz.

4.4.3 *Signal Processing*

The signal from a photo-detector was bandpassed (Kroh-Hite Model 3202R Filter) and then processed by a counter system developed by Gartrell (1978). The counter system amplified the bandpassed signal and determined when a doppler burst was present. When the system detected a doppler burst, the period of a fixed number of cycles was timed with a 20 MHz clock. The system then provided either a digital or an analog output related to the doppler frequency. In this study the analog signal was used which was recorded by the minicomputer.

4.4.4 *LDV Carriage*

A special carriage shown in Fig. 4.15 was designed to support the LDV. It's main structural members were made of 4 in. (10 cm) square aluminum tubing with 4 in. (10 cm) aluminum channels used for bracing. The carriage hung from two parallel tracks made from aluminum I-beams that were mounted to the laboratory's ceiling. The carriage straddled the tank and was moved lengthwise along the tank by hand. A smaller inner carriage, situated within the main frame, rode on three precision rails and was supported by twin screw jacks. An electric motor drove the screw jacks and allowed the LDV to be traversed vertically.

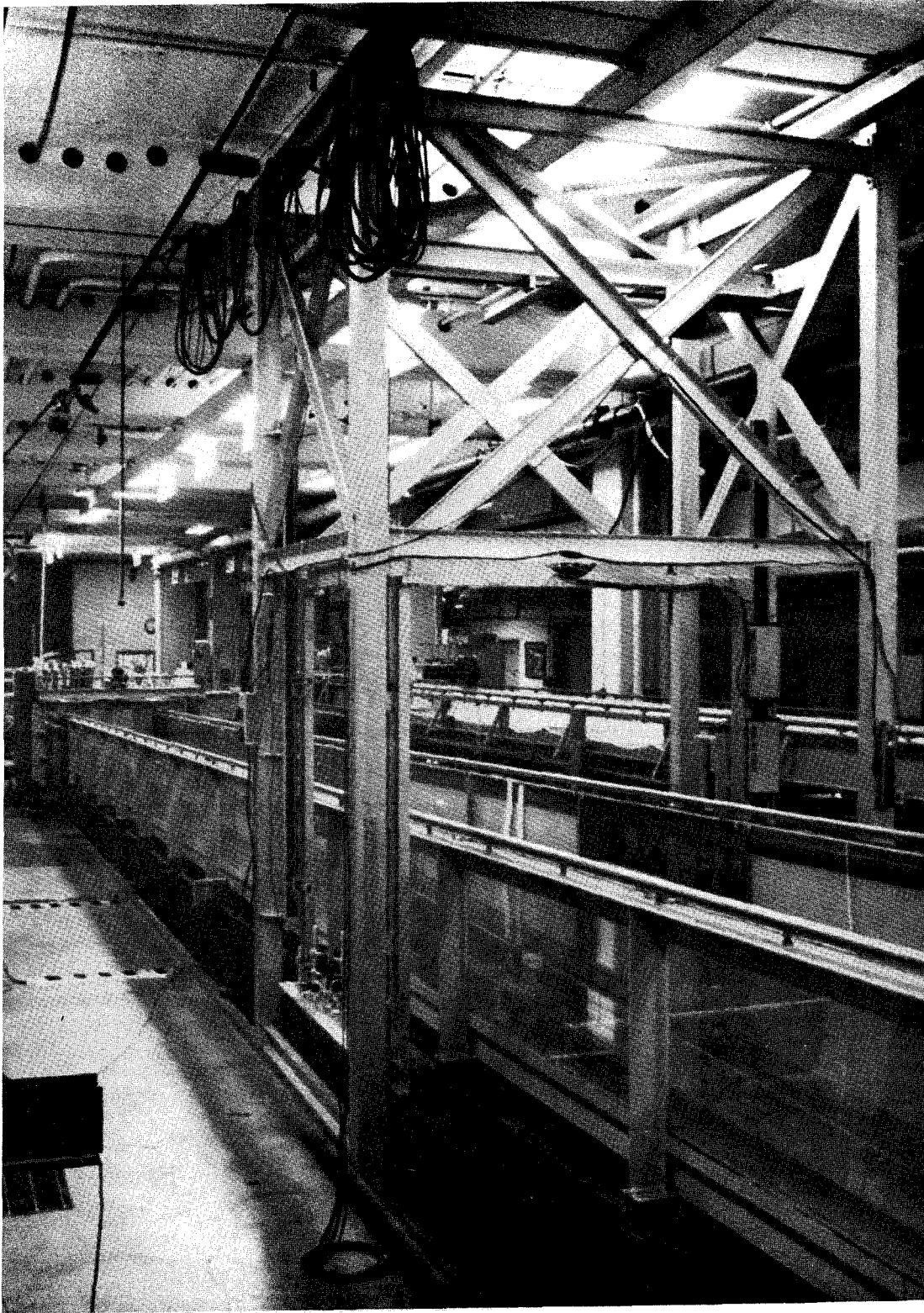


Fig. 4.15 Photograph of the LDV carriage.

The transmitting optics were mounted on one side of the inner carriage, and the receiving optics (seen in the foreground of Fig. 4.15) on the other. The position of the carriage lengthwise along the tank was read from a scale attached to the wave tank and could be read to the nearest 1 cm. The vertical position of the inner carriage was determined from a precision scale attached to it and a vernier scale on the main frame, this arrangement gave the position to within ± 0.1 mm. The carriage assembly allowed for the LDV to be accurately positioned at any point vertically and lengthwise along the tank.

4.5 *Water Surface Measurements*

The position of the water surface was determined in three ways: by resistive wire wave gages, by photographs and by a water mark left on the glass sidewalls of the tank.

4.5.1 *The Resistive Wire Wave Gage*

The wave gage, an example of which is shown in Fig. 4.16, consisted of a support frame 0.125 in. (3.2 mm) diameter, two stainless steel wires 0.01 in. (250 μ m) diameter, spaced 0.16 in. (4.1 mm) apart and tensioned between the support frame's arms. The distance between the arms of the support frames varied between 15 and 35 cm. The wave gage was positioned in the wave tank with a point gage having a resolution of ± 0.1 mm. The gage operated by the simple principle that the resistance between the two stainless steel wires varied with the depth of immersion in water. The wave gage was part of a Wheatstone

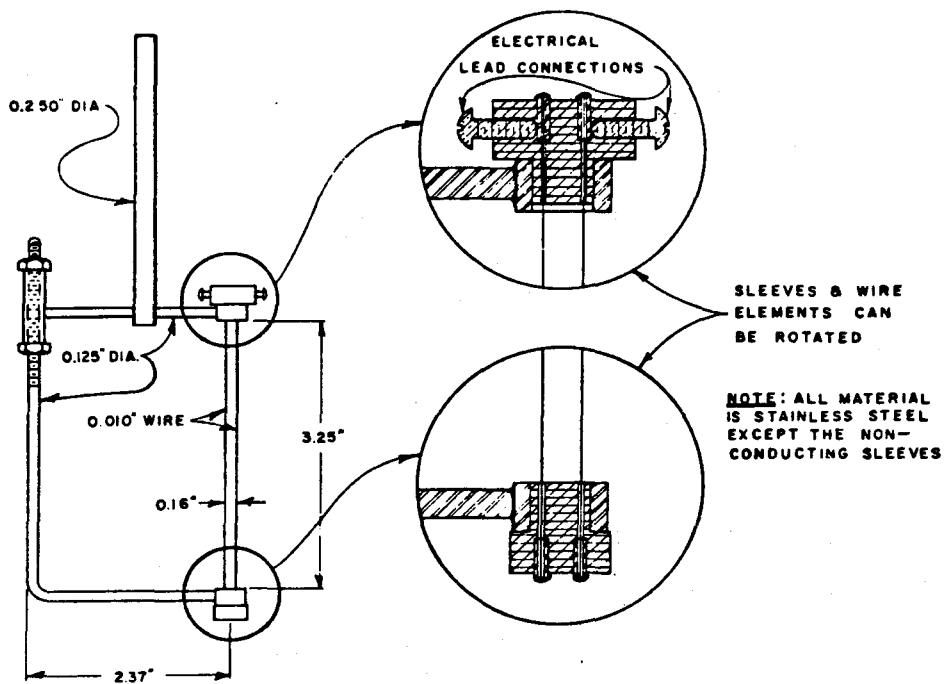


Fig. 4.16 Drawing of typical wave gage (after Raichlen, 1965).

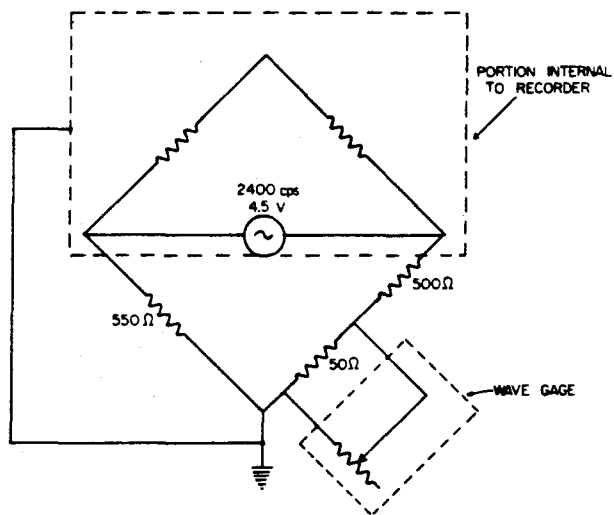


Fig. 4.17 Circuit diagram for wave gage (after Raichlen, 1965).

bridge in a carrier preamplifier (Hewlett Packard 8805A), as shown in Fig. 4.17, that was housed in a stripchart recorder (Hewlett Packard 7700). An analog signal provided by the preamplifier was recorded by the minicomputer.

The wave gages were calibrated manually by varying the immersion of the gages over the range of expected water surface variation. Fig. 4.18 shows a typical calibration curve using a 3rd degree polynomial least-squares fit; the fitted curve was used to compute the water surface elevation. As seen from Fig. 4.18, the resolution of the data acquisition equipment is approximately 1 part in a 1000 over the range of variation, or approximately 0.1 mm, which equals the resolution of the point gage.

4.5.2 *Photographs*

A motor-driven camera (Nikon F-2) was used to photograph waves at various stages of breaking. In all cases the camera was operated with a shutter speed of 1/1000 s, a 135 mm lens, an aperture setting of f5.6, Kodak TRI-X film, and backlighting through a translucent screen. The camera was controlled by the minicomputer using a Nikon relay box (see Fig. 4.2). The timing of the photographs was synchronized with the minicomputer in the following way: the camera, setup as it would be used to photograph waves, was positioned to photograph the display of a counter (Hewlett Packard 5300B); with the display zeroed, a 1 KHz train of pulses was supplied to the counter by the minicomputer; after

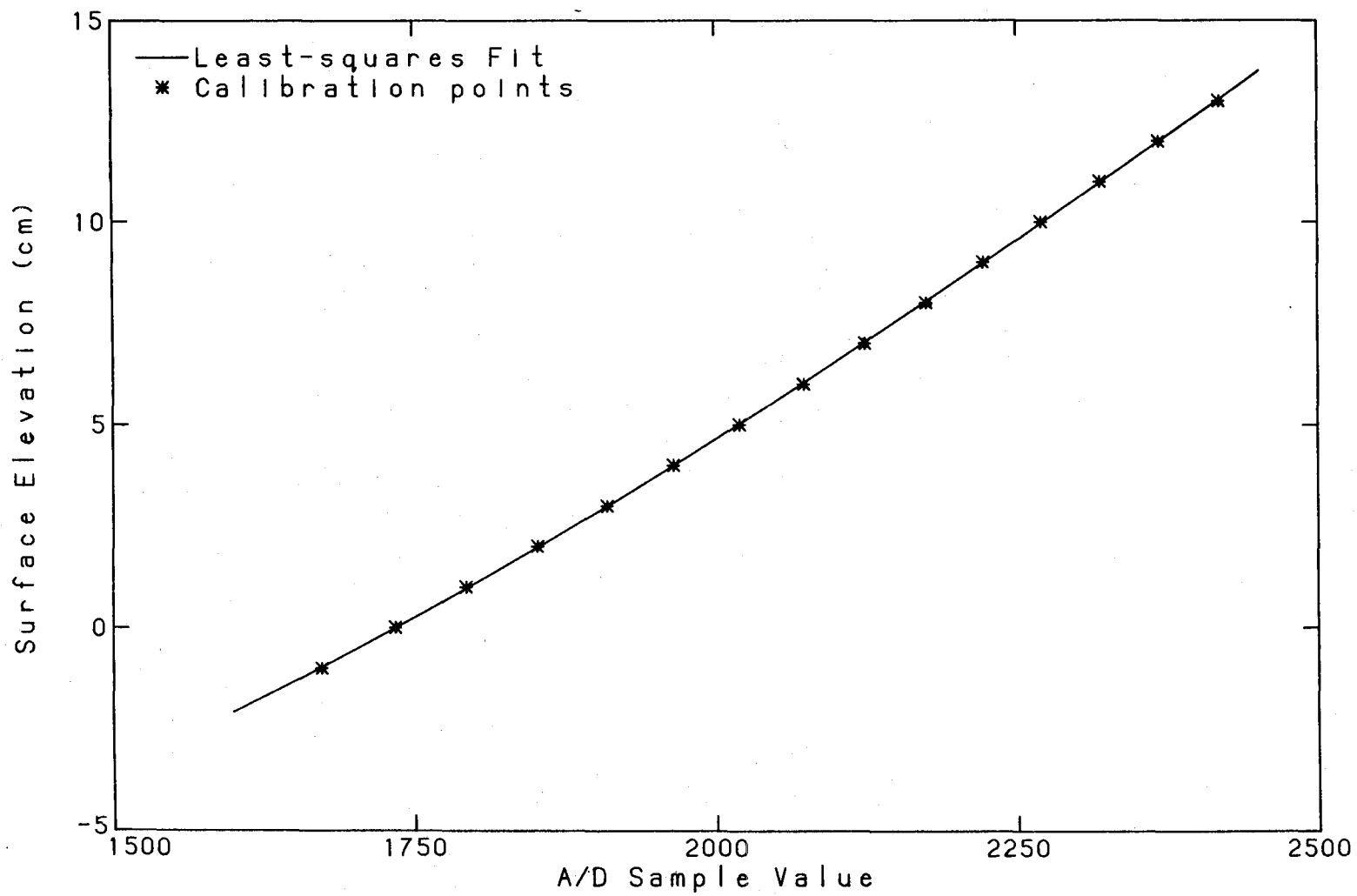


Fig. 4.18 Typical wave gage calibration.

a known number of pulses were issued, the computer instructed the camera to photograph the counter. Comparing the number of counts from the display of the counter, photographed and recorded on film, to the known number of counts issued when the camera was instructed to photograph the display, one could compute the delay time of the camera to within ± 0.001 s. Depending on the operation mode (mirror locked or unlocked) of the camera and the camera used, the delay time ranged between 0.01 and 0.02 s, but was a fixed and consistent delay for a given camera configuration.

4.5.3 *Water Mark*

It was noticed at some length into this study that a distinct water mark (possibly calcium carbonate) developed on the glass walls of the wave tank after a large number of experiments using waves generated under identical conditions, outlining the envelope of the wave's maximum amplitude. The position of the water mark together with the free surface and the tank bottom were measured by a point gage with a resolution of 0.1 mm. The water mark measurements are compared with the wave gage measurements in Fig. 4.19 (see Fig. 2.1 for definition of symbols). Near $h/h_0=0.8$ the comparison is very good, at $h/h_0=0.6$ and shoreward to $h/h_0=0.42$ the water mark compares well but consistently predicts an amplitude slightly larger than the wave gage measurements. Shoreward of $h/h_0=0.4$, the wave used for this comparison is growing rapidly in amplitude and is becoming steeper; the measurements from this region begin to differ considerably. The wave gage

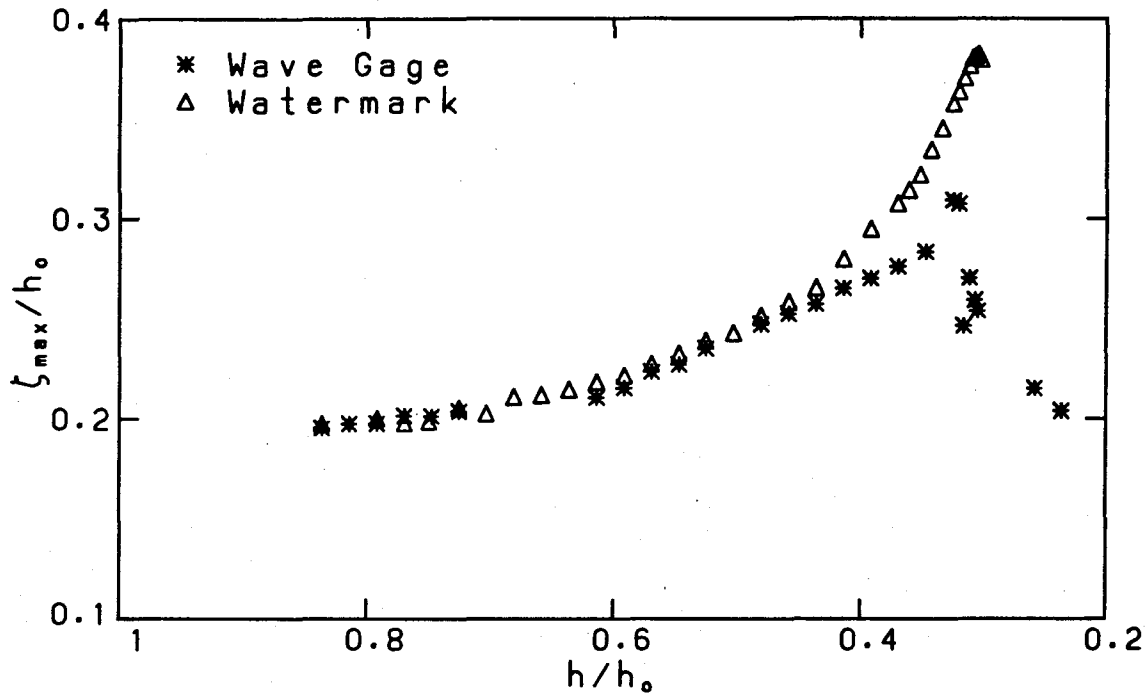


Fig. 4.19 Water mark and wave gage measurement.

under-predicted the wave's amplitude in this region due to the high frequency content of the signal resulting from the near vertical portions of the free surface. The maximum amplitude at breaking ($h/h_0=0.3$) was determined from a photograph and it compares to within $0.012h_0$ (5 mm) of the maximum water mark measurement shown in Fig. 4.19. Thus it is believed that the water mark gave accurately the envelope of the maximum amplitude. This type of measurement was available only for the plunging wave case up to the point of breaking; after breaking the water mark was no longer distinct.

4.6 *Other Experimental Procedures*

In this section we outline procedures used, that may have important effects on the results from experiments of this type.

To ensure that the waves used were reproducible and that the breaking zone was free of contamination from a previous breaking wave, 1/2 hour was allowed between runs. After this period of time neither detectable variations in the water surface elevation by a wave gage nor fluid motion by the LDV were seen.

The 1/2 hour wait between experiments caused other problems due to the long length of time needed to run a series of experiments. These problems included variations in the water surface due to evaporation and minor leaks in the tank and variations in the surface tension of the water due to surface contamination.

A small change (~ 0.5 mm) in the water surface level can cause a noticeable change in the time required a wave to travel from the point of generation to the point of breaking. To avoid variations in the water surface level, a 4 in. (10 cm) diameter overflow was positioned at the desired level of the water surface and a constant inflow of water was supplied to the reservoir at the backside (so no disturbances were created in the test section) of the wave paddle. This arrangement maintained the water surface level to within ± 0.1 mm for an indefinite length of time.

Miller (1970) has shown that surface tension does affect the breaking process in laboratory scale experiments. He pointed out that even in the cleanest of laboratories the surface tension will change with time. Having this in mind, all experiments were consistently run after clean tap water sat for two days in the tank and usually lasted for not more than an additional two days. The surface tension was not measured and it is not known if it varied over the course of an experiment.

CHAPTER 5

PRESENTATION AND DISCUSSION OF RESULTS

The results of this study are based on water particle velocity and surface elevation measurements made for two cases: a spilling breaker and a plunging breaker. Maximum surface elevation measurements for a second spilling breaker will also be presented. In all cases, solitary waves were used. The parameters (defined in Fig. 2.1) which describe each case are given in Table 5.1.

Table 5.1 Wave parameters and type of measurements made.

Case	Type of Breaker	h_0 (cm)	$\frac{H_0}{h_0}$	S	Type of Measurements	
					Velocity	Surface Elev.
1	Spilling	25.00	0.2	0.0075	.	.
2	Spilling	27.65	0.4	0.0062	.	.
3	Plunging	43.25	0.2	0.0192	.	.

The configuration of the wave tank and the wave generator was such that the waves were generated on the sloping bottom and thus never travelled on the horizontal section shown in the definition sketch, Fig. 2.1. The offshore depth, h_0 , was taken to be the depth at the mean position of the paddle trajectory. The parameters, listed in Table 5.1, were chosen to obtain representative spilling and plunging breaking waves. Information, presented by Street & Camfield (1966) of breaker type as a function of beach slope and initial amplitude ratio, was very useful in

choosing the parameters.

The coordinate used to represent the position along the sloping bottom is h/h_0 , allowing the reader to quickly envision the location in question (e.g., $h/h_0=0.5$ is exactly midway between the toe of the beach and the shoreline). Further, this coordinate is usually plotted running from right to left, giving the presentation of the data an orientation which is the same as the definition sketch. In the same spirit, the time coordinate is plotted running from right to left. This gives the presentation of time series an appearance similar to the equivalent information given in the spatial coordinate, x , had it been measured.

The resulting initial profiles of the waves generated for the three cases listed in Table 5.1, together with Boussinesq's (1872) prediction for a solitary wave on a horizontal bottom, are shown in Fig. 5.1. Each wave profile was measured shoreward of the generation point due to the inability to measure the surface elevation directly at the wave paddle. Fig. 5.1a shows the profile for the case with $h_0=25.0$ cm, $H_0/h_0=0.2$, and $S=0.0075$ that was measured at $h/h_0=0.95$. The profile from the experiment is in good agreement with theory but is somewhat broader at the base. As was the situation for the waves from each case, small oscillatory waves were present and can be seen trailing behind the wave. Fig. 5.1b shows the wave profile for the case with $h_0=27.65$ cm, $H_0/h_0=0.4$, and $S=0.0062$ that was measured at $h/h_0=0.97$. Apart from the oscillatory waves, this wave is in best

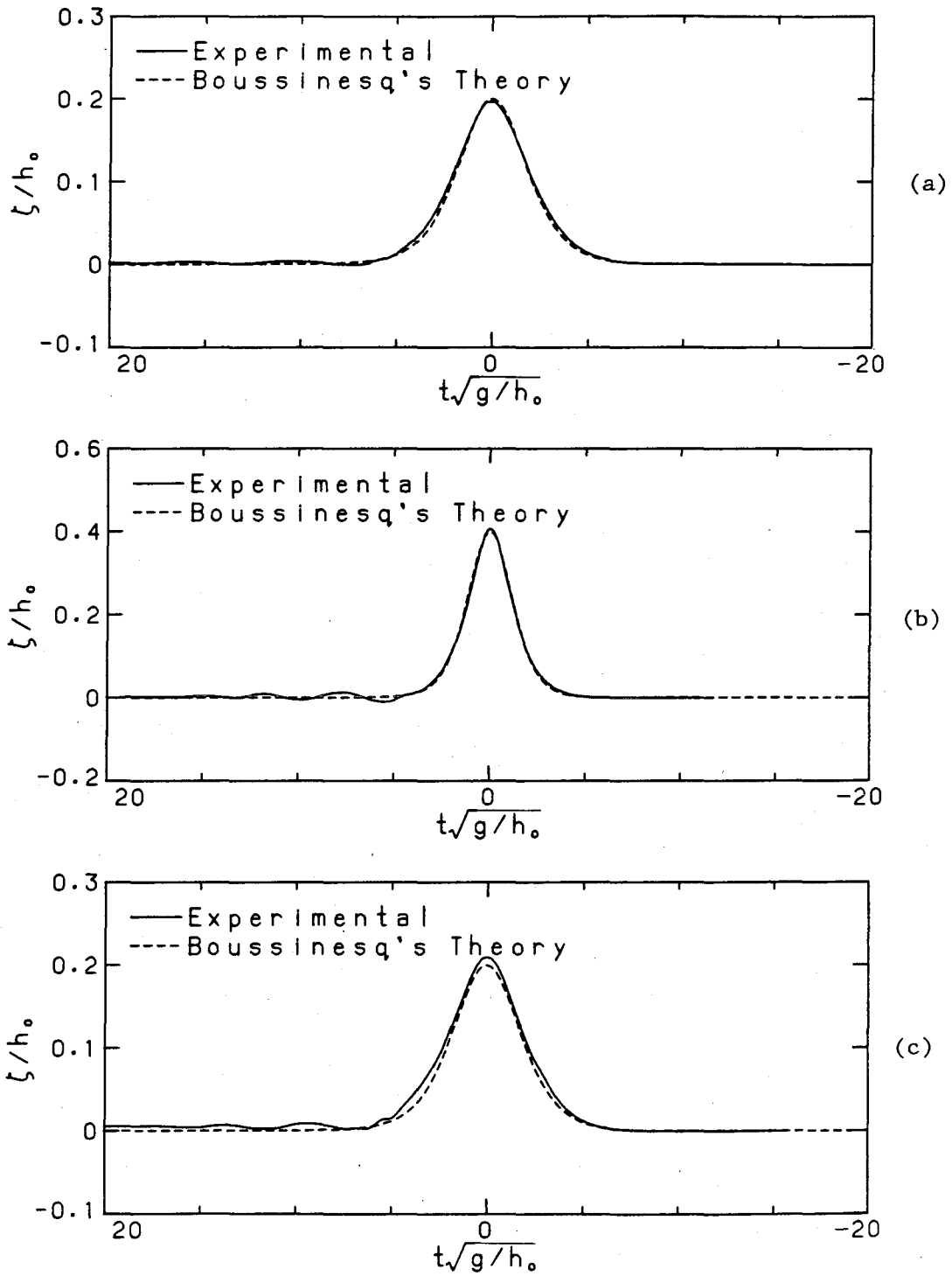
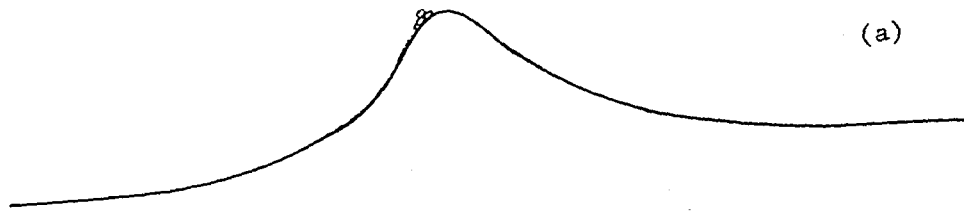


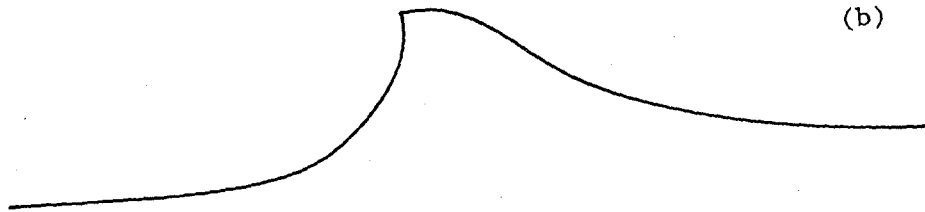
Fig. 5.1 Initial wave profiles; (a) $h_0=25.0$ cm, $H_0/h_0=0.2$, $S=0.0075$; (b) $h_0=27.65$ cm, $H_0/h_0=0.4$, $S=0.0062$; (c) $h_0=43.25$, $H_0/h_0=0.2$, $S=0.0192$.

agreement with theory when compared to the other two cases studied. This may be because it was measured the closest (in a relative sense) to the wave generator and that the slope was the smallest for all three cases. Fig. 5.1c shows the wave profile for $h_0=43.25$ cm, $H_0/h_0=0.2$, and $S=0.0192$ that was measured at $h/h_0=0.89$. The amplitude of the wave for this case is larger than that predicted by theory. The increase in amplitude cannot be entirely accounted for by shoaling; it may be due to the increase in the undisturbed water level seen after the wave passes. This increase in water level may be attributed to the generation technique used, or it may possibly be a reflected wave which is discussed further in Section 5.2.2.

It should also be clarified what will be the operational definition of the breakpoint for the two breaker types studied. While the qualitative features for each type of breaker, described in Chapter 1, are clear, more specific criteria for the location of breaking is necessary for quantitative comparison. For the spilling wave, it is taken to be the first appearance of a broken surface at the crest, and, for the plunging wave, it is taken to be the point at which the surface segment just in front of the crest becomes vertical. The location of each breakpoint was determined from visual observations made of the waves. Sketches of both breaker types are shown in Fig. 5.2 with each type of breaker at what was considered the point of breaking under the above definitions. The measured breaking parameters, for each case are listed in Table 5.2 (see Figures 2.1 and 2.2 for definition of symbols).



Spilling Breaker



Plunging Breaker

Fig. 5.2 Sketches of waves at breaking; (a) spilling breaker, (b) plunging breaker.

Table 5.2 Breaking parameters for this study.

Case	Type of Breaker	h_b (cm)	$\frac{H_b}{h_b}$	$\frac{h_b}{h_o}$
1	Spilling	10.54	0.91	0.42
2	Spilling	17.33	0.84	0.63
3	Plunging	13.40	1.24	0.30

There were in excess of 700 experiments conducted for this study; the locations of each velocity and surface elevation measurement are listed in Appendix B.

5.1 *The Reproducibility of the Generated Wave*

To obtain many of the results to be presented in this chapter, it was essential to have a means of generating a reproducible wave. A reproducible wave was necessary because of the desire to obtain information about the spatial variation of the flow in a breaking wave, at a single instant in time, by use of sequential single point measurements. In a sense, a *snapshot* of the flow is desired. The care taken to generate the waves has been outlined in Chapter 4. Here, the degree to which the waves were reproducible will be demonstrated with some velocity measurements obtained by the LDV and with photographs taken just after breaking.

Fig. 5.3 shows horizontal and vertical velocity time series at five elevations for the plunging wave case at breaking. There are actually two traces atop one another for each elevation and velocity component. Hence, this figure has been produced from ten individual experiments. In all cases, the traces are very near to being identical when inspected visually; the amplitude variations, from one run to another at any single elevation, average approximately $0.01\sqrt{gh}$.

Fig. 5.4 contains four photographs of the plunging breaker, each of which was taken at the same time after generation of separate waves generated under the same conditions. The vertical spacing of the grid lines is $0.12h_0$ (5 cm) and the vertical line just ahead of the wave is at $h/h_0=0.28$. The time at which the photographs were taken have an uncertainty of ± 0.001 sec, which translates to a spatial uncertainty in the direction of propagation of $\pm 0.005h_0$. Most variations seen in the photographs fall within that spatial uncertainty.

Reproducibility, as described above, could be obtained anywhere seaward of the point of breaking; shoreward of the point of breaking, one does not see the same sort of reproducibility. We illustrate this in Fig. 5.5, which shows the velocity time series for ten individual runs made under the same carefully controlled conditions as those of Fig 5.3. Again, records from the plunging wave case have been used and were measured at $h/h_0=0.17$ and $z/h=-0.67$. The variability of the flow after breaking is discussed further in Section 5.5.

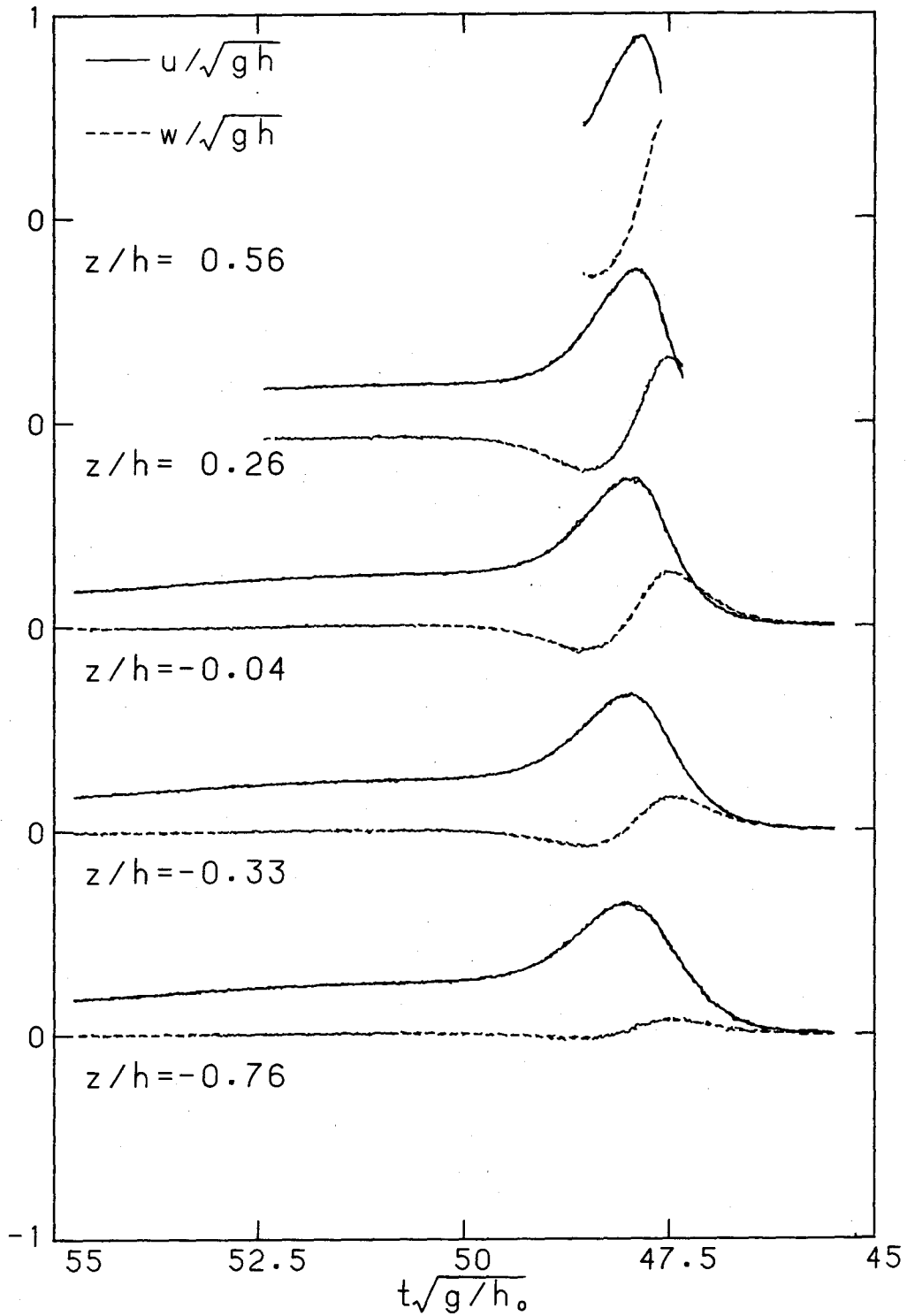


Fig. 5.3 Demonstration of the reproducibility of the wave; horizontal and vertical velocity at locations vertically through the depth for the plunging wave at $h/h_0=0.30$.

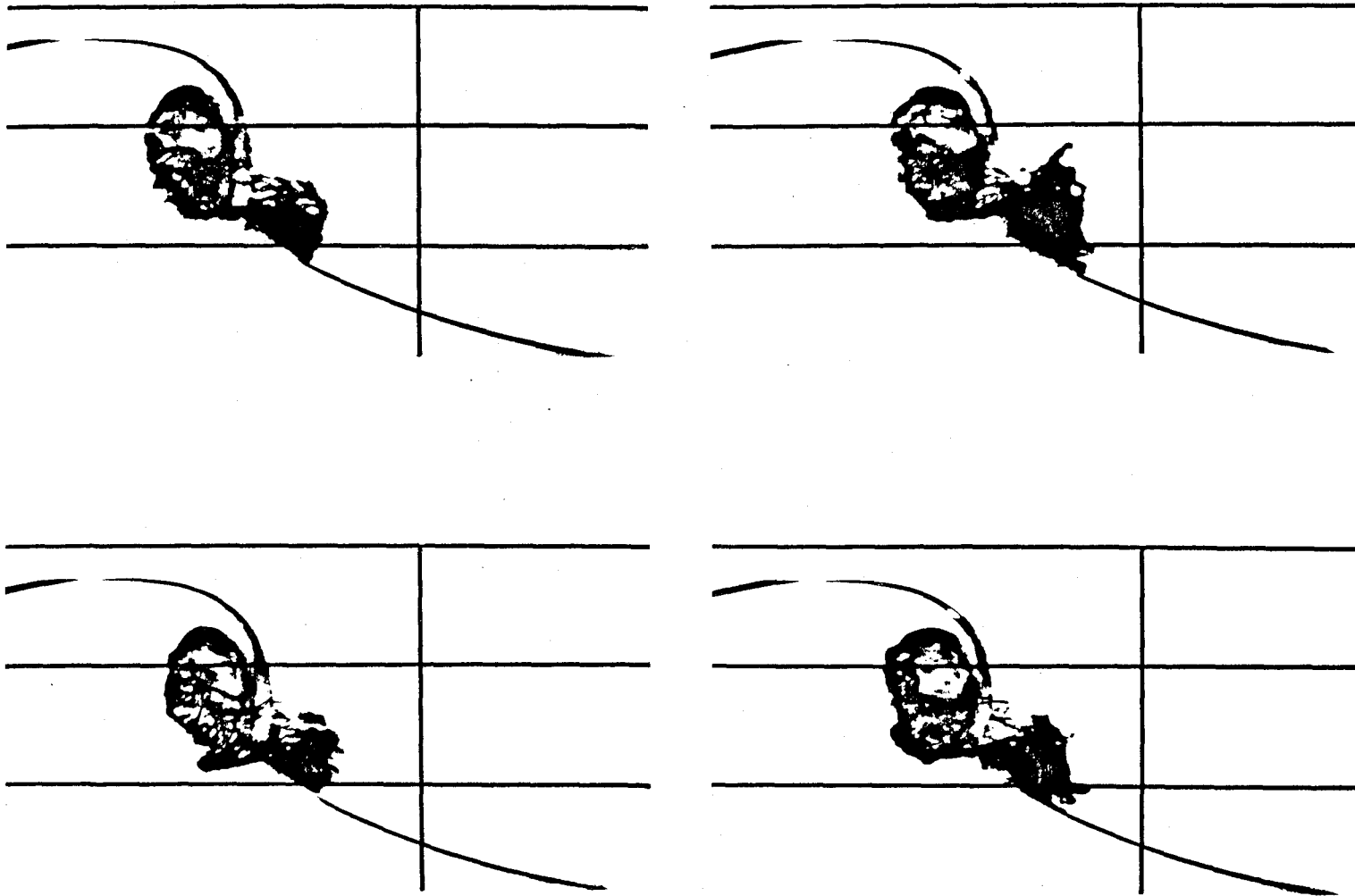


Fig. 5.4 Demonstration of the reproducibility of the wave; photographs of the plunger breaker.

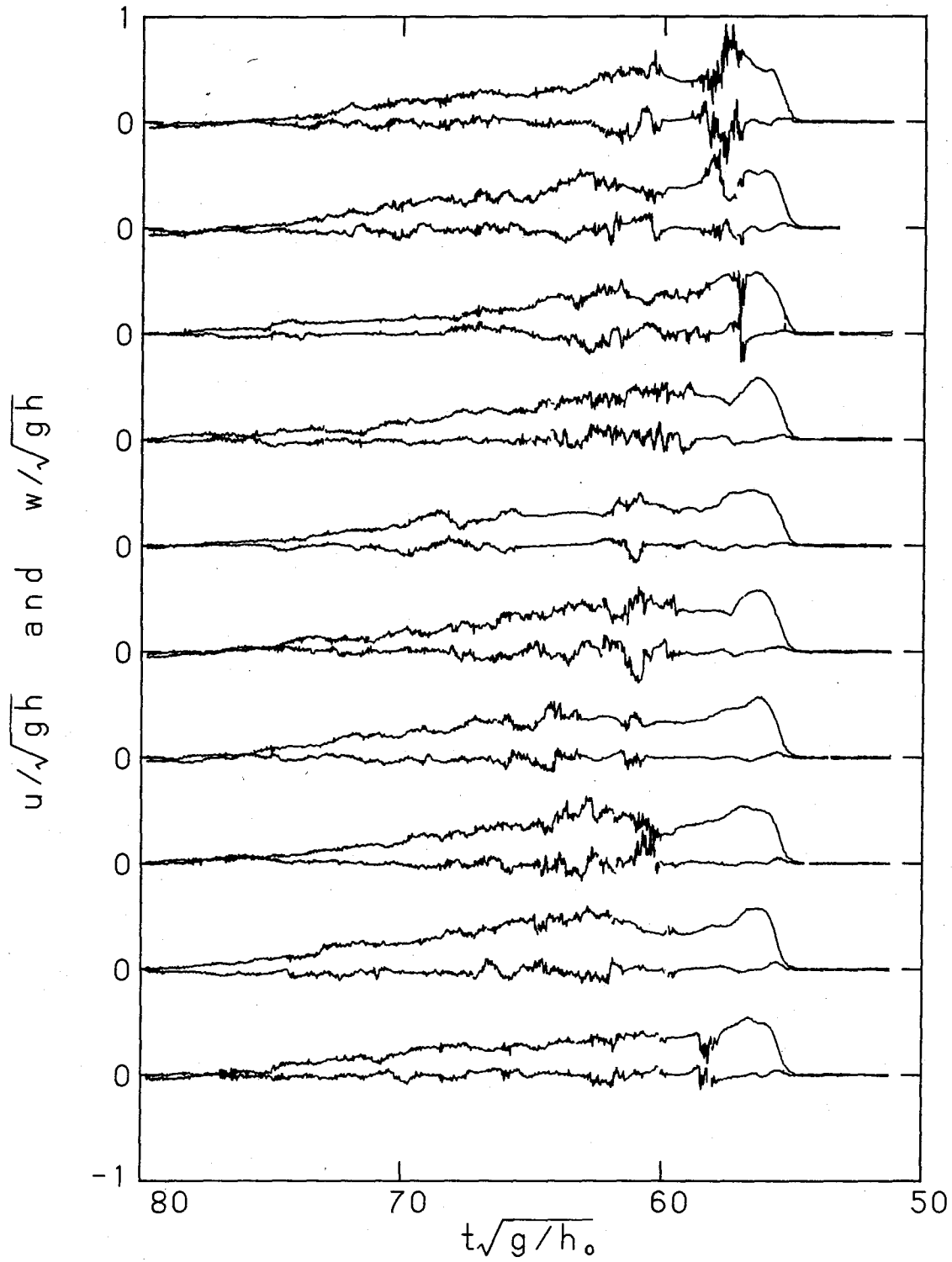


Fig. 5.5 Ten velocity time series used to show variability after breaking, plunging wave case at $h/h_0=0.17$ and $z/h=-0.67$.

5.2 The General Nature of the Solitary Wave on a Beach

In this section, the evolution of the solitary wave as it propagates up a sloping bottom will be presented by using measurements of its profile. A comparison of the data obtained from this study will be made with that of Camfield & Street (1969) and Saeki *et al.* (1971), the only known investigations of solitary waves on sloping bottoms within the range of slopes used in this study.

5.2.1 Spilling Breaker

Fig. 5.6 shows wave profiles measured at four locations along the beach, and indicate the evolution of a solitary wave, that breaks as a spiller, on a sloping bottom. This wave corresponds to case 2 in Tables 5.1 and 5.2. Near generation, at $h/h_0=0.9$, the wave has some small oscillatory waves trailing behind it, but appears to be not far removed from the shape of a solitary wave on a horizontal bottom. As the wave propagates up the beach, its amplitude increases and it becomes steeper. The small tail, discussed in Chapter 2, begins to emerge at the rear of the wave and is first noticed at $h/h_0=0.76$. At $h/h_0=0.63$ the wave is very steep and was observed to be at its breakpoint with a maximum height to depth ratio of $H_b/h_b=0.84$. Shoreward of the breakpoint, the wave decays rapidly as it propagates on to $h/h_0=0.49$. The wave profile after breaking, at $h/h_0=0.49$, shows that, for this spilling case, the wave has yet to reach a shape similar to the profiles in Fig. 2.3b that show a plunging breaker after breaking. In fact, it appears that this spilling wave retains the

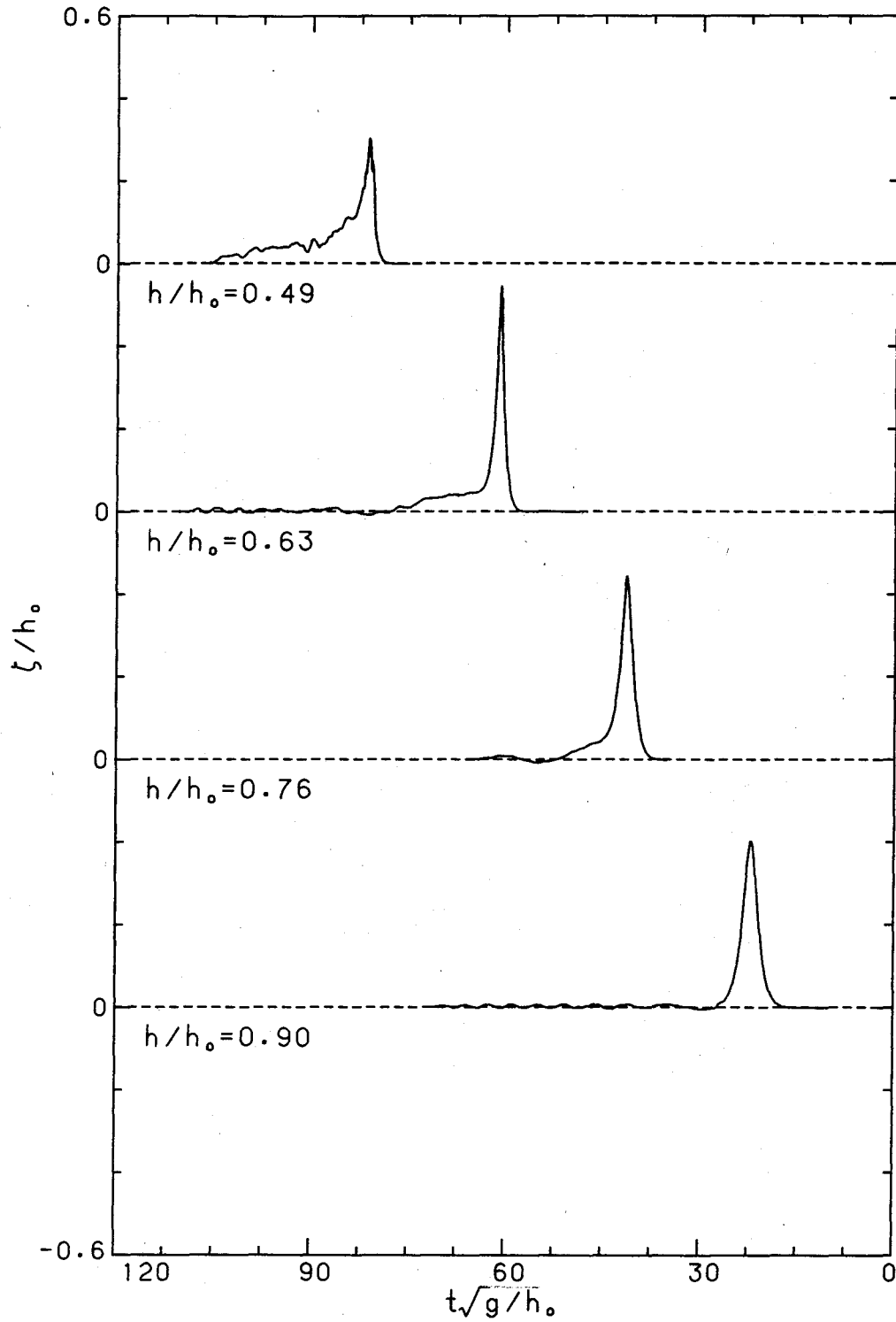


Fig. 5.6 Evolution of a solitary wave on a sloping bottom which breaks as spiller, case 2.

general shape it had before breaking. This contrasts with the plunging breaker shown in Fig. 2.3a which quickly attained the triangular wave shape.

In Fig. 5.7, the measurements of ζ_{\max}/h_b obtained from case 2 are compared to those of Saeki *et al.* (1971) who did their experiments on a slope of 0.0067 with a range of initial amplitude ratios. In this figure, the maximum amplitude, ζ_{\max} , and the local depth, h , have been normalized by the depth at breaking, h_b , following the practice of Saeki *et al.* Although it appears from the figure that data from all initial amplitude ratios collapse to consistent trends, the evidence is not conclusive that h_b is the appropriate normalization. From the figure, the measurements from this study are seen to be consistent with Saeki *et al.*'s data except, perhaps, for the initial region near generation. This departure may be due to the method used in this study of generating the waves on a sloping bottom. Clearly seen in this figure are the four zones of the shoaling-through-breaking solitary wave as discussed in Chapter 2. The power laws of $-1/4$ and -1 before breaking have been drawn and show good agreement. If one looks closely, however, there is sufficient scatter that one could draw a range of power laws within each segment. For instance, Leibovich & Randall (1973) could fit their $-1/3$ power law to the data in the ZGS (zone of gradual shoaling), here, and in subsequent data to be presented. The -1 power law shows up clearly prior to breaking in what we have termed the ZRS (zone of rapid shoaling). In the ZRD (zone of rapid decay), just after breaking, ζ_{\max}/h_b appears to follow a power

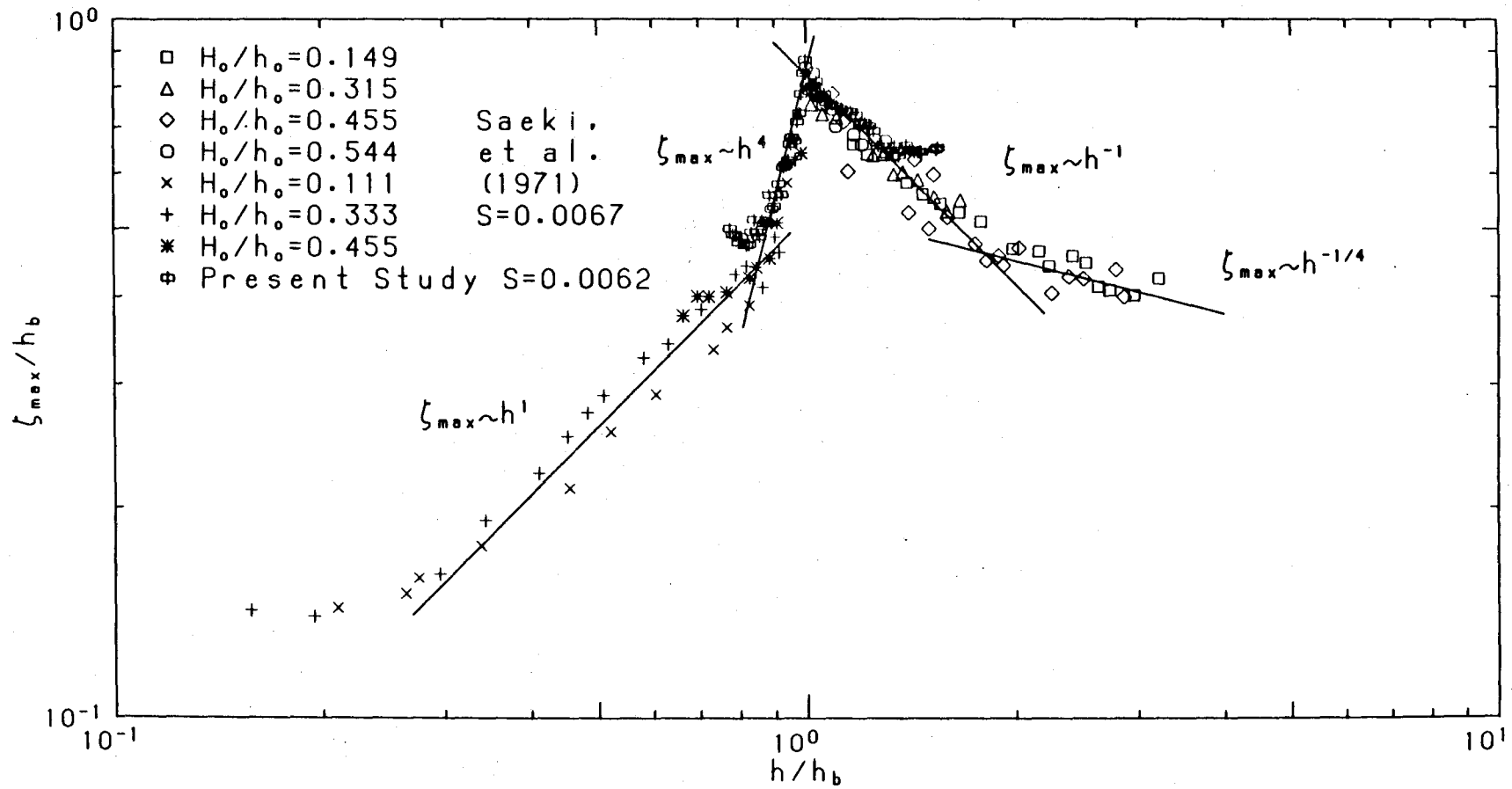


Fig. 5.7 Maximum amplitude variation for a spilling wave, case 2, compared with Saeki et al. (1971).

law close to 4. In the ZGD (zone of gradual decay), ζ_{\max}/h_b is proportional to the depth, and thus, in a relative sense, the maximum amplitude ratio is constant.

The celerity of the wave as it propagates up the slope, for case 2, is shown in Fig. 5.8. In Fig. 5.8a the celerity has been normalized by the local shallow water wave speed, \sqrt{gh} , and in Fig. 5.8b by the offshore shallow water wave speed, $\sqrt{gh_0}$. The celerity was computed by simply taking the distance between two neighboring wave gages and dividing by the difference in the arrival times of ζ_{\max} at each respective gage. Also shown in the figure is the result obtained if one uses the measured values of ζ_{\max} and the equation which gives the celerity of a solitary wave on a horizontal bottom, $\sqrt{g(h+\zeta_{\max})}$. The two different presentations of the celerity show that, in a relative sense, the celerity is continually increasing, while, in an absolute sense, it is decreasing, in the region before breaking. Also, in the region before breaking, the celerity of the wave is well predicted by the celerity for a wave of the same amplitude on a horizontal bottom. Just before breaking and continuing on through the range of measurements after breaking, the celerity increases and eventually exceeds the celerity at generation. The reason for the oscillations seen in the celerity after breaking are not clear. It may be that the arrival time of ζ_{\max} is somewhat random after breaking (recall that this information comes from many experiments), or it may be that ζ_{\max} is no longer a good indicator of the wave's celerity after breaking.

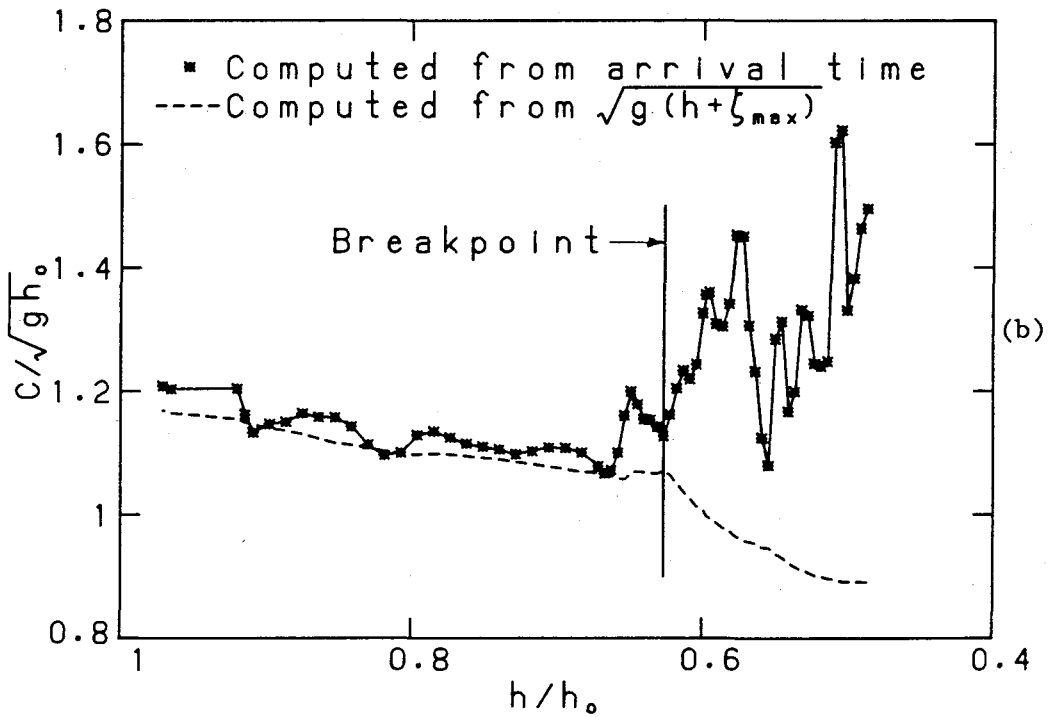
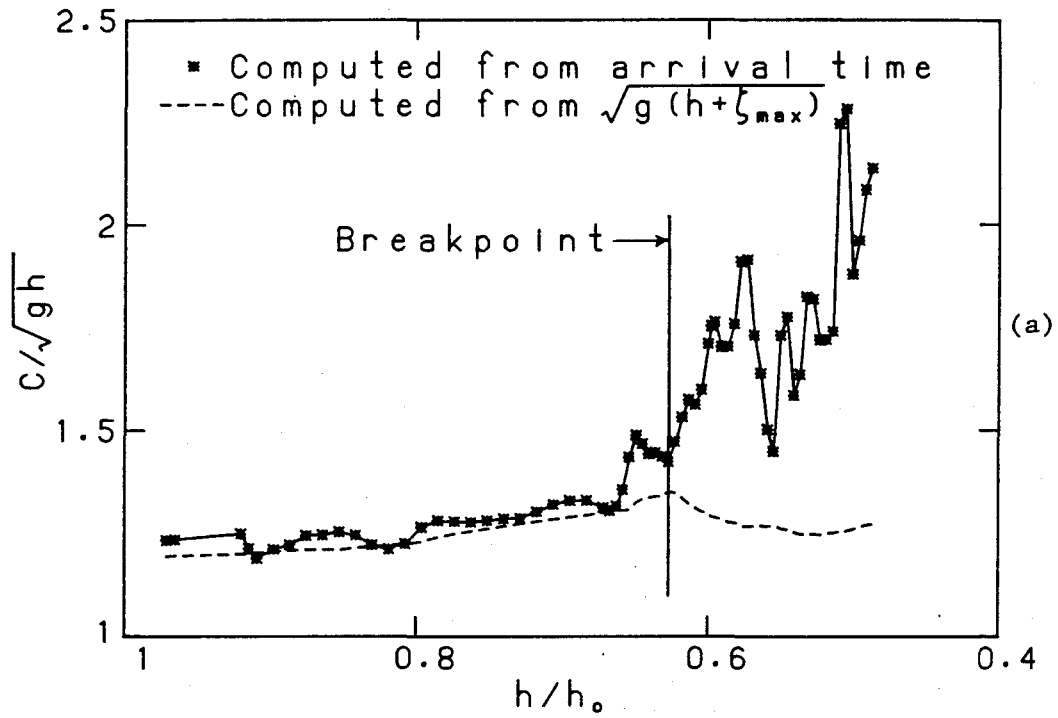


Fig. 5.8 Wave celerity for a spilling wave, case 2; (a) normalized by the local shallow water wave speed, (b) normalized by the offshore shallow water wave speed.

The maximum amplitude was also measured for the wave listed as case 1 in Tables 5.1 and 5.2. The results are shown in Fig. 5.9. We can fit the power laws that have been discussed which occur before breaking, but, here, we wish mainly to illustrate again the two zones after breaking. The amplitude decay in the ZGD is clearly proportional to the depth and the power law of 4 is drawn to show the approximate trend in the ZRD. It is also interesting to look at the amplitude variation for the case when ζ_{\max} is normalized by the local depth and plotted with linear scales as in Fig. 5.10. Again the two zones after breaking are clear and we see that the amplitude ratio at breaking, H_b/h_b , for this slope is approximately 0.9. In the ZGD we see that ζ_{\max} , relative to the depth, is constant at somewhat less than 0.6. We have no other data to compare with these, nevertheless, they are consistent with measurements from other slopes, both from this studies and other's.

5.2.2 *Plunging Breaker*

The evolution of a solitary wave, which breaks as a plunger, up a sloping bottom is shown in Fig. 5.11. This wave corresponds to case 3 in Tables 5.1 and 5.2. At $h/h_0=0.84$, somewhat shoreward of generation, the wave has yet to lose its basic solitary wave appearance and a slight increase in the undisturbed water elevation is seen to the rear of the wave beginning at $t\sqrt{g/h_0} \sim 30$ and onward for the duration of the record. This increase in the surface elevation may be a reflected wave, as discussed by Peregrine (1967) and Knickerbocker & Newell

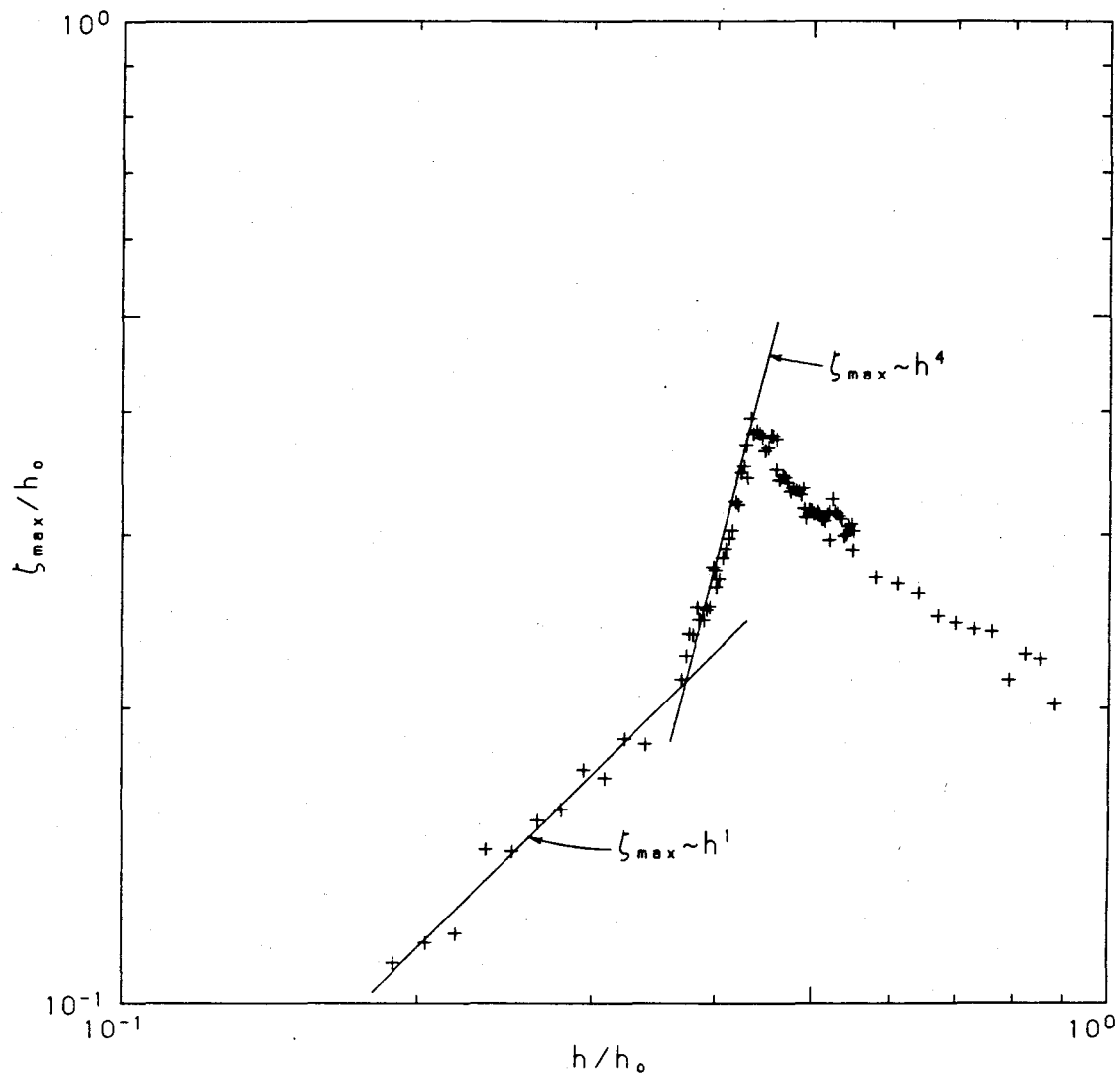


Fig. 5.9 Maximum amplitude variation for a spilling wave, case 1.

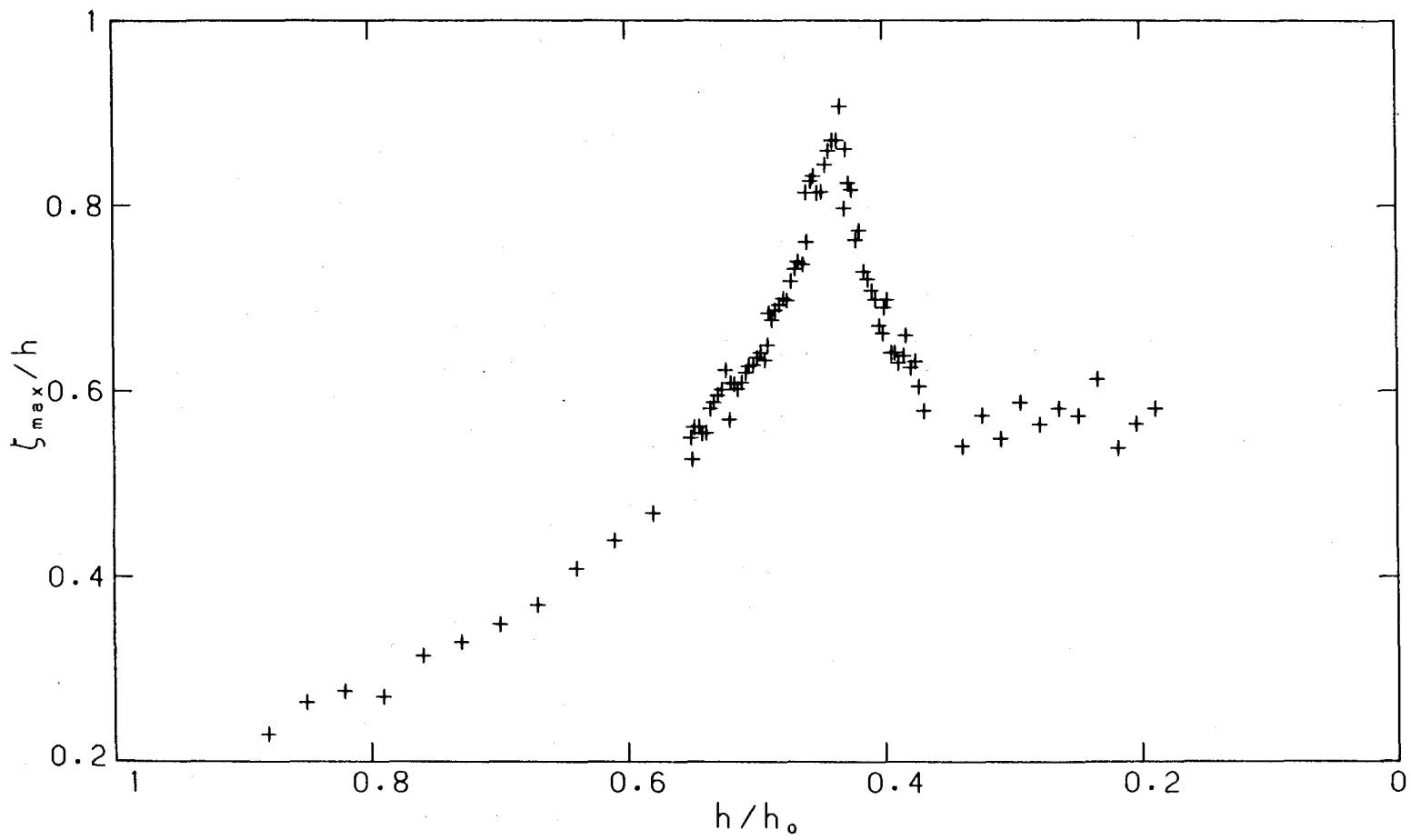


Fig. 5.10 Maximum amplitude variation for a spilling wave, case 1, normalized by the local depth.

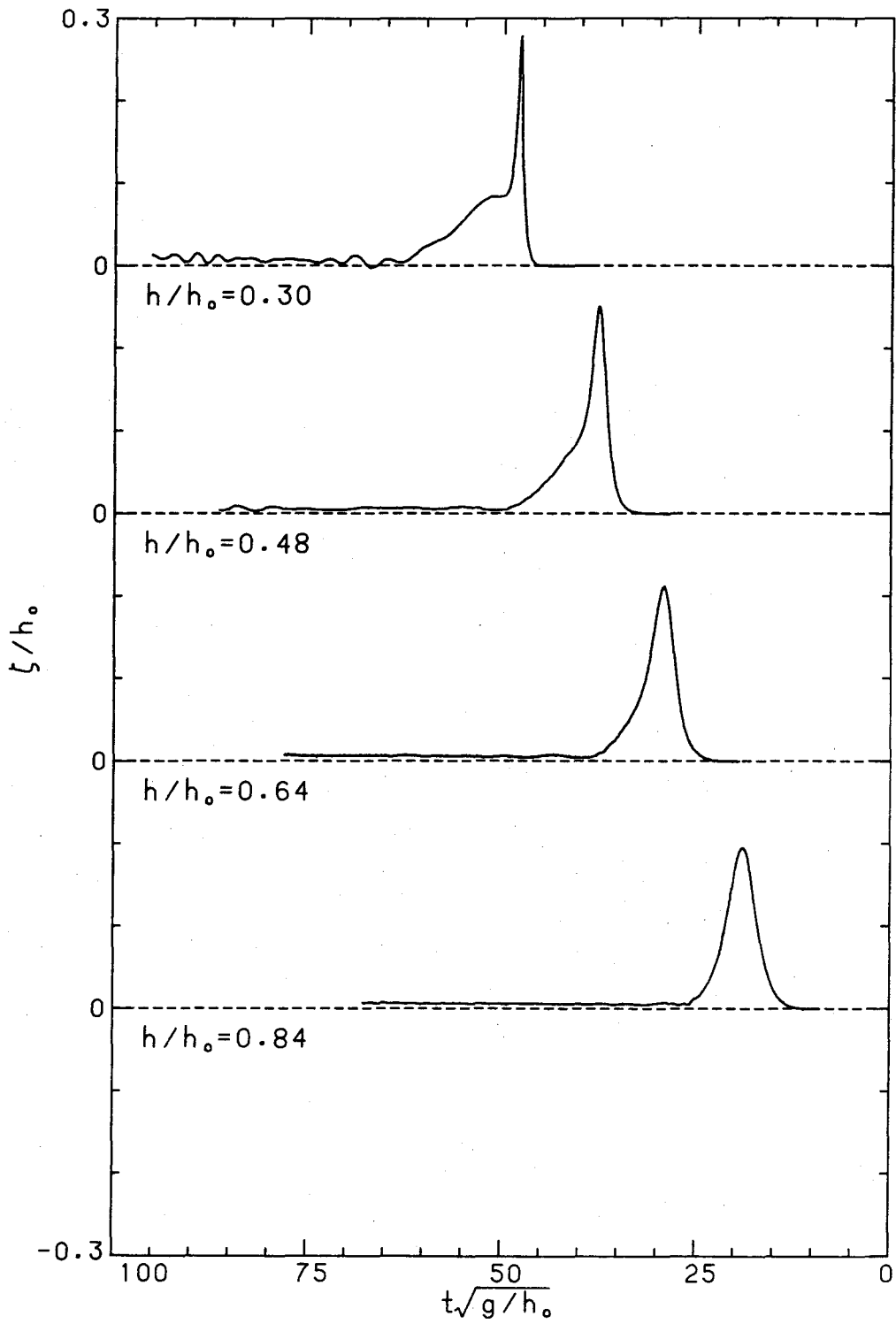


Fig. 5.11 Evolution of a solitary wave on a sloping bottom which breaks as plunger.

(1985). Peregrine gives an expression for the amplitude of the reflected wave as:

$$\frac{\zeta_r}{h_0} = \frac{1}{2} S \left(\frac{1}{3} \frac{H_0}{h_0} \right)^{1/2} \quad (5.1)$$

If there is a reflected wave, we would expect that its amplitude, after a sufficient amount of time, would be twice the value predicted from Eq. 5.1 at this location, since the wave paddle would reflect the reflected wave back up the beach. Eq. 5.1 gives $2\zeta_r/h_0=0.0049$ for this case compared to an experimental value of approximately 0.0056; hence, credibility is given to the existence of a reflected wave generated by a solitary wave on a beach. Synolakis (1986) also observed a reflected wave and a similar result in his investigations. As the wave travels along to $h/h_0=0.64$ and $h/h_0=0.48$, it continually steepens, and a tail (not part of the reflected wave) which travels with the wave, is seen to emerge on the trailing side of the wave. At $h/h_0=0.30$ the wave is at the breakpoint and has become very steep with a considerable amount of the wave's volume now residing in the tail. The oscillations, seen beginning at $t\sqrt{g/h_0} \sim 60$ in the profile at $h/h_0=0.3$ and near the end the record at $h/h_0=0.48$ are small oscillatory waves generated during breaking, and which propagate offshore. It should be noted that the maximum amplitude registered by the wave gage at breaking (which affects the record at $h/h_0=0.3$ presented in Fig. 5.11) is in error by 25%; this is discussed further in Section 5.3.3.

The maximum amplitude behavior for case 3 is shown in Fig. 5.12, together with data obtained by Camfield & Street (1969) and Saeki *et al.* (1971), who both performed experiments with solitary waves on a slope of 0.02. For this type of plot, the normalization is a bit awkward with h appearing on both axes, but it was chosen because of problems in presenting Camfield & Street's data in any other form. The data shown from this study are from the water mark measurements (see Section 4.5.3) and, because of their density and lack of scatter, they are presented here as a continuous line for clarity. Camfield & Street did not use constant values for the initial amplitude ratios for the waves used in their study but all were ~ 0.2 . The data from our study tend to line centrally within their's. Saeki *et al.*'s data, for all cases, consistently fall below those from this study. Their generation technique, of quickly releasing water into the wave tank to create a solitary wave, may be the reason for the discrepancy. The power laws of $-1/4$ and -1 can also be plotted (when adjusted for the normalization used for this figure) and would show good agreement with the data. After breaking, there are no measurements of ζ_{\max} from this study, but, from the data of others, we see the usual rapid decay and that the extent of the ZRD depends on the initial amplitude ratio. In the ZGD, ζ_{\max} follows a power less than 1 but greater than 0, and, thus, grows in a relative sense but, in an absolute sense, it is decaying.

The data for the plunging case from this study are presented in Fig. 5.13 separately from the others to clearly show the measured values. These data were obtained along the beach from near generation

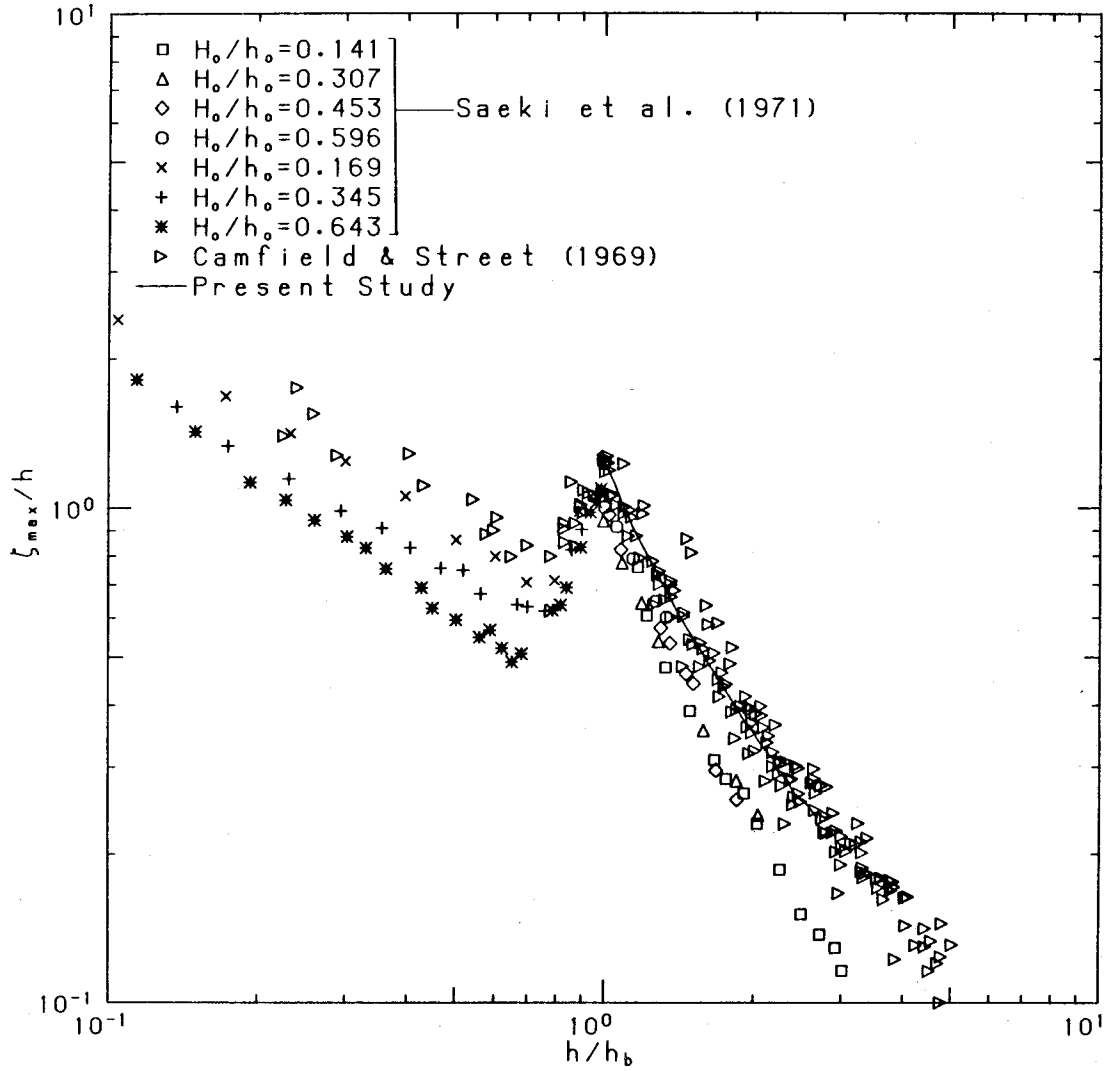


Fig. 5.12 Maximum amplitude variation for the plunging wave compared with Saeki et al. (1971) and Camfield & Street (1969).

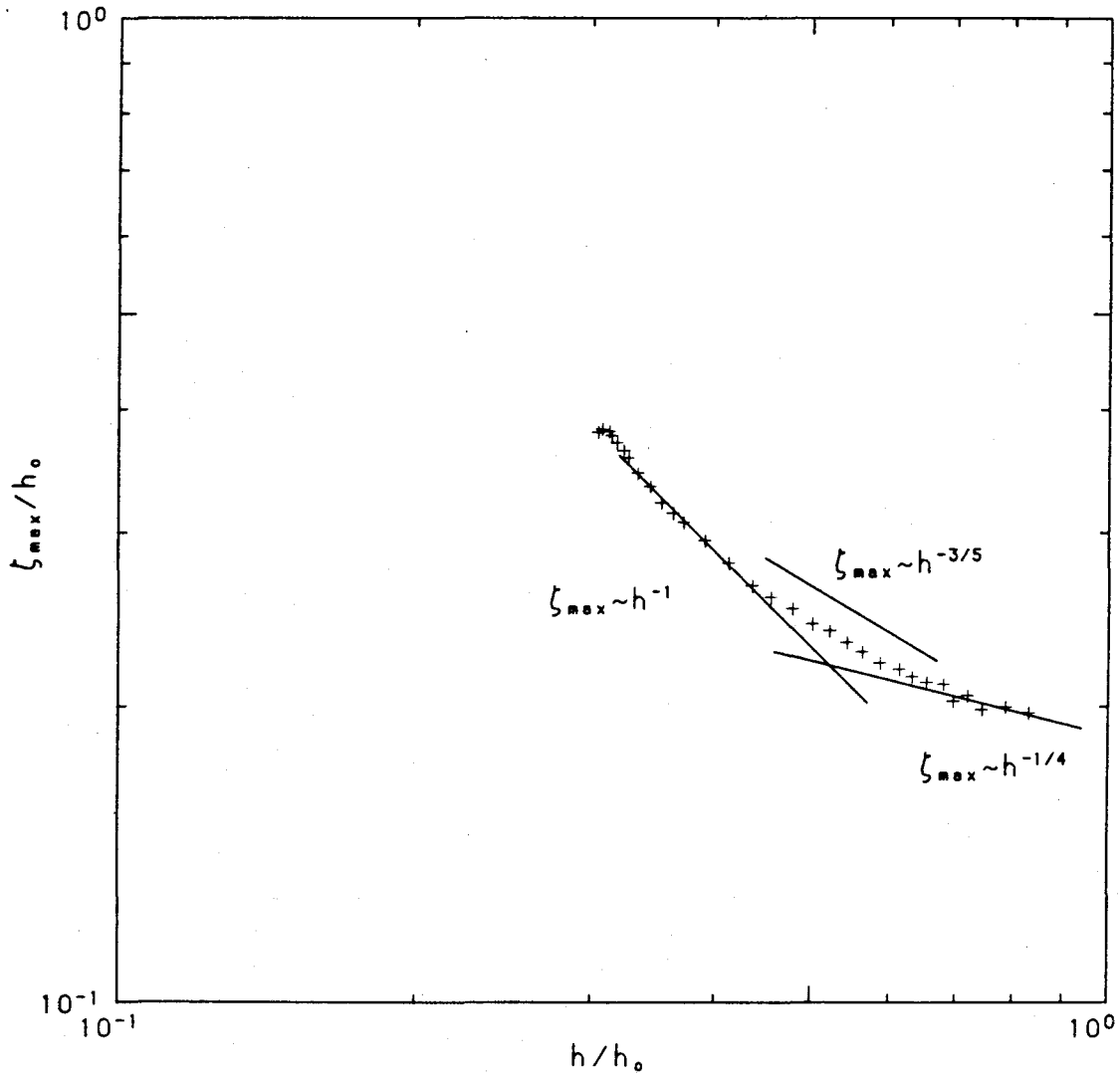


Fig. 5.13 Maximum amplitude variation, from water mark measurements, for the plunging wave case.

to the breakpoint. Near generation, ζ_{\max} appears to follow a power law close to $-1/4$ and somewhat later, as the wave propagates up the beach, a -1 power law. In the transition between these two regions, there is a definite trend which follows closely a $-3/5$ power law. Beyond the -1 power law region and up to the breakpoint, the growth rate of ζ_{\max} is slightly greater than the -1 power law. There are no theoretical explanations for the $-3/5$ and the less than -1 trends as there are for the power laws $-1/4$ and -1 .

Fig. 5.14 shows the celerity of the plunging wave along the beach. We see the same sort of behavior here as with the spilling wave case; the relative celerity increases while the absolute celerity decreases in the region before breaking. This case differs from the spilling case in that the rate of change in the celerity is larger here. Further, the actual celerity departs more from that computed using the equation for a solitary wave on a horizontal bottom. The source of the oscillations near $h/h_0=0.8$ is not known, but may be due to the wave generation technique. Again, we note the increase in celerity just before and continuing on after breaking.

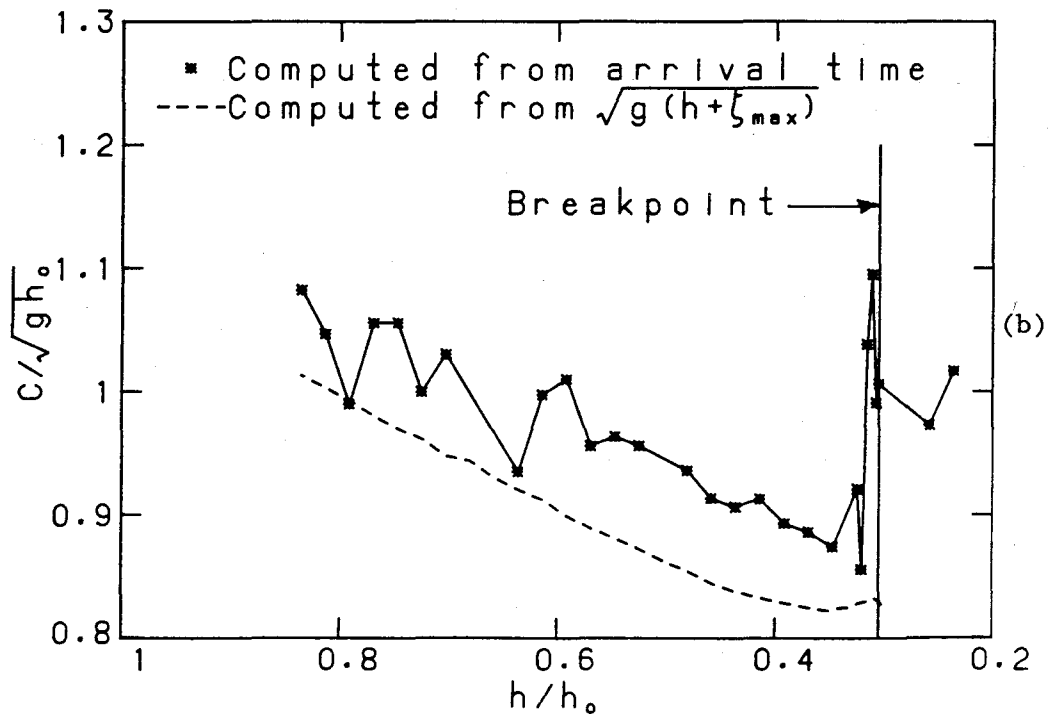
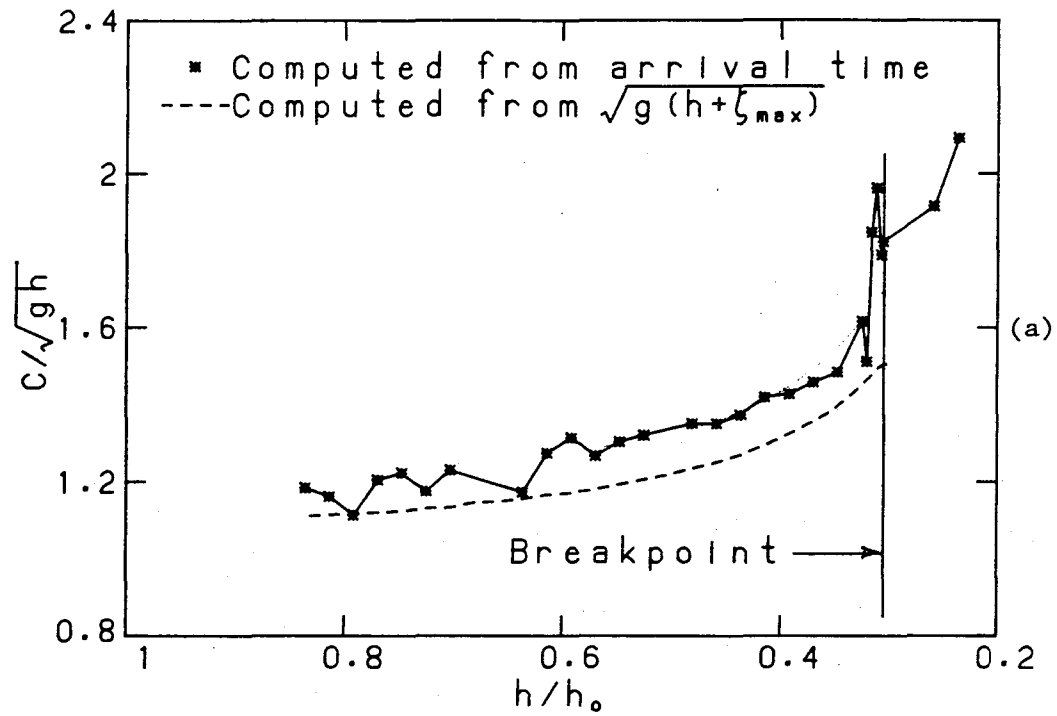


Fig. 5.14 Wave celerity for the plunging wave case; (a) normalized by the local shallow water wave speed, (b) normalized by the offshore shallow water wave speed.

5.3 *Kinematics at Breaking*

Before a presentation of the results of this section, the technique of inferring the spatial structure the flow field from single point measurements of the LDV will be discussed.

5.3.1 *Formation of the Flow Field*

The output from the LDV gives us a time series of horizontal and vertical velocity at a single point in space for any given experiment. In order to construct the flow field (by flow field is meant a time series given vertically through the depth) at some location along the beach, many time series, obtained at different vertical locations through the depth, were combined to form a single time series representing the flow field. Typically, measurement levels were spaced vertically at approximately one-tenth the local depth but were not always equally spaced. Any repeated measurements at the same vertical level were first averaged by simply summing the time series at corresponding times and then dividing by the number of measurements. The collection of time series used to construct the velocity field are presented as vectors on a rectangular grid using cubic-spline interpolation in both the vertical and time coordinates. Fig. 5.3 shows typical time series from the plunging wave case at breaking that were used in this type of formulation from five locations across the depth. Note that, above the undisturbed free surface, the signal is present only when the wave encases the LDV's laser beams and the photodetectors' lines of sight. It is clear, that for this type of

signal construction to be viable, it is essential to have a reproducible wave — hence, the motivation for the careful generation techniques used for this study.

To compute the total acceleration, we assume that the wave is of permanent form such that we can then use the transformation $x = -Ct$ to obtain velocity gradients in x . The value of C was obtained from Figures 5.8 and 5.14 for cases 2 and 3 respectively. This assumption seems reasonable since the time scale of a major change (e.g. overturning) in the wave shape is roughly two orders of magnitude larger than our sample period. It is realized that this is an approximation and the results obtained using it must be interpreted with caution. The above transformation yields the following expressions for the horizontal and vertical components of acceleration:

$$\frac{Du}{Dt} \cong \left(1 - \frac{u}{C}\right) \frac{\partial u}{\partial t} + w \frac{\partial u}{\partial z}, \quad (5.2)$$

$$\frac{Dw}{Dt} \cong \left(1 - \frac{u}{C}\right) \frac{\partial w}{\partial t} + w \frac{\partial w}{\partial z}. \quad (5.3)$$

The acceleration field was obtained from the constructed velocity field; time derivatives were computed using a cubic-spline, while spatial derivatives were computed using a 2nd degree least-squares polynomial fit with 3 neighboring points, the central point being the location of the desired derivative.

5.3.2 *Spilling Wave*

The overall view of the velocity and acceleration fields of a spilling wave (case 2) at breaking are shown in Fig. 5.15. The vectors shown in this figure, and others to follow, have lengths and directions indicating the magnitudes and directions of the velocity or acceleration at the base (end opposite arrowhead) of each. In the upper-right corner of each figure of velocity and acceleration fields are scales representing the measured celerity, C , and the acceleration of gravity, g , respectively. The solid line in the figure depicts the free surface elevation. At first glance, we notice some symmetry in the flow, but, on closer inspection, there are some obvious departures. Both velocities and accelerations are larger in the front portion of the crest and a time lag, in the vicinity of the crest, is noticed when traversing vertically through the flow field from top to bottom.

The details of the flow in the crest are revealed with an expanded section of the flow shown in Fig. 5.16. The maximum fluid velocity and acceleration shown in this figure are $0.73 C$ and $0.88 g$ respectively. Although measurements could not be made very near (limited by the curvature of the wave) the free surface, one can extrapolate (liberally) and find that the largest fluid velocity is still less than $0.8 C$. It is, more hazardous to extrapolate the accelerations to the surface, their trends being not as clear as the corresponding velocities near the crest. No conclusive evidence can be drawn from the data presented here on whether the fluid accelerations at and in the vicinity of the crest approach $1g$ near the surface. Hence, from

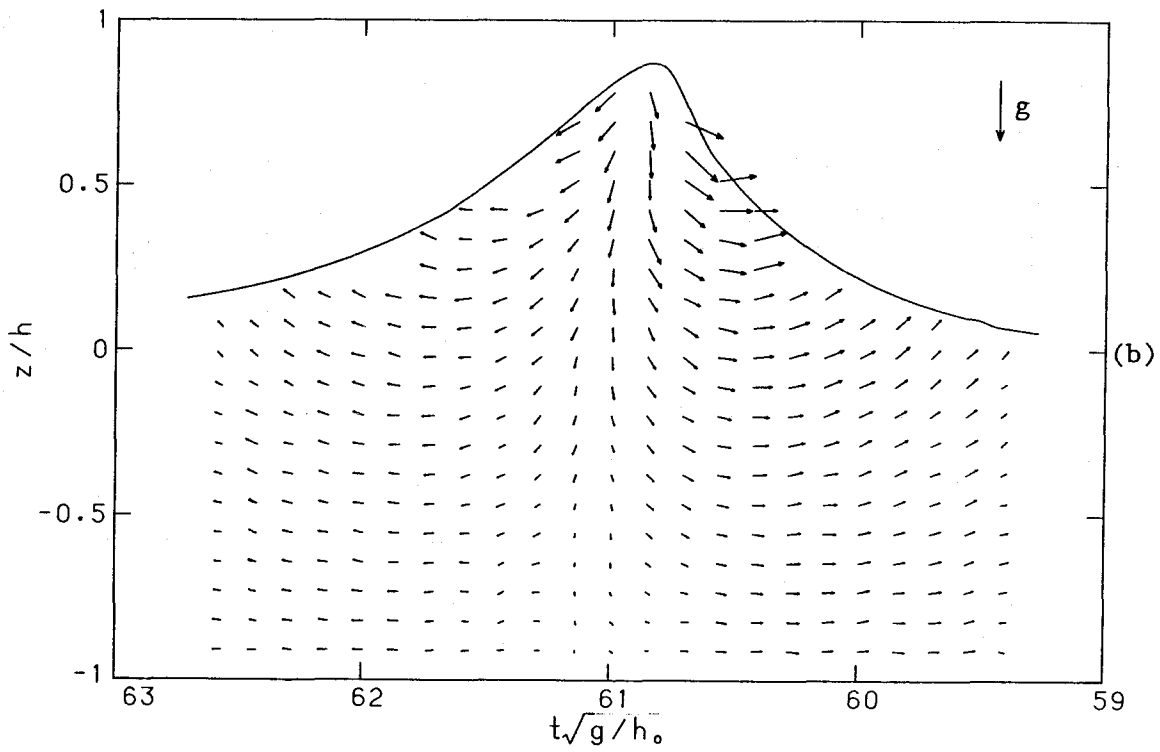
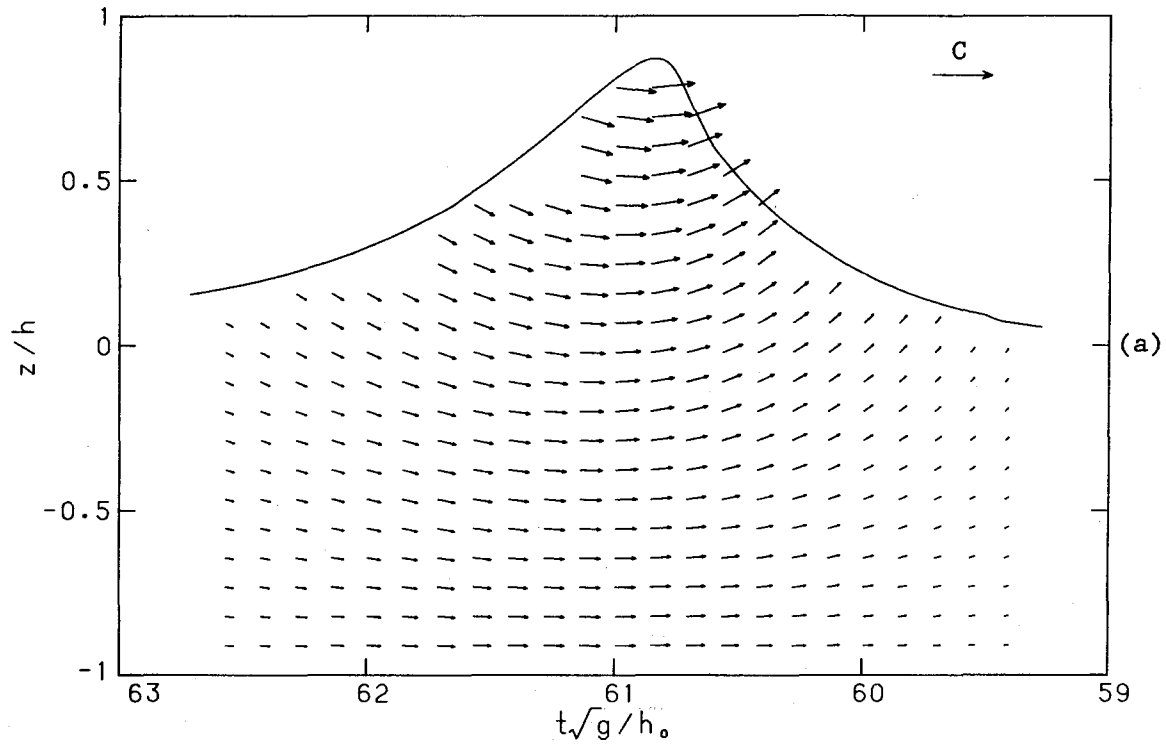


Fig. 5.15 Overall view of flow field of a spilling wave, case 2, at breaking; (a) velocity, (b) acceleration.

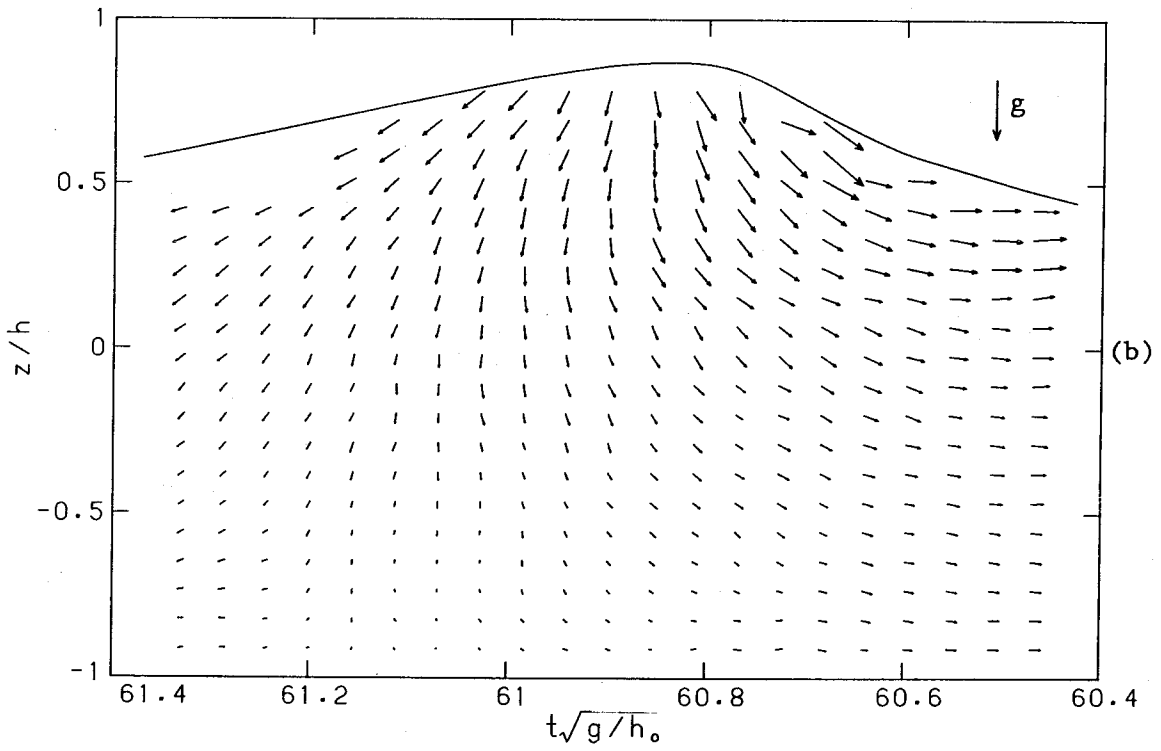
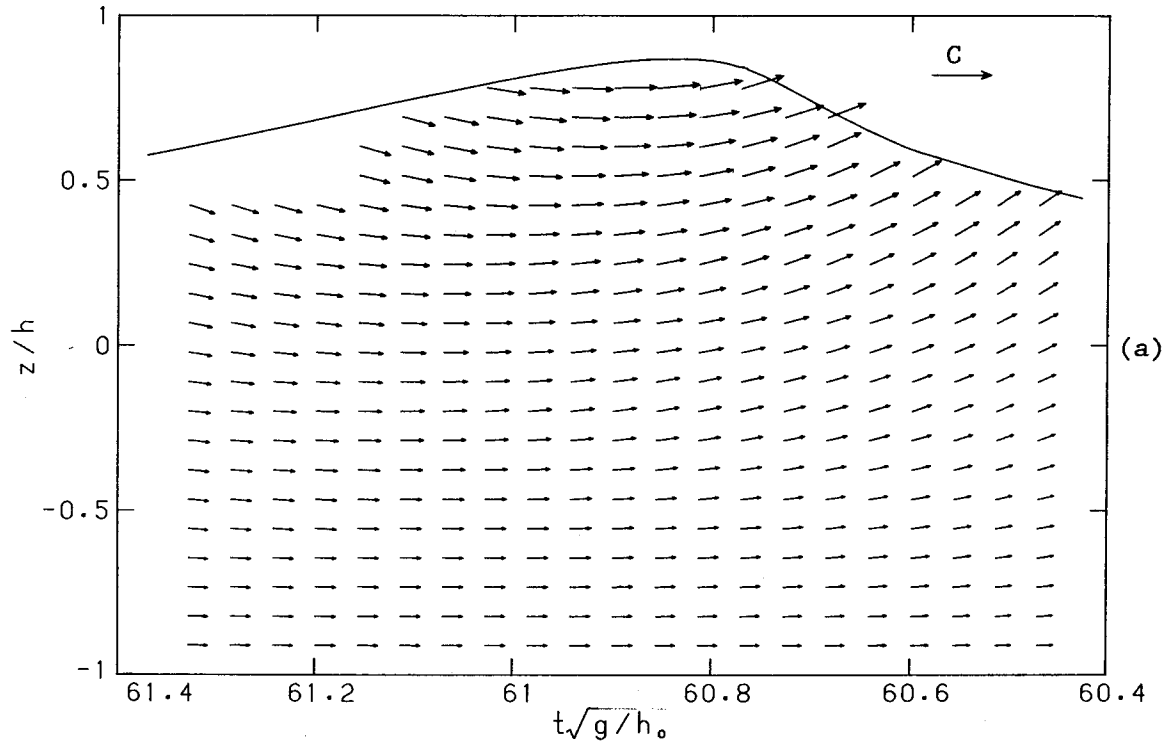


Fig. 5.16 Expanded view of flow field near crest of a spilling wave, case 2, at breaking; (a) velocity (b) acceleration.

Fig. 5.16b, no obvious indications of downward accelerations at the surface sufficient to produce a Rayleigh-Taylor instability is seen. This is bothersome; in that there is little evidence that the conditions necessary for the two acknowledged mechanisms for wave breaking do, in fact, occur.

It may be that, in a small localized region in the crest, so close to the surface that it cannot be reached by the LDV, the downward accelerations do approach $1g$. It appears very unlikely, though, that it is the fluid velocity at the crest exceeding C that results in wave breaking for this spiller considered.

Eight horizontal and vertical velocity profiles measured in the vicinity of the crest are shown in Fig. 5.17. The first and the last profiles are also shown with fitted lines. It was from such profiles that the flow fields, as shown in Figures 5.15 and 5.16, were constructed. This figure illustrates that the maximum horizontal velocity does not occur simultaneously at all positions vertically through the depth, above $z/h=0.4$ it is decreasing while at the same time it is increasing below. The changes in the horizontal velocity, over the span of time shown, are subtle for the most part with much of it occurring near the surface. The vertical velocity profiles are varying more rapidly than the corresponding horizontal velocity throughout most the depth, with some profiles showing positive and negative portions simultaneously.

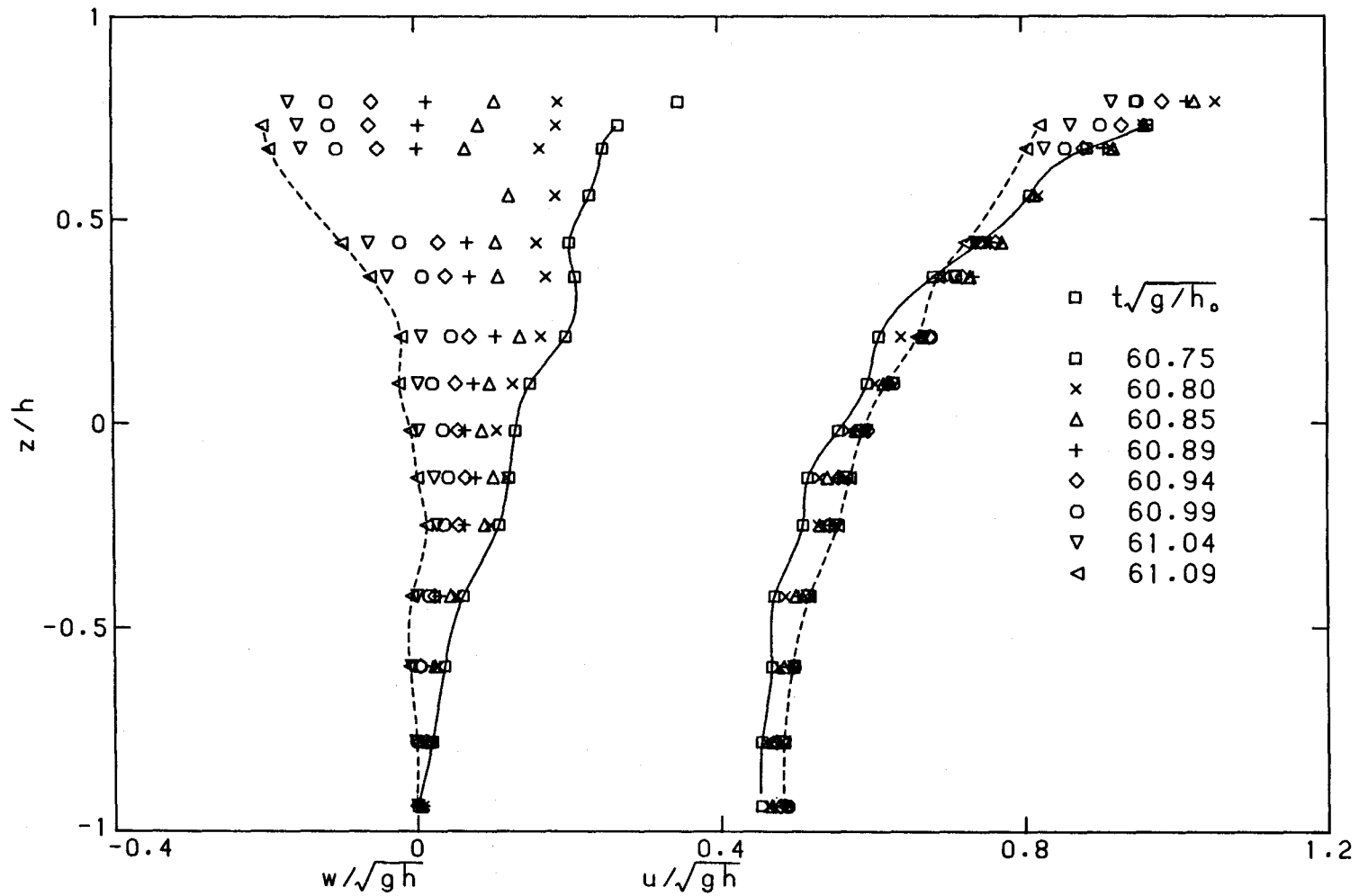


Fig. 5.17 Horizontal and vertical velocity distribution in the vicinity of the crest for a spilling wave, case 2, at breaking.

5.3.3 *Plunging Wave*

Before presenting the flow field for the plunging wave case, we discuss a problem associated with the wave gage measurement at breaking. A comparison of a wave profile digitized from a photograph with a profile obtained from a wave gage is shown in Fig. 5.18. The spatially defined profile from the photograph was transformed to the time coordinate using the transformation discussed in 5.3.1, while the wave gage record has been multiplied by the function $1 + 0.33 \left(\frac{\xi}{\xi_{\max}} \right)^2$. The wave gage's frequency response was apparently too low to capture the high frequency content of the signal corresponding to the steep portions of the wave profile in the vicinity of breaking. The choice of the above mentioned correction was reasoned from the fact that the higher amplitude portion of the wave is also the steepest, and, hence, more corrective weight is given to it. Although, exact agreement of a profile measured as a time series at a fixed location when compared to a profile obtained from a photograph is not expected, the adjusted profile seems to give a reasonable estimate of the surface at breaking. The wave gage registered a maximum value 25% lower than the that obtained from the photograph. Again, one should keep in mind that the line depicting the location of the free surface is not exact, but rather, it is an indication of where the location is likely to be.

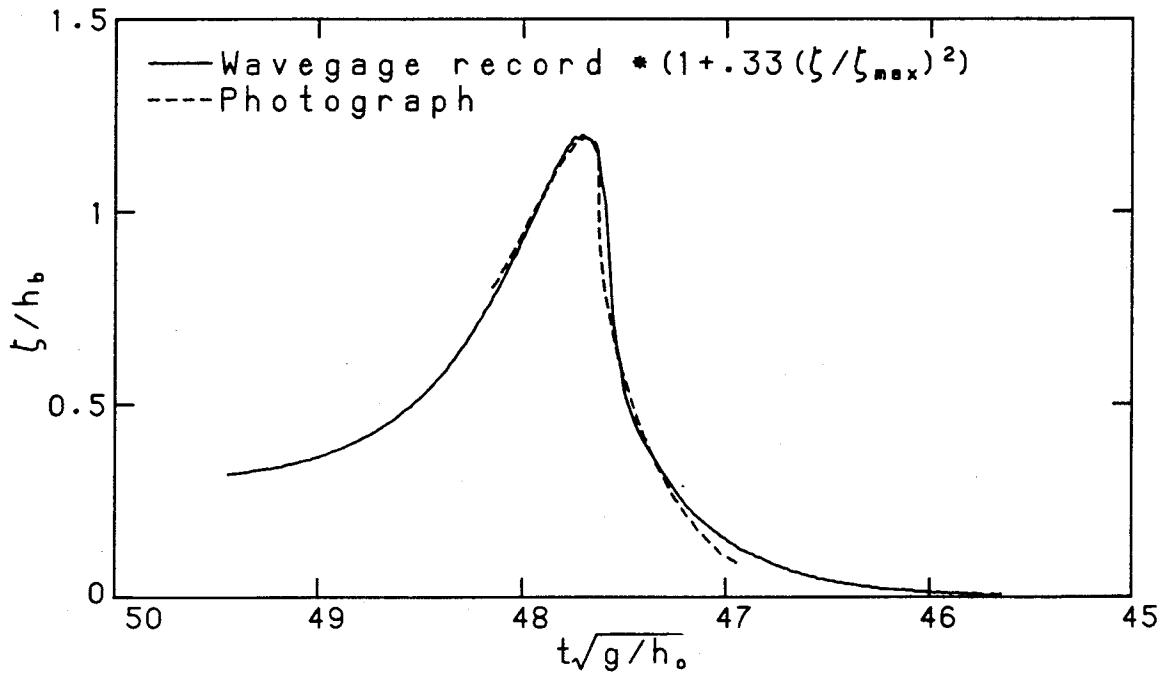


Fig. 5.18 Surface elevation measured by a wave gage compared with a photograph of the plunging wave at breaking; $h/h_0=0.30$.

Figures 5.19, 5.20, 5.21 and 5.22 show the flow field for the plunging breaker. We start with the overall view in Fig. 5.19, and go towards increasingly expanded views ending with Fig. 5.22, which centers on the front portion of the crest.

The overall view of Fig 5.19a shows the varied nature of the velocity field throughout the wave. Ahead of the crest, the flow near the surface feels a stronger effect in the vertical of the oncoming wave as one might expect due the steepness of the front face. In Fig. 5.19b at $z/h \sim 0.5$, the horizontal accelerations on the front face approach or exceed g , which is necessary to accelerate the fluid particles that will eventually become part of the overturning crest

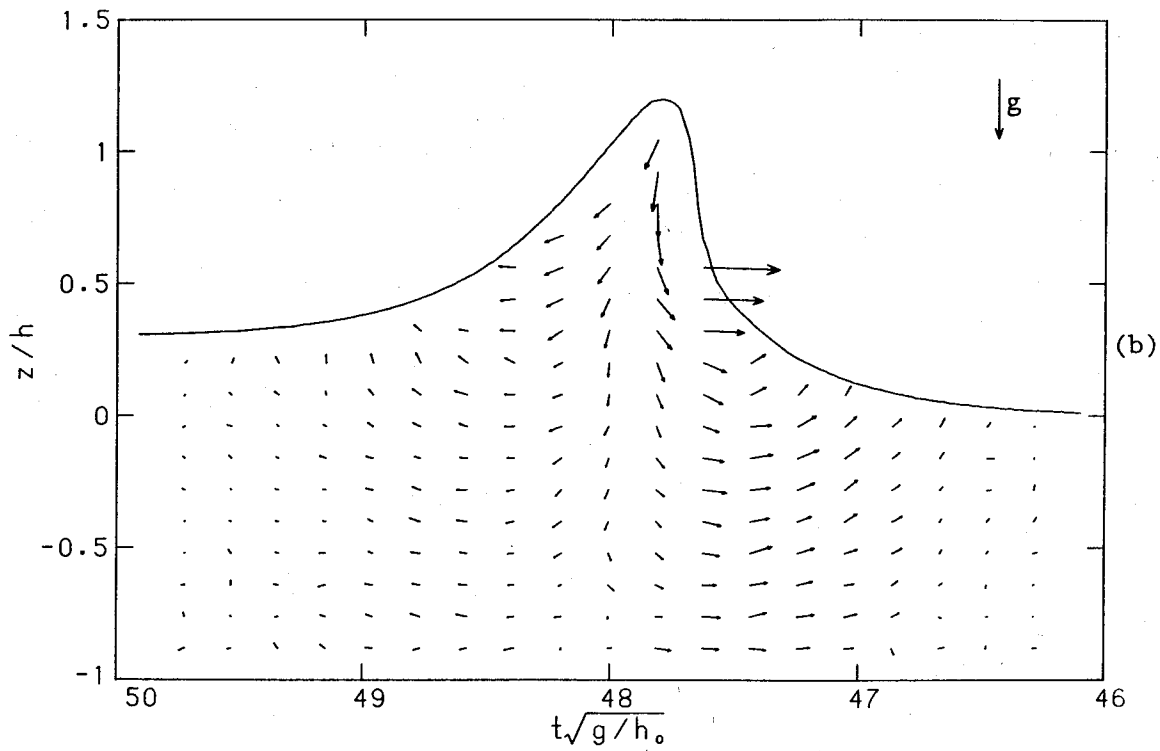
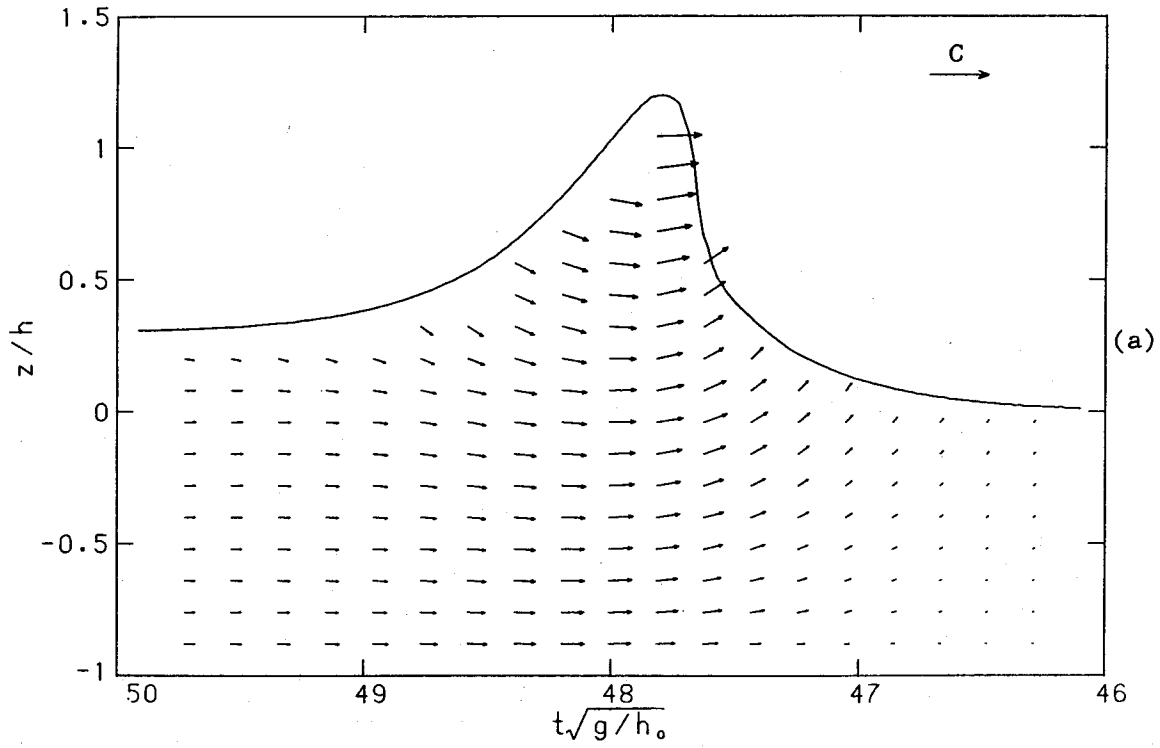


Fig. 5.19 Overall view of flow field of the plunging wave at breaking; (a) velocity, (b) acceleration.

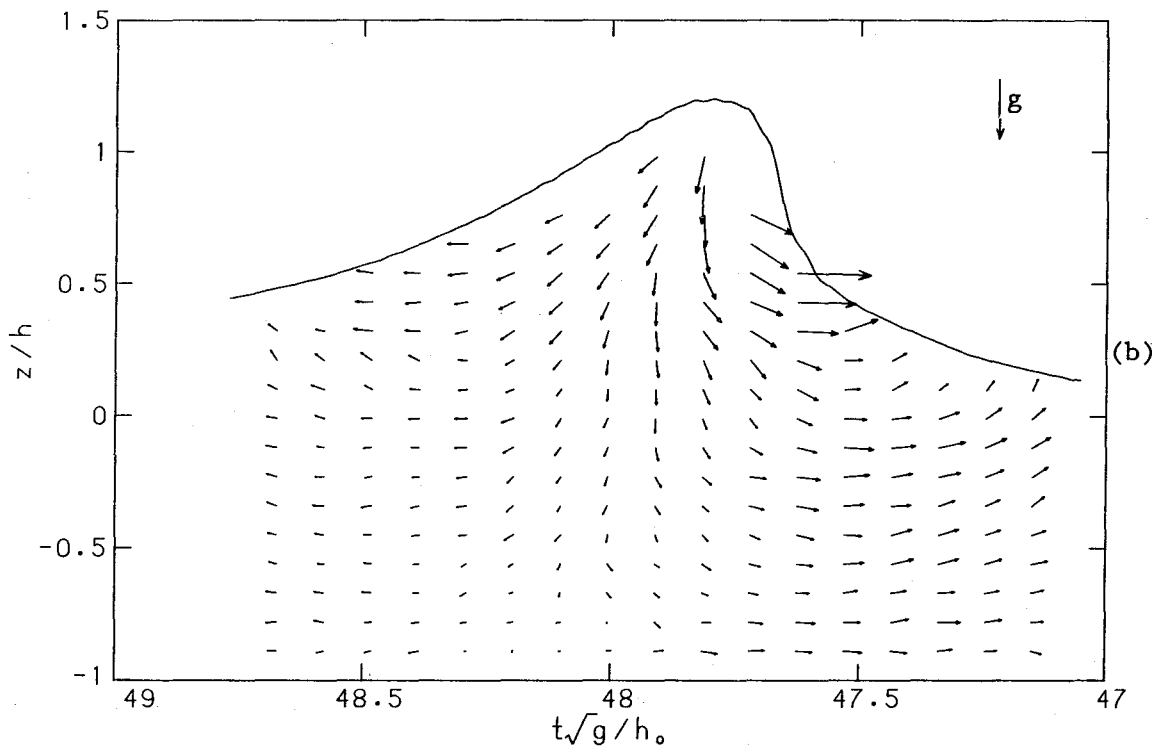
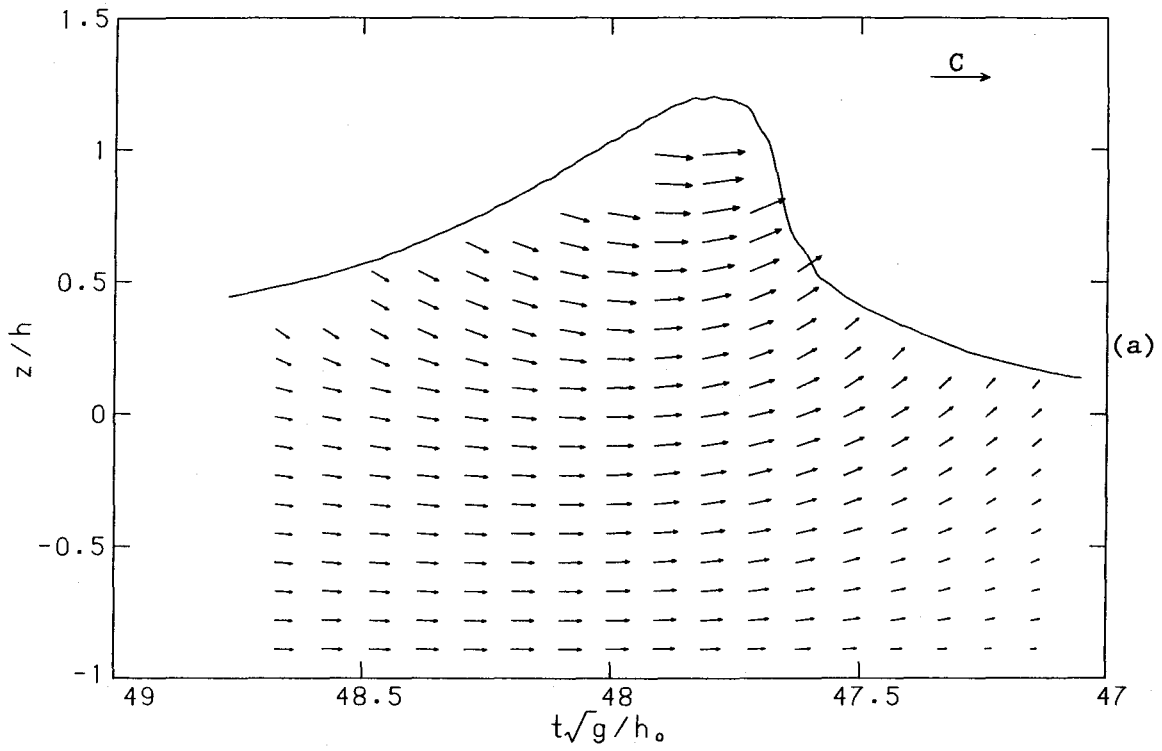


Fig. 5.20 Expanded view of flow field near the crest of the plunging wave at breaking; (a) velocity, (b) acceleration.

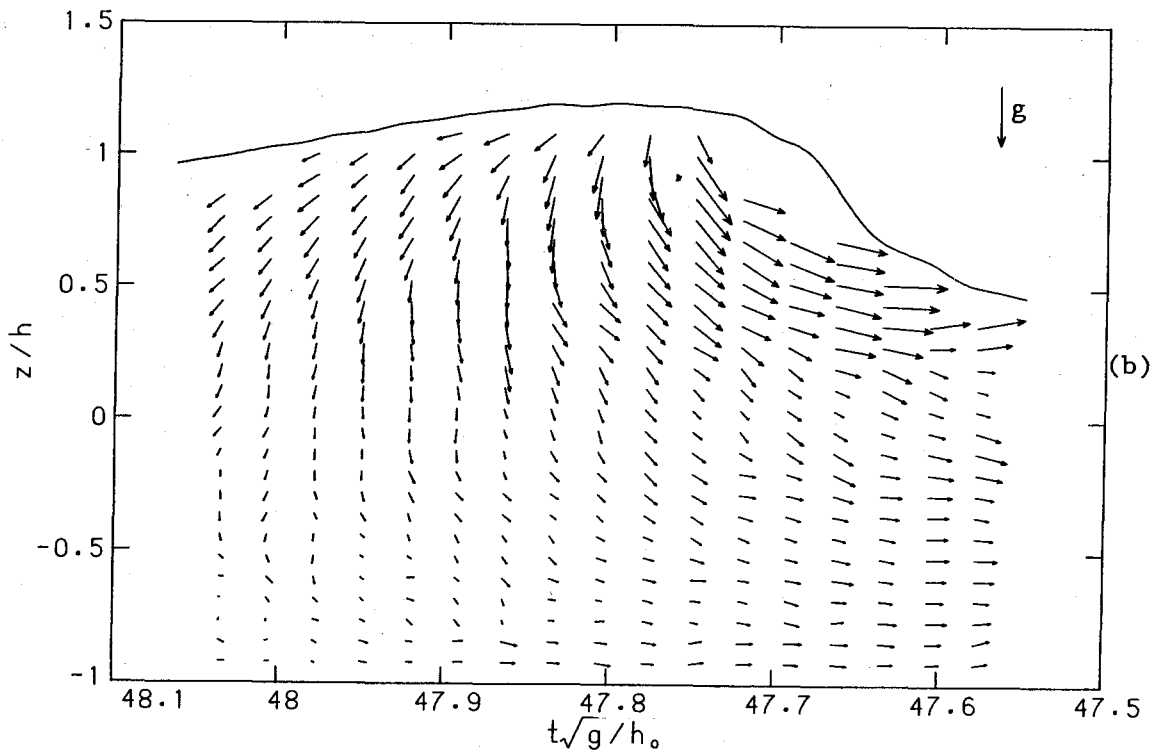
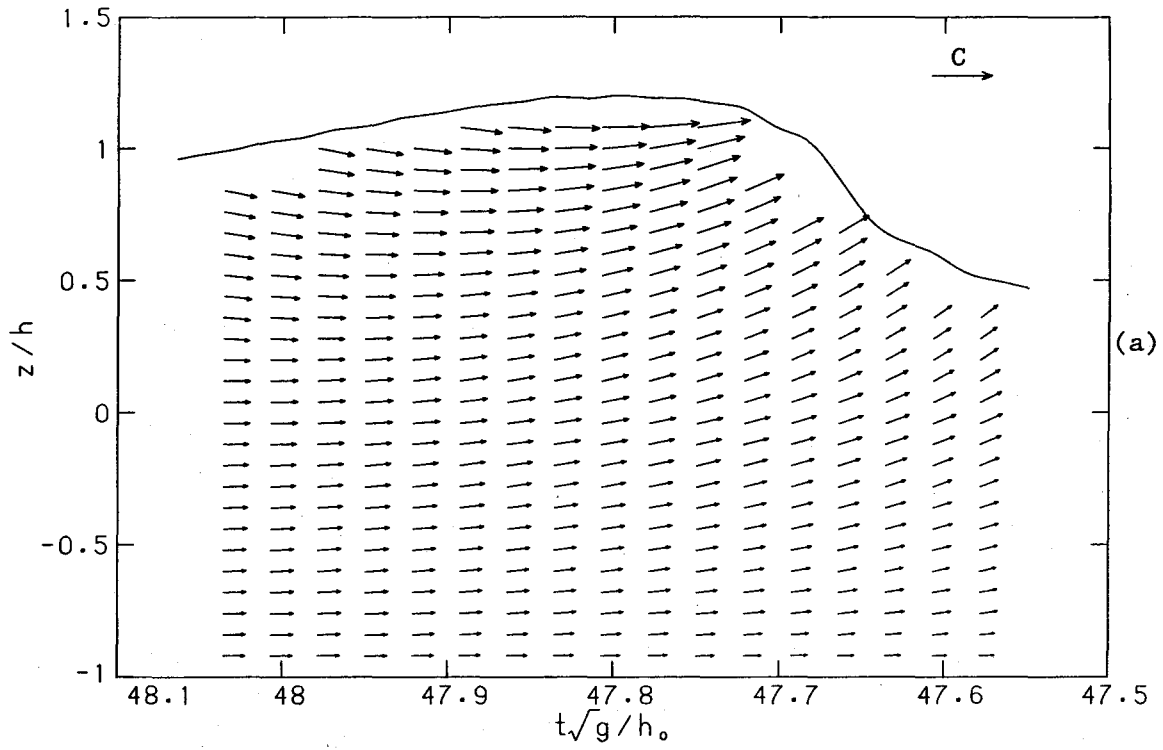


Fig. 5.21 Expanded view of flow field near the crest of the plunging wave at breaking; (a) velocity, (b) acceleration.

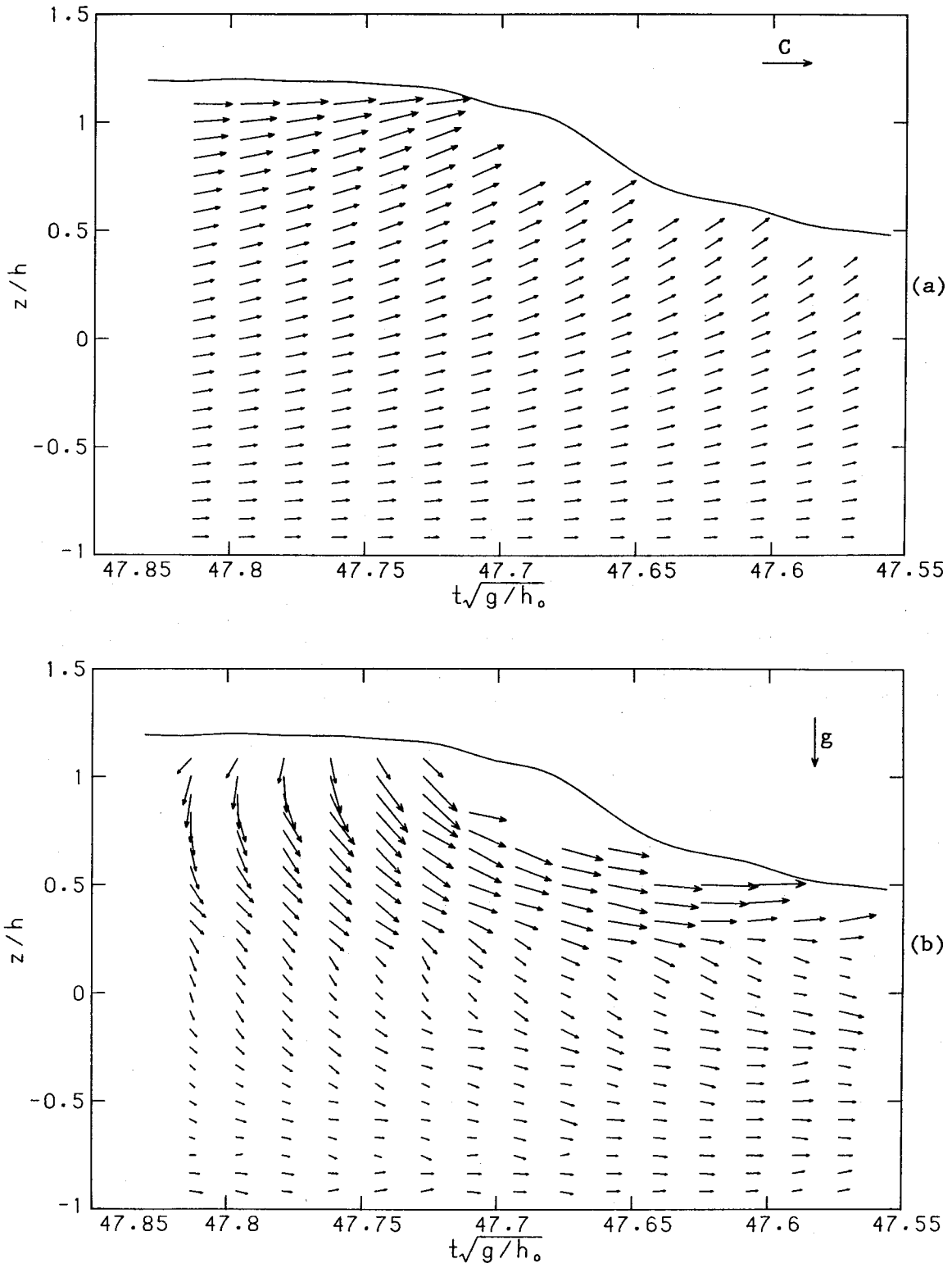


Fig. 5.22 Expanded view of flow field near the crest of the plunging wave at breaking; (a) velocity, (b) acceleration.

where the velocities must exceed C . On the trailing side of the crest, the accelerations are considerably smaller when compared to those on the leading side. In the tail region, the flow is nearly horizontal and constant across the depth. The time lag that was observed in the spilling case is present here and is clearly seen in Fig. 5.21.

Looking now at the expanded views, we examine some of the more subtle details. The velocities shown near the crest do not exceed C but are very close at $0.90 C$. If one extrapolates up to the surface, it seems plausible that they may exceed C . The extent of the high acceleration region in the front portion of the crest is large, with much of the flow in this vicinity having accelerations in excess of $1g$. Also, beneath the crest and away from the surface, a portion of the flow experiences vertical accelerations near $-0.8g$. At the crest near the surface, it appears that the accelerations are diminishing, which is consistent with Equations 5.1 and 5.2 since $(1 - \frac{u}{C}) \rightarrow 0$ and $w \rightarrow 0$.

Peregrine *et al.* (1980) give a description of three dynamically important regions in a wave approaching breaking; the results found here, for a plunger breaker, support them. The three regions they found were based on a numerical study and include: 1) a region at the crest where the water particle velocities exceed C , 2) a thin region on the front face of the wave where the accelerations exceed g and 3) a region on and beneath the trailing side of the crest where the accelerations are low. They also note that, in the crest region, the

velocities and accelerations are pointed in similar directions while at the same time being large. Other numerical studies, such as those of Cokelet (1979) and Vinje and Brevig (1980), also compare well qualitatively to our measurements.

Eight horizontal and vertical velocity records, sampled during the passage of the crest, are shown in Fig. 5.23. It should be noted that, at the particular location in the wave tank where these measurements were made, there was difficulty in aligning the LDV near the bottom. The variations seen in the horizontal velocities near the bottom may be a result of that problem. Again, it can be seen that the maximum horizontal velocity, through the depth, does not occur simultaneously; the figure shows a decreasing velocity with time above $z/h \approx 0.7$ and increasing with time below. As was the case with the spilling breaker the horizontal velocities vary mainly near the surface. At $z/h \approx 0.7$ it is interesting to note that the change in the horizontal velocity is very small over the time span shown. The vertical velocities near the surface are varying rapidly with the largest value occurring somewhat below the crest at $z/h \approx 0.8$. It is interesting to compare the spilling and plunging waves using the information from Figures 5.17 and 5.23. The horizontal velocity variations over the entire depth are larger in a relative sense for the plunging case, with u/\sqrt{gh} ranging from near 0.55 at the bottom to roughly 1.45 near the crest. The corresponding values near the bottom and near the crest are 0.45 and 0.90 respectively for the spilling breaker. Note, the spilling breaker's vertical velocity, in a relative sense, has a wider range of variation

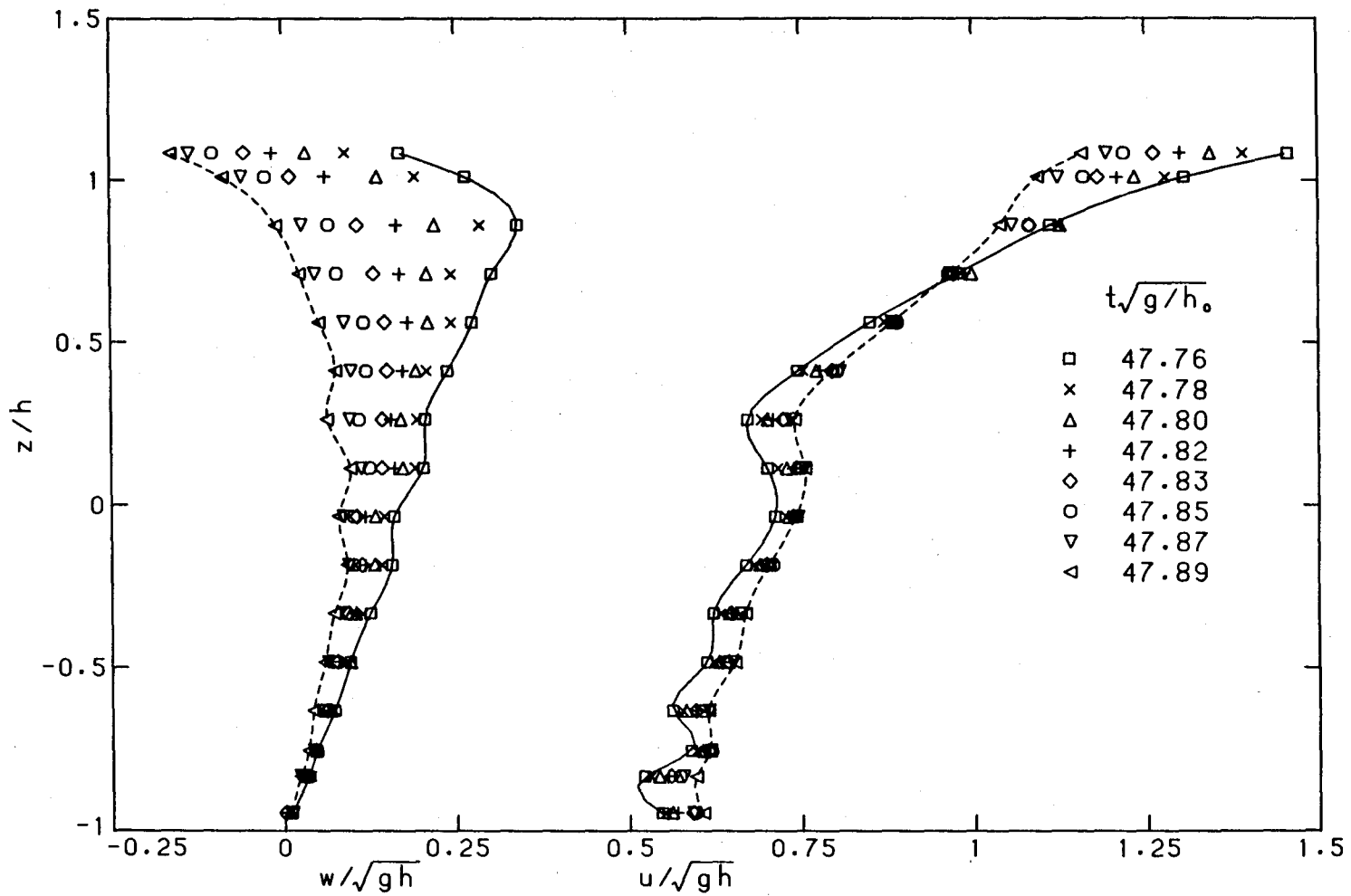


Fig. 5.23 Horizontal and vertical velocity distribution in the vicinity of the crest for the plunging wave at breaking.

near the crest than do the corresponding vertical velocities of the plunging wave. This is most likely due to the higher curvature of the plunger's free surface, hence the LDV's beams were not all encased in the flow to record the velocities there.

5.4 *Counter-rotating Vortices*

Unsatisfied with the notion that the vortices generated during the early breaking phase are co-rotating (e.g. see Peregrine 1983 or Basco 1985), an effort was made to determine if, indeed, the vortices were counter-rotating. Photographs of waves at a stage when the breaking tongue is fully developed, such as the one in Fig. 2.4f, lend support to the existence of counter-rotating vortices. We illustrate this stage of breaking in Fig. 5.24. In this illustration we hypothesize a possible arrangement of the counter-rotating vortices using the free surface shape and the penetration of air bubbles into the flow as a guide. We still do not know the mechanism by which these vortices are set up, at this stage they are only hypothesized to exist.

It is difficult to learn much about the vortices in a breaking wave when using a single point instrument such as the LDV. However, it may be assumed that they do exist, say in an arrangement similar to that shown in Fig. 5.24, such that an idea of how their signature would manifest itself in the LDV velocity traces could be formed. For instance, we consider the simple case when counter-rotating vortices are lined up as shown in Fig. 5.25. Taking paths from right to left

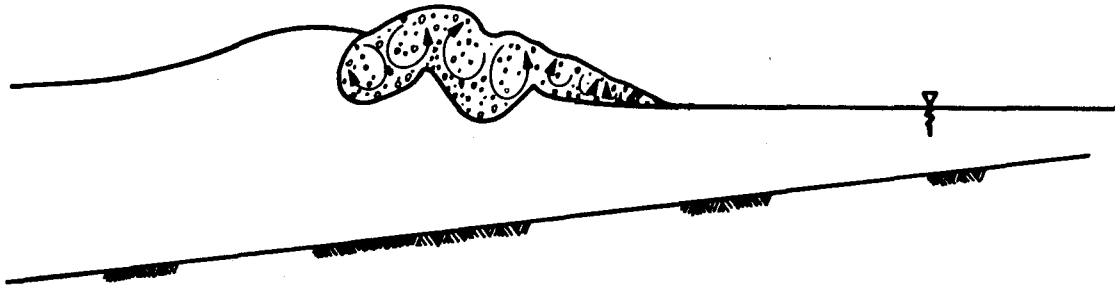


Fig. 5.24 Illustration of the counter-rotating vortices in the breaking tongue of a plunging wave.

that pass below, above and through the line of vortex centers, which we represent by A-A, B-B and C-C respectively, we will look at the direction of the velocity vector at locations along each of the paths. We can consider that, either the vortices are fixed and that velocities will be measured passing through them, or that the point of measurement is fixed and that the vortices are moving to the right (and also downward for path C-C).

Passing below the vortex centers, on path A-A, the velocity vector's direction continually rotates in the clockwise direction. The concern is not with the smoothness of the rotation, but only that its net rotation is clockwise, with one complete rotation after passing each vortex pair. On path B-B we see the opposite effect, the velocity vector's net rotation is in the counter-clockwise direction with again

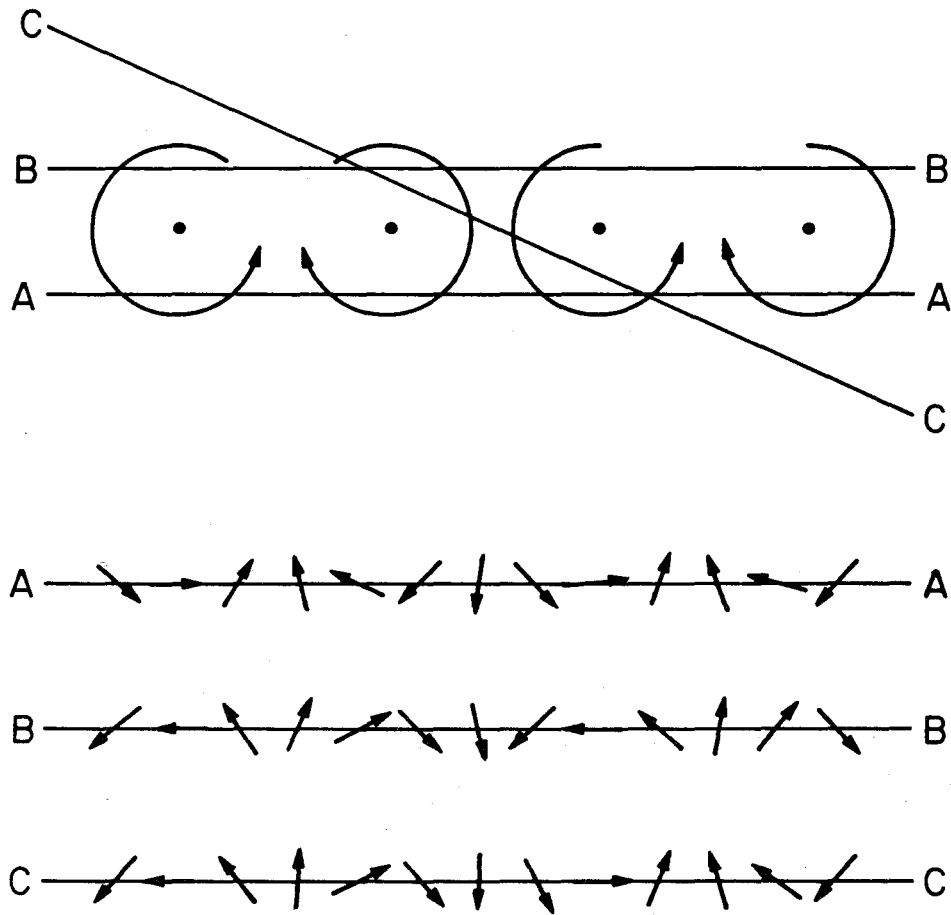


Fig. 5.25 Velocity vector rotation for various paths through counter-rotating vortices.

one complete rotation for each vortex pair. Finally, on path C-C, which passes through the vortices, the velocity vector's rotation is clockwise when beneath the level which passes through the centers of the vortices and counter-clockwise when above. One can repeat this simple analysis with co-rotating vortices; the significant outcome is that there is no complete rotation of the velocity vector's direction on any of the paths.

So how does this discussion of various paths through vortices relate to vortices in breaking waves? For the situation in the laboratory, the LDV is fixed while the vortices translate past the point of measurement. It is unlikely that the vortices in the breaking tongue, or elsewhere, will be as nicely ordered as shown in Fig. 5.25. As long as they are distributed somewhat along a line in the direction of wave motion, however, it is plausible that they will take a path through the measurement point in a manner similar to that assumed in our idealized discussion. This provides a starting point from which to demonstrate the existence of counter-rotating vortices in the breaking wave.

5.4.1 *Early Breaking*

Probing of the flow in the breaking tongue is hampered by its transient nature and the substantial amount of air entrained into the flow. The air entrainment renders the flow opaque to optical instruments and inhospitable to intrusive instruments. Information, however, can be gained by inspecting the flow away from but near the breaking tongue. Fig. 5.26 shows five velocity records from the plunging wave case measured at $h/h_0=0.25$ and at an elevation of $z/h=-0.04$. At this location along the beach, the breaking tongue, when centered at the measurement location, was at a stage similar to that shown in Fig. 2.4f. The elevation of $z/h=-0.04$ was chosen in order to approach beneath and as close as possible to the breaking tongue while, at the same time, staying far enough away that a sufficiently long

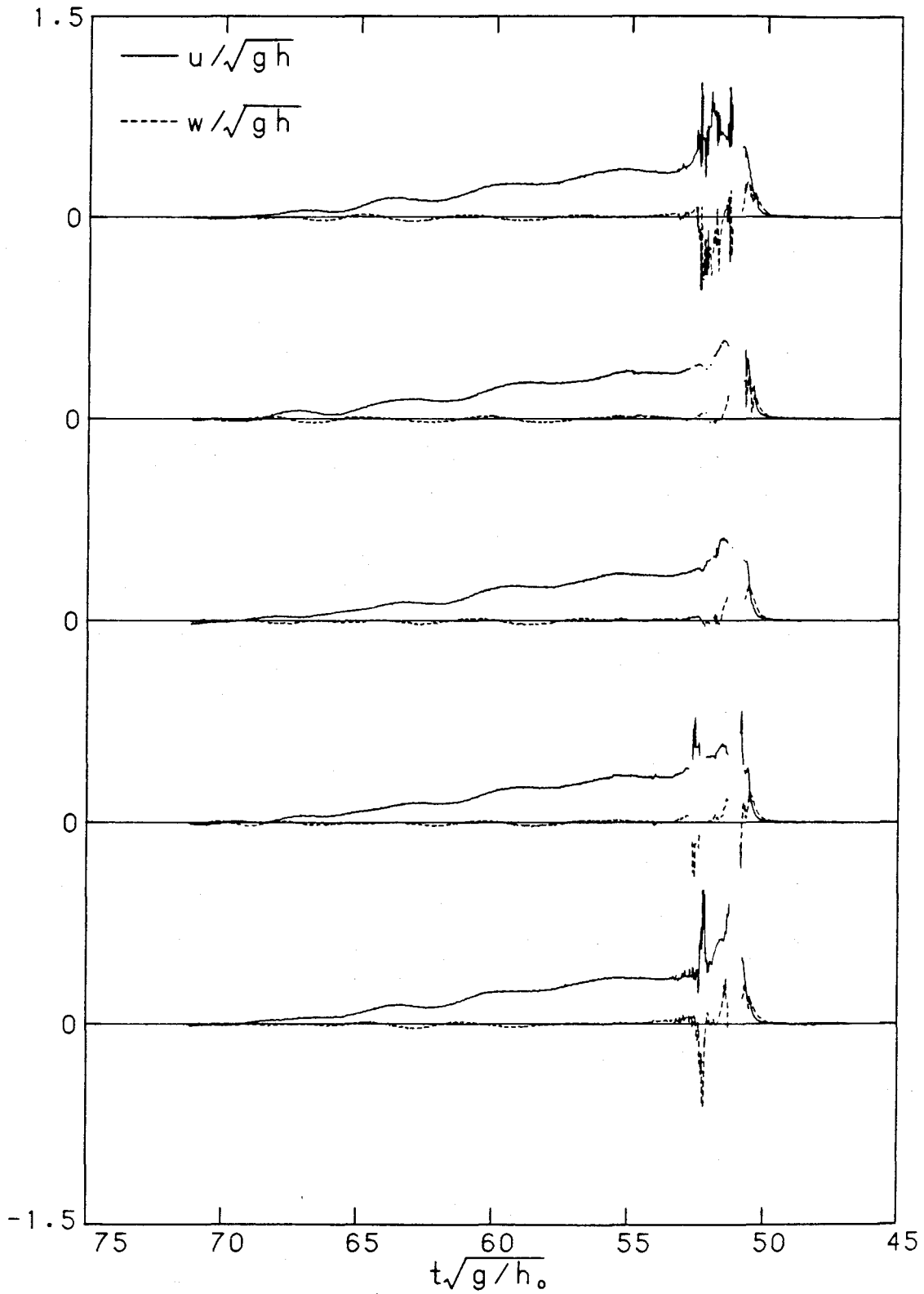


Fig. 5.26 Velocity time series in the after breaking region of the plunging wave, $h/h_0=0.25$ and $z/h=-0.04$.

velocity record was obtained before the entrained air in the flow disrupted the signal. Although photographs taken at this stage of breaking seem to indicate a situation which is repeatable in some detail, the velocity traces in Fig. 5.26 indicate variability in the crest region which is probably a result of three dimensional effects. Such effects may not be as apparent in photographs since the information in the flow is integrated across the tank.

To investigate the existence of counter-rotating vortices in the breaking tongue, we will look at the leading edge of the velocity traces in Fig. 5.26, before the disruption of the signal from the entrained air. Presented in Fig. 5.27 are the fluctuations in the velocity signals due to the presence of the hypothetical vortices in the breaking tongue. These traces are the result of averaging the five sets of time series in Fig. 5.26, at corresponding times, to form a single time series, and then, subtracting the average from each of the time series that formed it. It was necessary to remove the average, which is assumed to represent a mean flow, so that the induced velocity fluctuation from the vortices could be examined. Again, we see variability between signals, there is, however, a consistent outcome from each of them. Take for instance, the horizontal and vertical velocity traces shown second from the top in Fig. 5.27. Constructing the velocity vector at $t\sqrt{g/h_0}=50.5$, with u roughly equal in magnitude to w but positive, yields a direction of -45° . Moving forward in time, u is becoming less positive while w becomes increasingly more negative; the vector's direction is rotating clockwise and continues to do so.

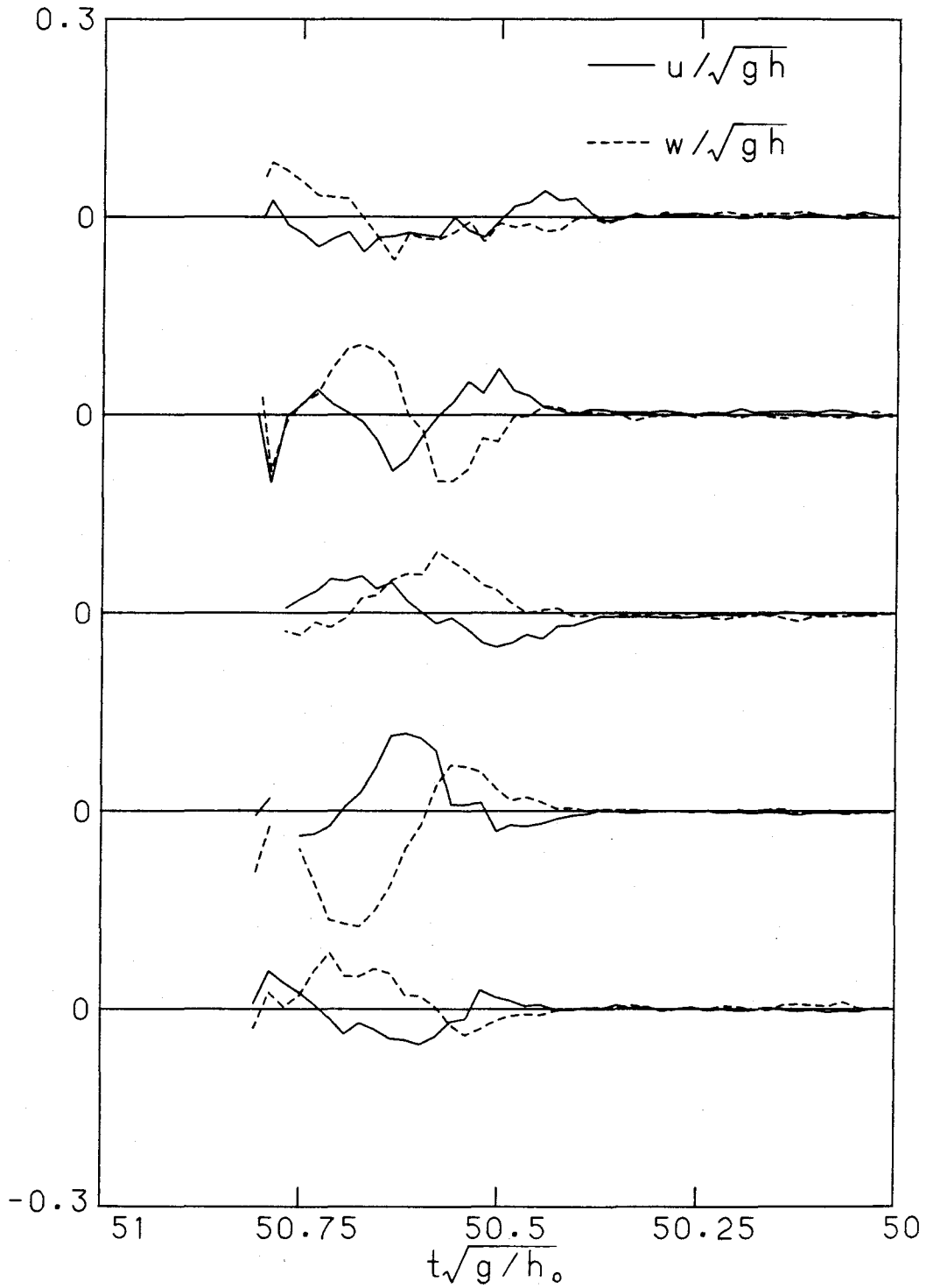


Fig. 5.27 Velocity fluctuations due to the presence of counter-rotating vortices in breaking tongue of the plunging wave.

The same result is seen from each of the other velocity traces. As the measurements were made below the vortex centers, we expect the rotation of the vector to be the similar to what was shown for path A-A in Fig. 5.25; and this is the case.

The above result considered during early breaking certainly supports the existence of counter-rotating vortices but it is limited. To further investigate counter-rotating vortices created from wave breaking, we will consider a later period when a turbulent wake has been established. Before discussing those results, however, we must first introduce a filter which was used to process the velocity time series.

5.4.2 *Filtering*

To obtain the results to follow in this chapter, it was necessary to filter the velocity signals. The entrained air in the flow often blocked the LDV's measurements and consequently left gaps of arbitrary size and at arbitrary times in the velocity records. Time series of this nature are not easily filtered and, hence, a simple technique was adopted to filter the time series obtained. Using $G(t)$ to denote the time series we wish to filter, we define our filtered function as:

$$\hat{G}(t) = \frac{1}{T} \int_{t-T/2}^{t+T/2} G(s) ds . \quad (5.4)$$

This transformation can be thought of as a box, centered at t and with

width T , which runs along the input $G(t)$. The output at t is simply the average of everything in the box. This type of lowpass filter commonly goes by the name *moving average* and has a cutoff frequency of approximately $1/T$.

Now, to accommodate discrete data with the gaps that have been discussed above, we use Eq. 5.4 and define the filtered time series at the i^{th} sample, t_i , to be:

$$\hat{G}(t_i) = \frac{W[G(t_i)]}{N_w} \left\{ G(t_i) \left[1 + 2 \sum_{j=1}^{(N_w-1)/2} \left[1 - W[G(t_{i-j})]W[G(t_{i+j})] \right] \right] \right. \\ \left. + \sum_{j=1}^{(N_w-1)/2} \left[G(t_{i-j}) + G(t_{i+j}) \right] W[G(t_{i-j})]W[G(t_{i+j})] \right\}, \quad (5.5)$$

where W is defined as:

$$W[G(t_i)] = \begin{cases} 0 & \text{if } G(t_i) \text{ invalid} \\ 1 & \text{if } G(t_i) \text{ valid} \end{cases}, \quad (5.6)$$

the variable G being considered invalid when there are no data at t_i . The adjustable parameter for the filter is N_w (odd) and, in a loose sense, we can consider the cutoff frequency to be $\frac{1}{\Delta t N_w}$, where Δt is the sample period. This filter is similar to the one described by Eq. 5.4 and can be thought of as a box which runs along the signal and the filtered output, $\hat{G}(t_i)$ is the average of every value in the box. But the gaps in the signal have been accounted for by removing the portion of the signal which lies symmetrically about the center of the

box from the gap. If there are any gaps, addition weight, equal to the weight of the gaps, is given to the central point in the box. This procedure avoids biasing of the average in the box. Note that no average is computed at t_i if $G(t_i)$ is invalid; in other words, data are not generated where none was obtained. The performance of the filter for values of N_w of 15, 35, and 59 is demonstrated in Figures 5.28a, 5.28b, and 5.28c respectively. The test signal is the horizontal velocity measured at $h/h_0=0.21$ and $z/h=-0.52$. The high frequency content can also be obtained by subtracting the filtered signal from the original signal which is also shown in the figures.

The above filter could also be used to bandpass a signal which we define as:

$$G_{bp} = \hat{G}_m - \hat{G}_n, \quad n > m, \quad (5.7)$$

where \hat{G}_j is \hat{G} evaluated with $N_w = j$.

5.4.3 Vortices in the Wake

As the plunging breaker propagates up the beach, beyond the stage illustrated in Fig. 5.24, it will eventually take on a form similar to that shown in Fig. 5.29a (Fig. 5.24 is also included in this figure for comparison). Here it has reached a stage commonly referred to as a quasi-steady bore, and is in, what we have termed, the ZGD. By the time the wave reaches this stage of breaking, the vortices in the breaking tongue have become part of the turbulent wake behind the

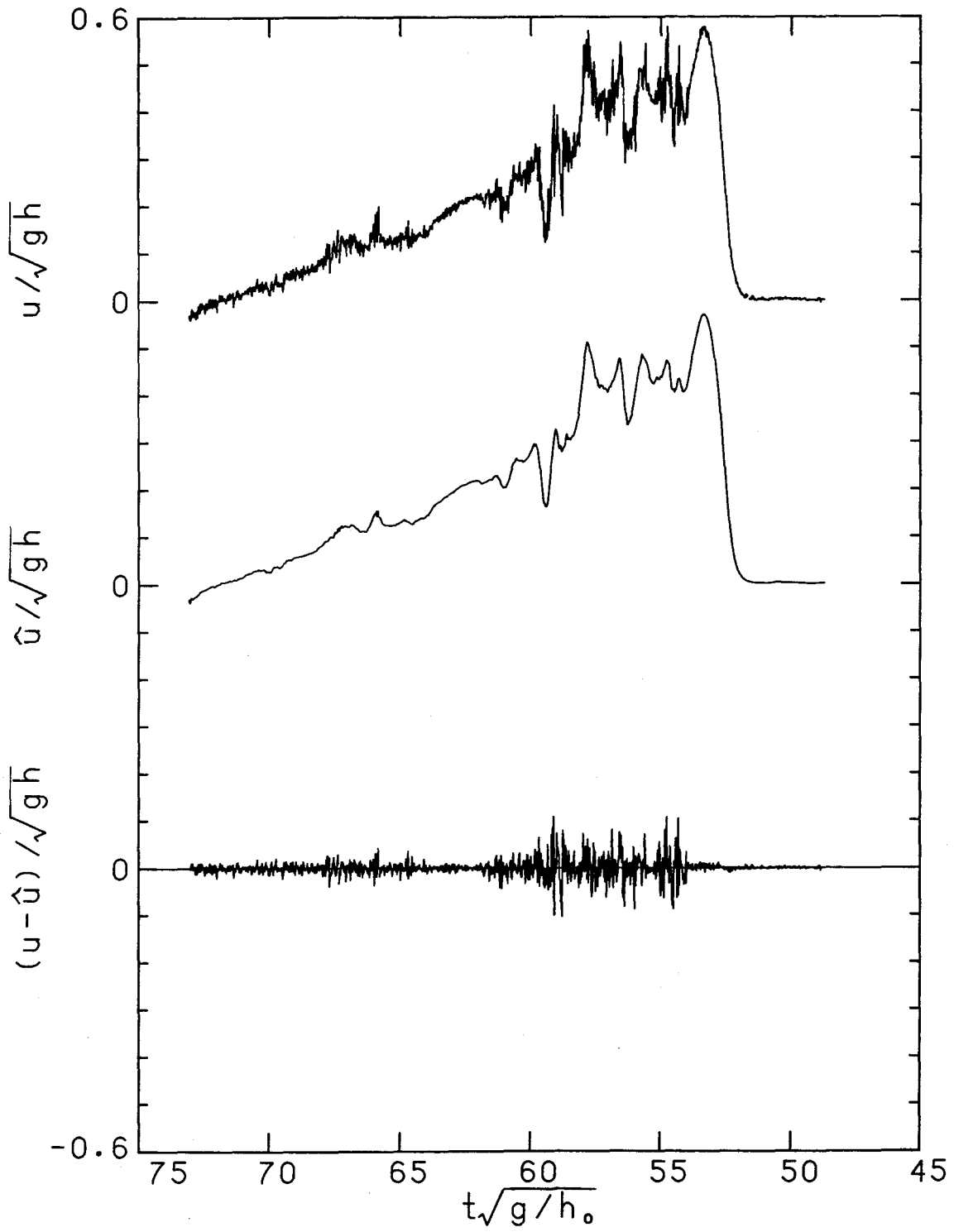


Fig. 5.28a Example of filter performance, $N_w=15$.

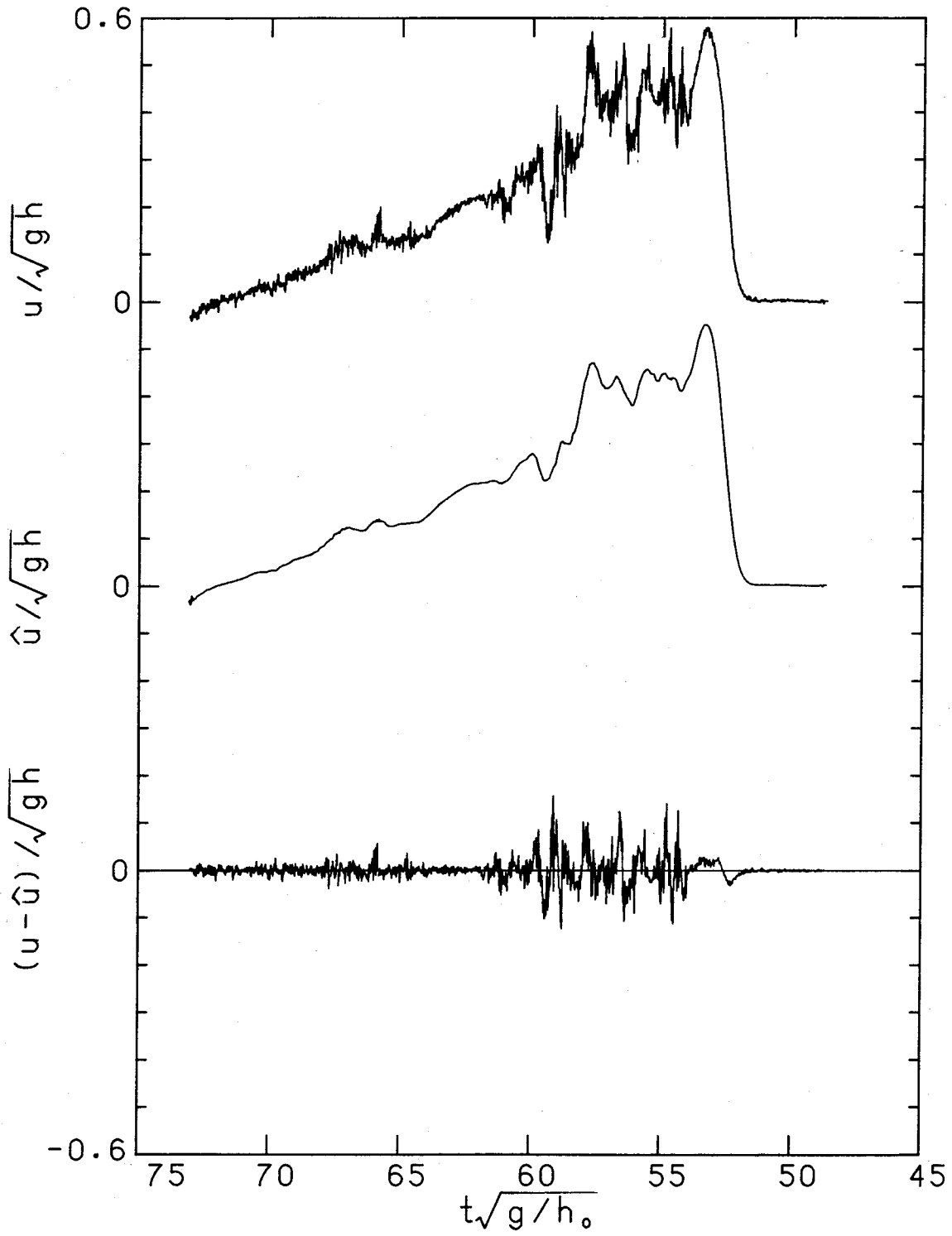


Fig. 5.28b Example of filter performance, $N_w=35$.

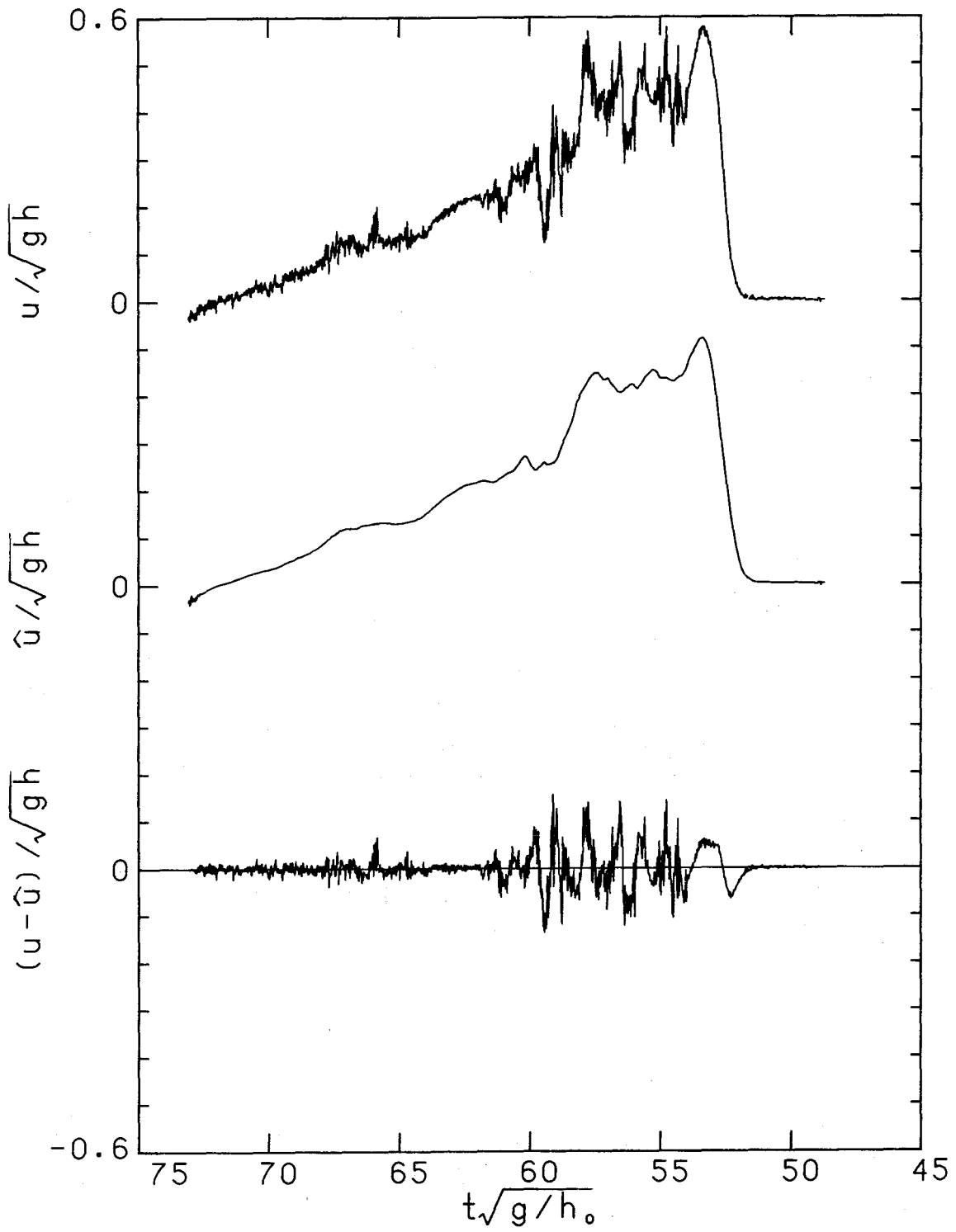


Fig. 5.28c Example of filter performance, $N_w=59$.

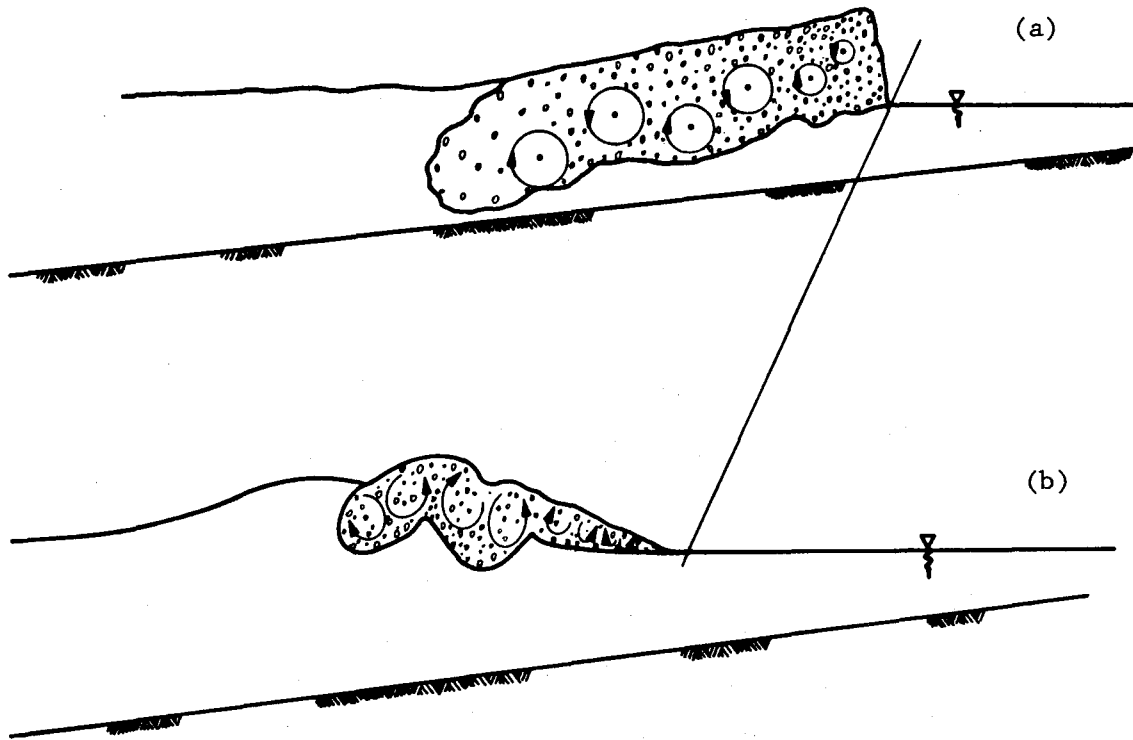


Fig. 5.29 Illustration of vortices in plunging wave after breaking; (a) quasi-steady bore, (b) early breaking.

breaking front. We really don't have much information about the vortices or the wake itself but in Fig. 5.29a we illustrate what is believed to be a possible arrangement for them, which aids the discussion to follow.

To support the existence of counter-rotating vortices, velocity measurements were made at three locations where the turbulent wake was present. The locations were chosen so that the paths taken by the

vortices would be similar to the paths shown in Fig. 5.25. Measurements made near the bottom, at mid-level, and near the surface would be expected to give results similar to those predicted from the path A-A, the path C-C, and the path B-B. To extract the fluctuations induced by the presence of the vortices in the flow, it was again necessary to, at least lowpass the velocity signals as discussed in Section 5.4.1. To also eliminate the small scale fluctuations, the signals were bandpassed with the filter described by Eq. 5.7. The filter passed frequencies in the approximate range of $0.42\sqrt{g/h_0}$ to $4.2\sqrt{g/h_0}$ (2-20 Hz).

Fig. 5.30b shows the bandpassed horizontal and vertical velocity traces which were measured at $h/h_0=0.17$ and $z/h=-0.94$. Since this location is near the bottom, we expect that the velocity vector constructed from the bandpassed velocity signal should rotate in a clockwise direction. Taking the angle ϕ to be positive in the counter-clockwise direction, we show the cumulative rotation of the velocity vector in Fig. 5.30c, and, as expected of a clockwise rotation, ϕ is seen to decrease. Note that since the cumulative angle is measured from an arbitrary initial direction, the initial magnitude is not important; the important thing is the trend in the figure.

Measurements near the surface, which were obtained at $h/h_0=0.21$ and $z/h=0.19$, are shown in Fig. 5.31. At this location, the entrained air in the flow precluded measurements until somewhat rearward of the crest. Here again, we see the expected result with the net rotation of

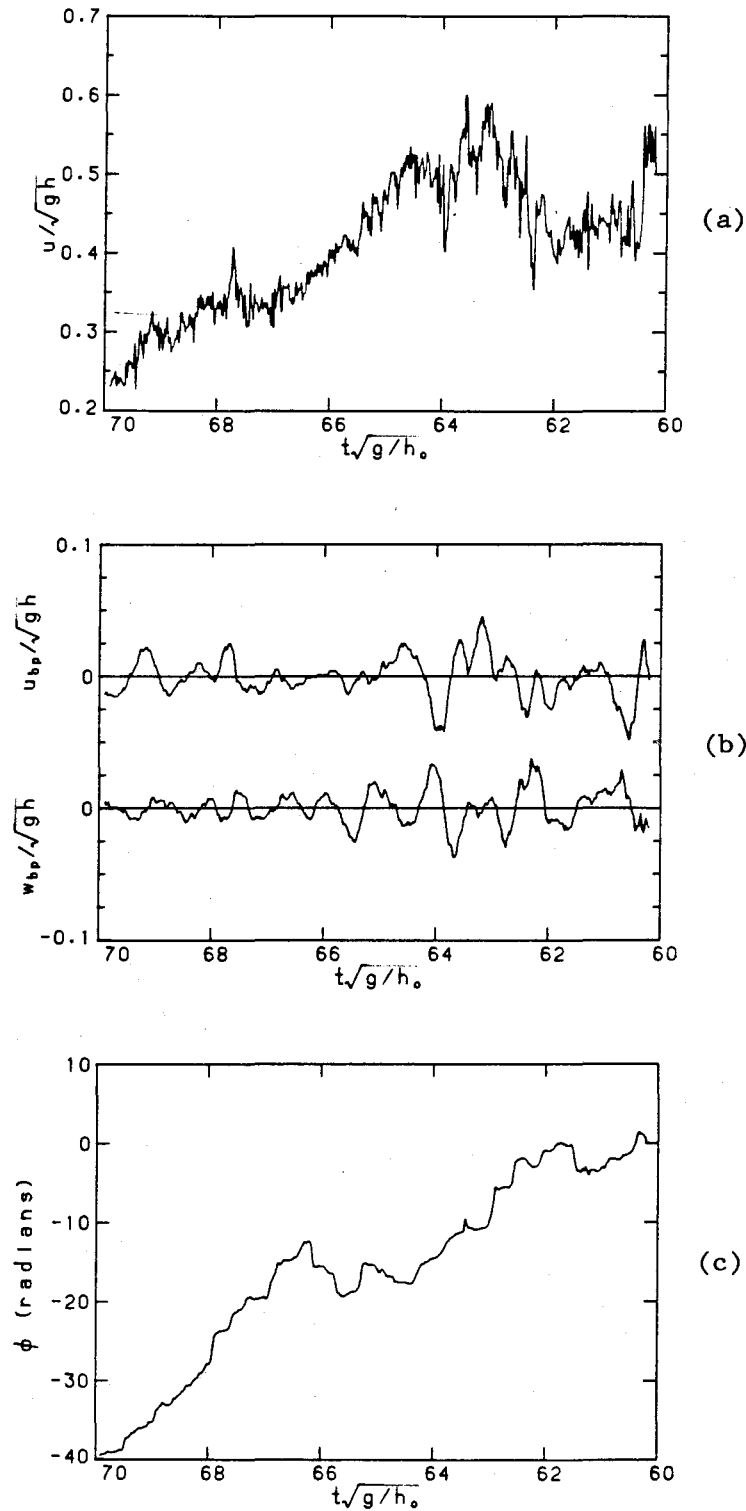


Fig. 5.30 Velocity traces in the after breaking region of the plunging wave, $h/h_0=0.17$ and $z/h=-0.94$; (a) measured horizontal velocity, (b) bandpassed horizontal and vertical velocities, (c) cumulative vector angle rotation from filtered velocity signals.

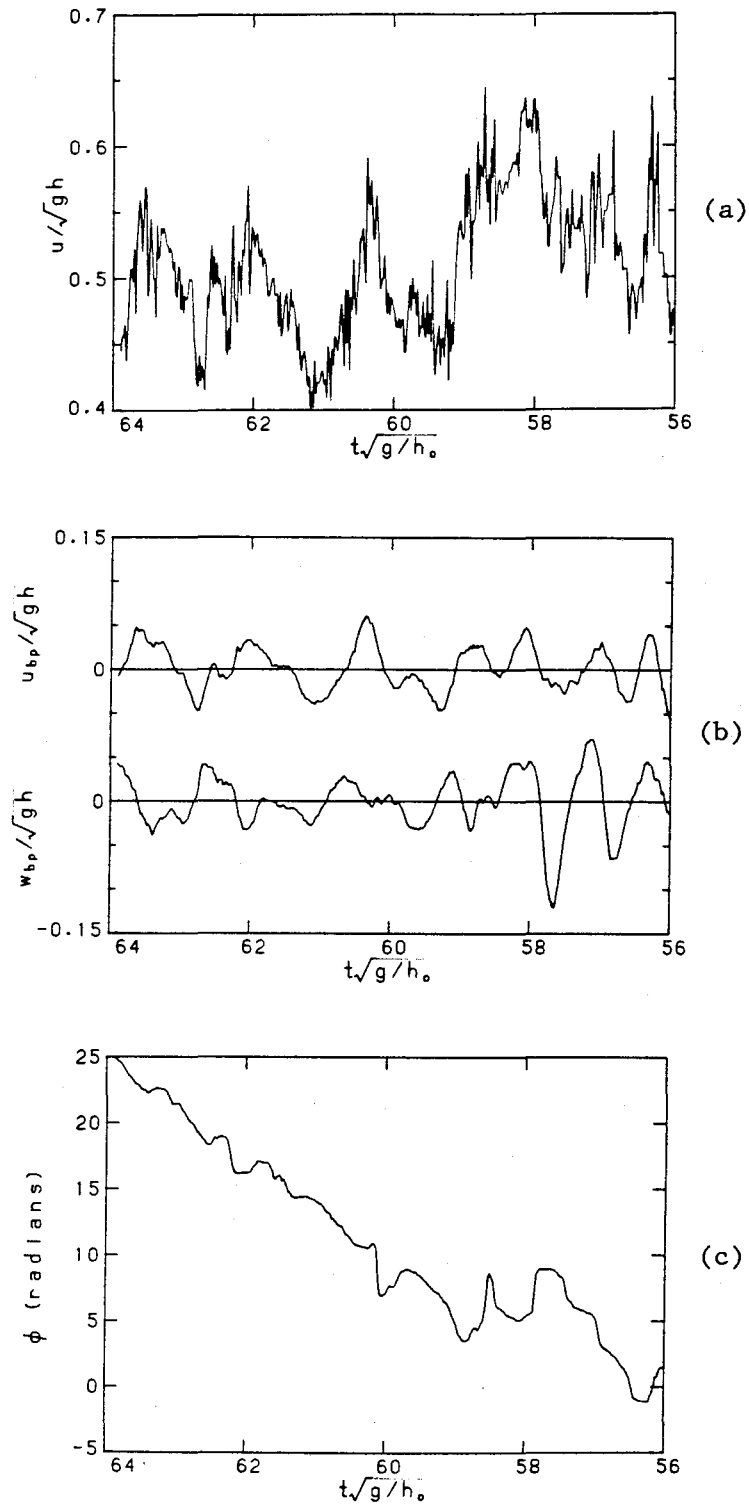


Fig. 5.31 Velocity traces in the after breaking region of the plunging wave, $h/h_0=0.21$ and $z/h=0.19$; (a) measured horizontal velocity, (b) bandpassed horizontal and vertical velocities, (c) cumulative vector angle rotation from filtered velocity signals.

the velocity vector in the counter-clockwise direction. Apparently during the duration of this signal the vortices were mostly below the point of measurement. Finally, at $h/h_0=0.21$ and $z/h=-0.52$, a mid-level measurement, the expected result is again obtained as shown in Fig. 5.32. At this point, it can be said, with some confidence, that the vortices in this wave are indeed counter-rotating.

Assuming that our hypothesis concerning the arrangement of the vortices is reasonable (i.e., along a line in the direction of wave motion), we can learn some additional information about the vortices from Figures 5.30, 5.31, and 5.32. Since the velocity vector constructed from the bandpassed signals makes one complete rotation for each vortex pair, then we can estimate the size of a vortex from the rate of change in ϕ and the mean horizontal velocity which convects the vortices forward. The size of a vortex is, then, approximated by:

$$l_v \sim \bar{u}_v \bar{t}_v \quad , \quad (5.7)$$

where \bar{u}_v is the average horizontal velocity over some time span, and \bar{t}_v is the average time for a vortex to pass the point of measurement over the same time span. Table 5.3 lists some estimates of l_v .

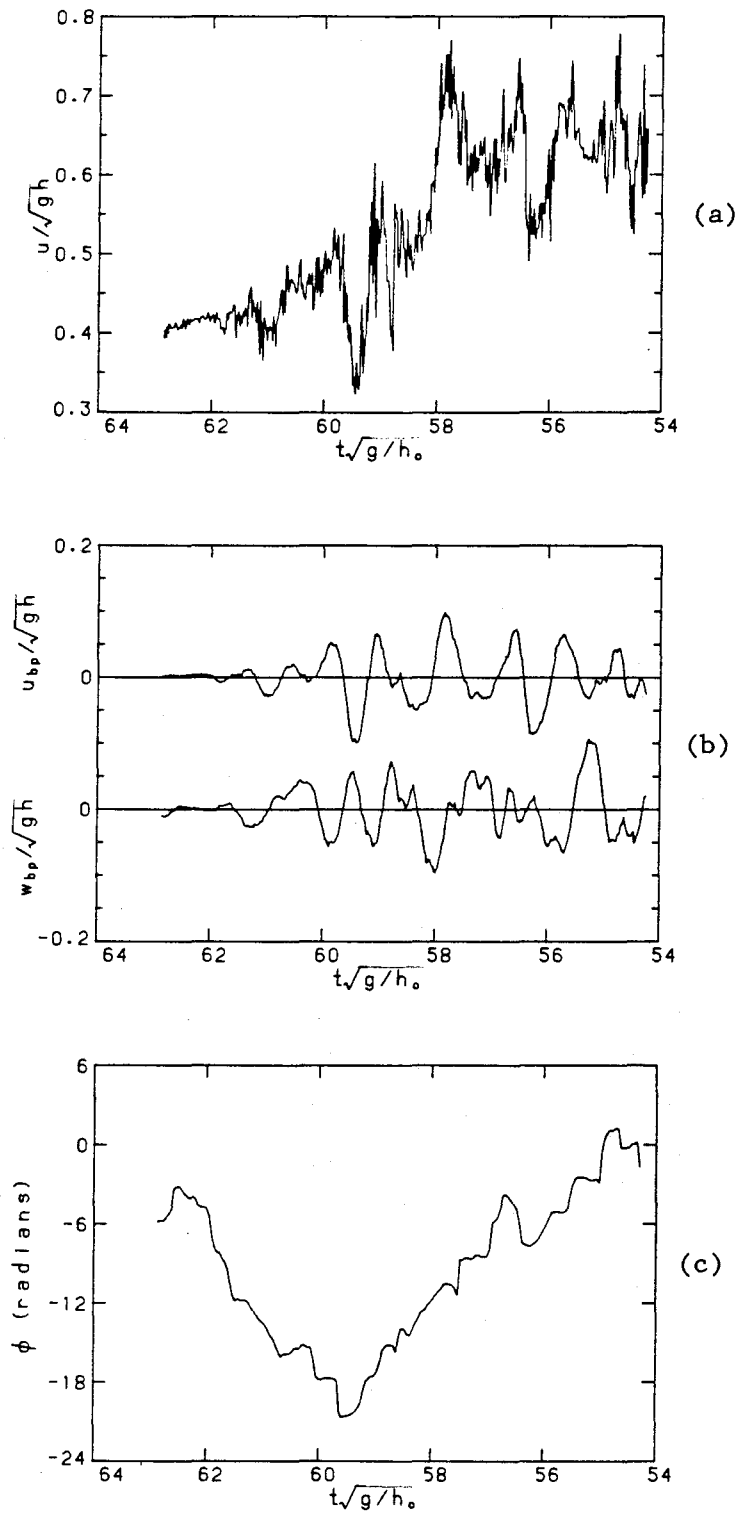


Fig. 5.32 Velocity traces in the after breaking region of the plunging wave, $h/h_0=0.21$ and $z/h=-0.54$; (a) measured horizontal velocity, (b) bandpassed horizontal and vertical velocities, (c) cumulative vector angle rotation from filtered velocity signals.

Table 5.3 Estimates of l_v

Fig.	Time range for estimate $\Delta t \sqrt{g/h_0}$	$\frac{\bar{u}_v}{\sqrt{gh}}$	$\bar{\tau}_v \sqrt{g/h_0}$	$\frac{l_v}{h_0}$
5.30	60 - 65	0.45	0.79	~ 0.15
5.31	59 - 64	0.48	0.68	~ 0.14
5.32	54 - 59	0.63	0.79	~ 0.23
5.32	60 - 62	0.42	0.62	~ 0.13

These calculations show very consistent results. These estimates for l_v indicate that the average size of the vortices is of the same order as the depth at the point of measurement. These have been the results for the plunging beaker, the measurements for the spilling case did not exhibit, in any obvious way, details of the vortices it may have contained.

5.5 Turbulent Intensities in the Wake

Velocity measurements in the ZGD, where the wave has become quasi-steady bore, show considerable variability in the wake even when made under carefully controlled conditions such as those characterizing this study. A good example of this variability is demonstrated in Fig. 5.5 which shows ten individual runs all measured at the same location $h/h_0=0.17$ and $z/h=-0.67$. The strength, number and distribution of the vortices generated from breaking are likely to be dependent on some measure of the breaking event. The subsequent

behavior of the vortices is apparently less deterministic, with their trajectories and the small scale turbulence carried with them being more random. Hence the variability we see in Fig. 5.5.

With a single point measurement, it is difficult to say much about the turbulent wake or even the mean translatory flow of the wave itself in the ZGD. The vortices can confuse the interpretation of measurements when they slow or stop translating forward. For instance, a significant velocity reading can be registered due to a stationary vortex, indicating a local flow in some direction, when there is no overall translatory flow present. More can be learned about the average flow from many repeated measurements at locations across the depth. To do this properly requires that one investigate the statistical nature of the flow at the point of interest to determine the degree of measurements needed. It is most likely to require a rather involved effort. To go along with the measurement problem is the problem of analyzing the velocity signals obtained and the appropriate representation of the turbulence in the wake.

To analyze the turbulent velocity signals we have taken the approach of Nadaoka & Kondoh (1982), who filtered the individual signals to examine the small scale turbulence. Nadaoka & Kondoh used an analog bandpass filter, while we use the digital filter, described by Eq. 5.5, to obtain the high frequencies. The filtered signal is then considered the turbulent velocity signal. It is clear from the velocity traces shown in Fig. 5.5 that the turbulent character of the

signals varies with time. It is necessary, therefore, to compute turbulence intensity over some window width. The resulting output of this process is a time series of turbulence intensity. Accounting for the gaps in the data, we find that the horizontal component of the fluctuating velocity is given by:

$$u'_{rms}(t_i) = \frac{1}{\sum_{j=-(N_t-1)/2}^{(N_t-1)/2} W[u(t_i)]} \left\{ \sum_{j=-(N_t-1)/2}^{(N_t-1)/2} [u(t_i) - \hat{u}(t_i)]^2 W[u(t_i)] \right\}^{\frac{1}{2}}, \quad (5.8)$$

where \hat{u} is the filtered horizontal velocity obtained using Eq. 5.5, and N_t is the window width used to compute the turbulence intensity. If $\Sigma W(u) = 0$ (see Equation 5.6), then u'_{rms} is considered invalid. The equivalent equation for the vertical component is obtained by replacing all occurrences of u with w . In the cases to be presented here, a window width of $1.01\sqrt{h_0/g}$ (0.21 sec) and a filter cutoff frequency of $\sim 1.5\sqrt{g/h_0}$ (7 Hz) were used. Note that the lowest frequencies in $(u - \hat{u})$ are contained within the window used. Repeated measurements at the same location were then averaged to form a single time series.

Fig. 5.33a shows the individual averaged turbulence intensity time series of the wake of the plunging wave at seven locations across the depth at $h/h_0=0.21$. The wave crest passed this location at $t\sqrt{g/h_0} \sim 53$. The maximum rms value is $0.038\sqrt{gh}$. The time series are also presented in Fig. 5.33b, using gray levels to represent the differing levels of turbulence intensity. This type of presentation facilitates the

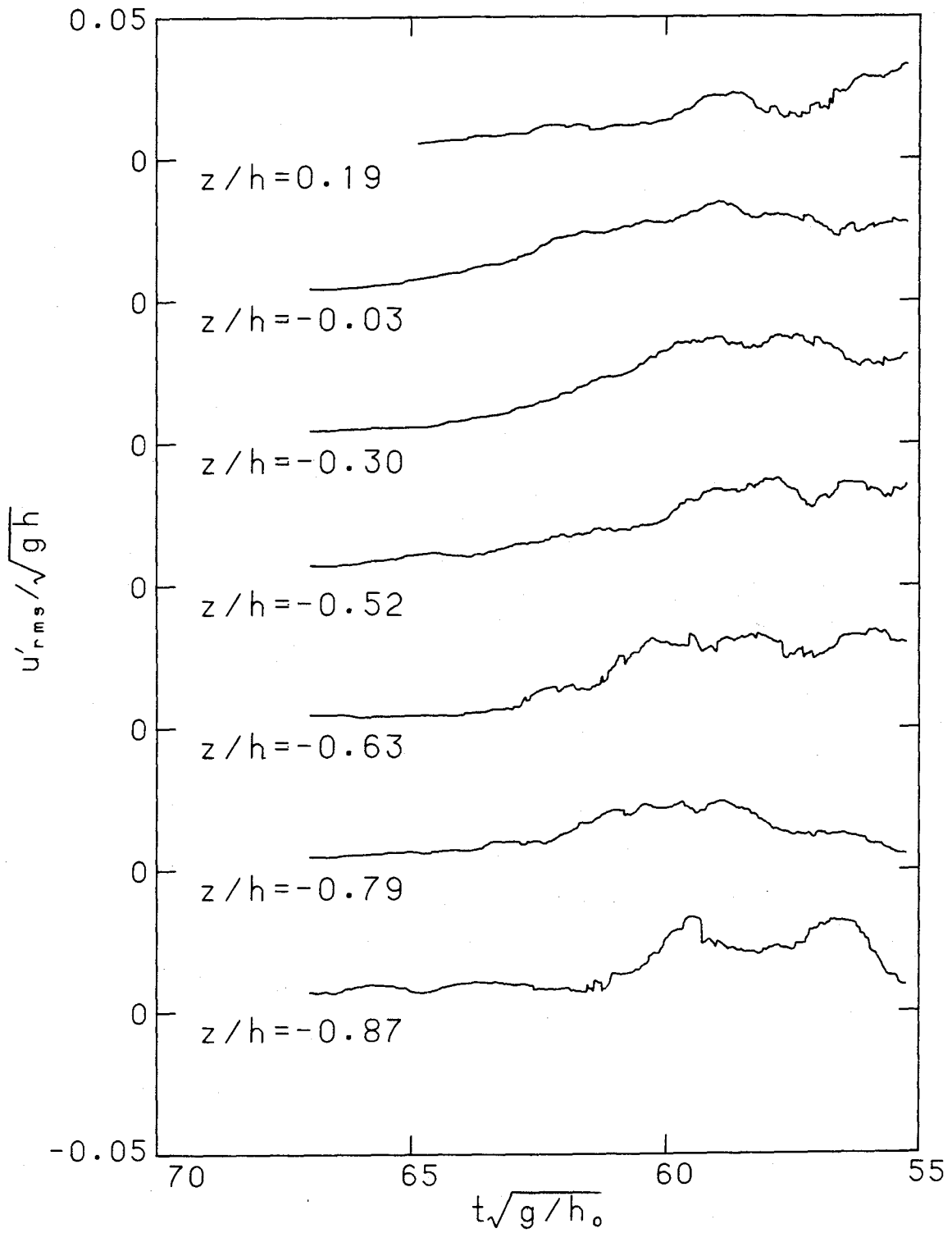


Fig. 5.33a Turbulence intensity in the wake of the plunging wave $h/h_0=0.21$, line plot representation.

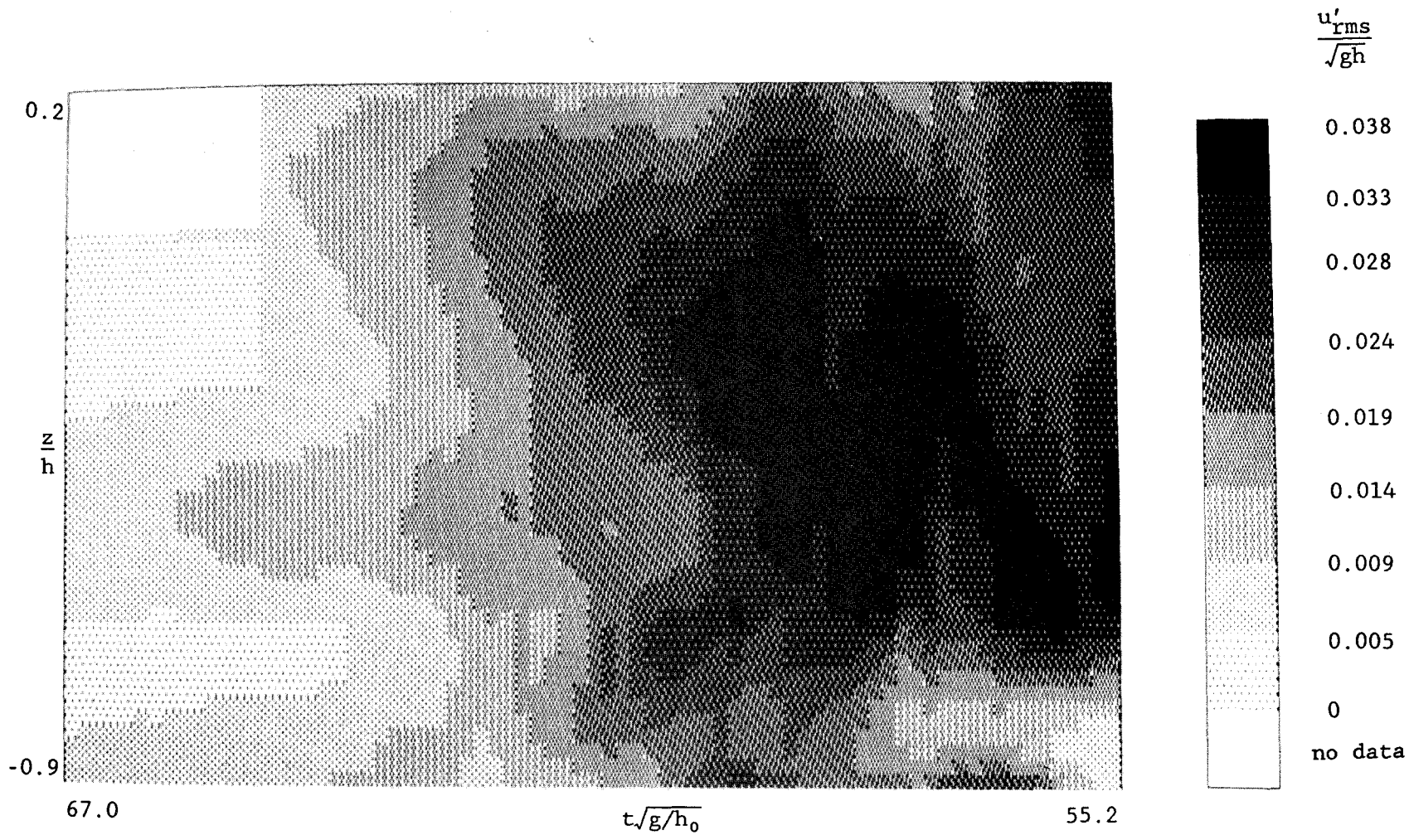


Fig. 5.33b Turbulence intensity in the wake of the plunging wave
 $h/h_0=0.21$, gray scale representation.

visualization of the turbulence intensities across the depth. The equivalent information at $h/h_0=0.19$ is presented in Fig. 5.34a and Fig. 5.34b. At this location the crest passed at $t\sqrt{g/h_0} \sim 55$ and the maximum rms value is $0.044\sqrt{gh}$. These figures indicate that a high intensity turbulent core is left behind the breaking front; the progressively decreasing turbulent intensity region behind the high intensity core is characteristic of a wake. Unlike the results presented by Battjes & Sakai (1981), here we see a region of low turbulent intensity preceding the high turbulent intensity region. Hence, the actual wake character may not be as simple as the impression one gets from looking at the results of Battjes & Sakai, at least for a plunging breaker. Instead of a continuously decreasing turbulent intensity behavior trailing behind the breaking front, there may be localized regions of high turbulent intensity, possibly vortex pairs, distributed within the wake.

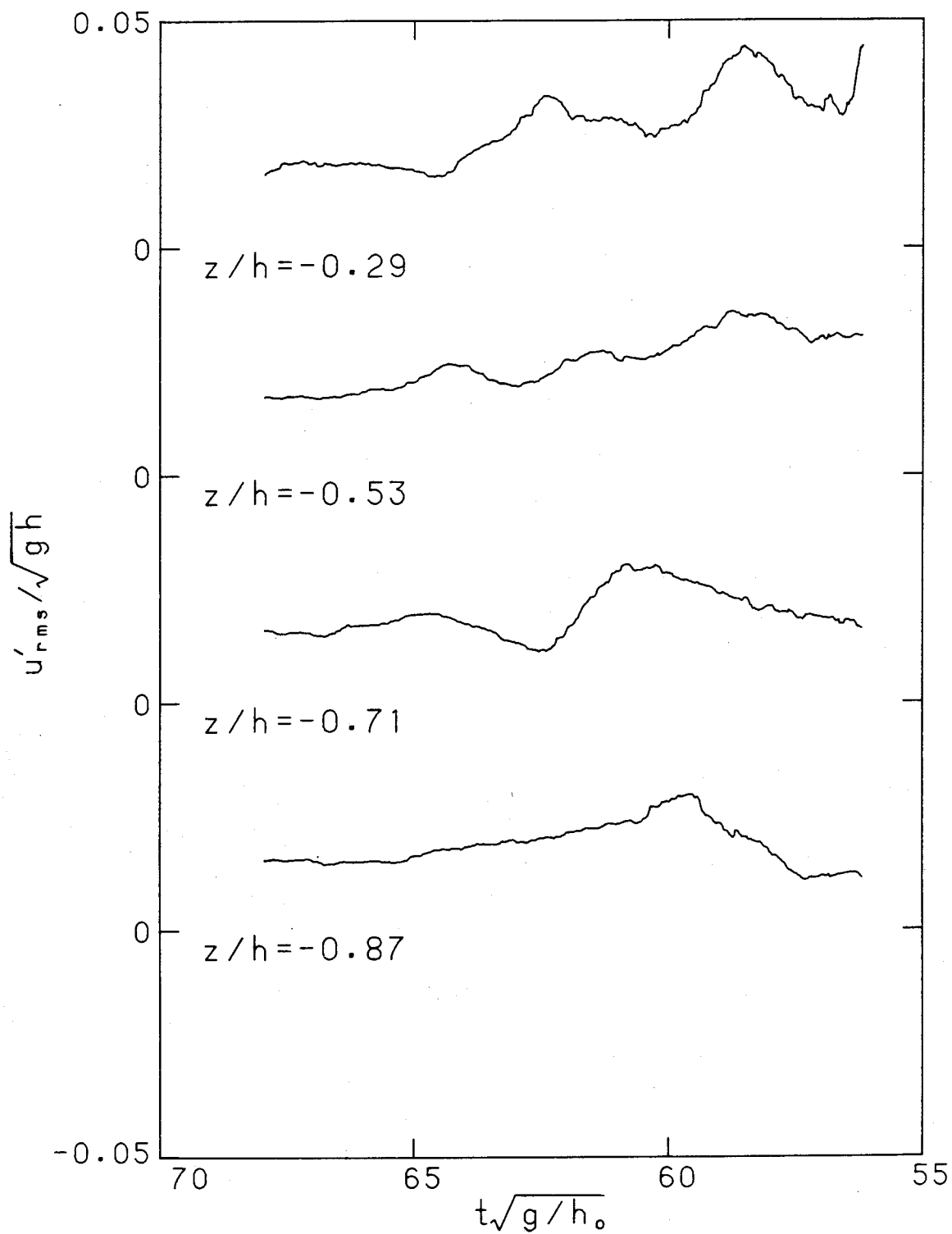


Fig. 5.34a Turbulence intensity in the wake of the plunging wave $h/h_0=0.19$, line plot representation.

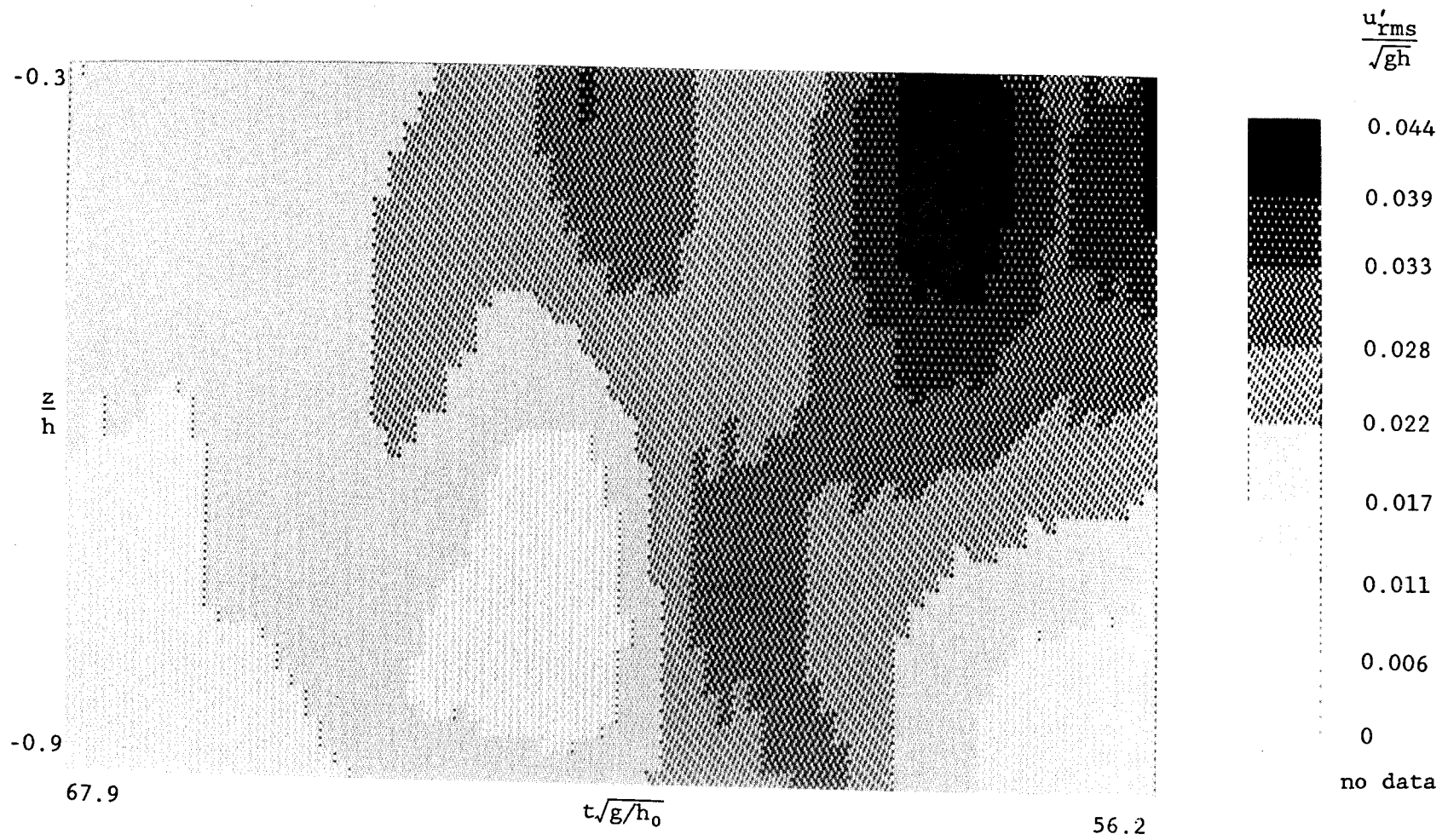


Fig. 5.34b Turbulence intensity in the wake of the plunging wave $h/h_0=0.19$, gray scale representation.

CHAPTER 6

CONCLUSIONS AND RECOMMENDATIONS FOR FURTHER STUDY

Wave breaking has been studied by use of laser Doppler velocimetry with emphasis given to the kinematics at breaking, the early breaking phase and the turbulent wake generated from breaking. Significant among the findings of this study was that no clear mechanism was found that would give rise to the initiation of breaking for the spiller considered in this study, also, the existence of counter-rotating vortices generated from breaking was established. As solitary waves were used to conduct this investigation on wave breaking, a significant contribution to the existing information on the amplitude behavior of solitary waves on beaches has been made. The LDV designed and constructed for this study, although representing nothing new in concept or principle, is unique and its configuration provides an effective means of observing flow near boundaries.

6.1 *The General Nature of the Solitary Wave*

The measurements from this study have shown that there are at least four well defined regions of the shoaling-through-breaking solitary wave on a beach. These regions have been termed according to the amplitude behavior they exhibit on the beach; they are:

- The zone of gradual shoaling.
- The zone of rapid shoaling.
- The zone of rapid decay.

- The zone of gradual decay.

The most detailed wave amplitude measurements from this study indicate that there is a definite transitional zone between the previously known $-1/4$ and -1 power laws where the wave amplitude exhibits a growth rate following a power law of $-3/5$.

6.2 *The Kinematics at Breaking*

The flows fields for the spilling and plunging breakers obtained from this study represent some of the most detailed experimental measurements of their kind. The flow field of the plunging breaker indicates that, indeed, the velocities at the crest reach the measured celerity of the wave. The flow field obtained for the spilling breaking, however, gives no clear indication that the fluid velocities at the crest reach, or exceed, the measured celerity of the wave. Additionally, the accelerations computed from the velocity field do not attain the necessary magnitude to produce a Rayleigh-Taylor instability. Nevertheless, the overall picture given by the flow fields of the plunging and spilling breakers are consistent with qualitative descriptions that have been based on theoretical results (see Peregrine 1983).

6.3 *Counter-rotating Vortices*

It apparently has always been the perceived notion that the vortices created by the breaking process are co-rotating. To this author's knowledge, the question of where the required net increase in angular momentum originates, with no apparent moments acting on the fluid, has not been explained or, for that matter, even discussed. The measurements obtained from the plunging breaker, during the early breaking phase beneath the breaking tongue and those in the turbulent wake behind the breaking front, clearly show the vortices generated from breaking to be counter-rotating and their size to be on the order of the undisturbed depth at breaking. This fact, that the vortices are counter-rotating, is certainly among the most interesting and revealing findings resulting from this study.

6.4 *The Turbulent Wake*

Use of a single point flow measurement device, such as the LDV used in this study, together with the transient nature of the breaking phenomenon, made it difficult to learn much about the turbulent wake which develops behind the breaking front, though considerable effort was directed towards this aspect of the study. The air entrainment precluded measurements in much of the flow, possibly the most interesting portions. Still, the time series of the turbulent intensities obtained show the wake nature for an actual breaker on a beach; most previous efforts in this direction have made use of breakers of uncertain character. Too little information is available

to draw any significant conclusions on the precise nature of the wake, however, it does appear that the wake of a plunging breaker has regions of high turbulent intensity distributed within it rather than there being a continuously decreasing level in the turbulent intensities behind the breaking wave front.

6.5 *Recommendations for Further Study*

It is believed that the techniques developed and the procedures implemented for this study represent an efficient and effective means of investigating the phenomena of breaking waves. Specifically the use of:

- The solitary wave together with repeated measurements.
- An LDV capable of measurements near boundaries.
- Unattended measurements via a computer controlled set-up.

Further studies directed towards the unresolved question concerning the mechanism for breaking of the spilling breaker, would require velocity measurements closer to the surface where it is sloping. This could be accomplished with an LDV similar to the one designed for this study, but with the added flexibility of optics which could be rotated so that any arbitrary surface could be approached.

Though the existence and a rough size estimate of the counter-rotating vortices has been achieved, there is still much to be explained regarding the distribution, trajectories and decay of the

vortices generated from breaking. In this area, extensive use of flow visualization is recommended with clever use of flow tracers and dye. In the wake region, where the entrained air concentration is reasonably low, qualitative and quantitative information can be continued to be obtained by LDV.

REFERENCES

- Banner, M.L. & Phillips, O.M. 1974 On the Incipient Breaking of Small Scale Waves. *J. Fluid Mech.*, **65**, 647-656.
- Bazin, H. 1865 Recherches expérimentales sur la propagation des ondes. *Mém. présentés par divers Savants à L'Acad. Sci. Inst. France* **19**, 495-644.
- Basco, D.R. 1985 A Qualitative Description of Wave Breaking. *Journal Waterway, Port, Coastal and Ocean Engineering*. ASCE. **111**, WW2, March, 171-188.
- Battjes, J.A. & Sakai, T. 1981 Velocity Field in a Steady Breaker. *J. Fluid Mech.* **111**, 421-437.
- Boussinesq, M.J. 1872 *Théorie des ondes et des remous qui se propagent le long d'un canal rectangulaire horizontal, en communiquant au liquide contenu dans ce canal des vitesses sensiblement pareilles de la surface au fond*. *J. Math. Pures Appl.* (2) **17**:55-108; transl. A. C. J. Vastano, J. C. H. Mungall, Texas A&M Univ., Ref. 76-2-T (March, 1976).
- Camfield F.E. & Street R.L. 1969 Shoaling of Solitary Waves on Small Slopes. *Journal Waterway and Harbors Division*. ASCE. **111**, WW1, February, 1-22.
- Cokelet, E.D. 1977 Breaking Waves. *Nature*, **267**, 769-774.
- Cokelet, E.D. 1979 *Breaking Waves - The Plunging Jet and the Interior Flow Field*. Mechanics of Wave Induced Forces on Cylinders. T. Shaw, Editor. Pitman, London. 379-392.
- Divoky, D., Le Méhauté, B., & Lin, A. 1970 Breaking Waves on Gentle Slopes. *Journal of Geophysical Research*. **75**, 1681-1692.
- Drain, L.E. 1980 *The Laser Doppler Technique*. John Wiley & Sons.
- Durst, F., Melling, A. & Whitelaw, J. H. 1981 *Principles and Practices of Laser-Doppler Anemometry*. Academic Press.
- Duncan, J.H. 1978 *The Dynamics of Breaking Surface Waves*. Ph.D. Thesis, John Hopkins.

- Duncan, J.H. 1981 An Experimental Investigation of Breaking Waves Produced by a Towed Hydrofoil. *Proc. R. Soc. Lond. A* 377, 331-348.
- Easson, W.J. & Greated, C.A. 1984 Breaking Wave Forces and Velocity Fields. *Coastal Engineering*, 8, 233-241.
- Flick R.E., Guza, R.T., & Inman, D.L. 1981 Elevation and Velocity Measurements of Laboratory Shoaling Waves. *Journal of Geophysical Research*. 86, 4149-4160.
- Gartrell, G. 1978 *A Signal Processor for a Laser-Doppler Velocimeter*. Tech Memo 78-5, W. M. Keck Laboratory of Hydraulics and Water Resources, California Institute of Technology, Pasadena, California.
- Galvin, C.J. 1972 Wave Breaking in Shallow Water. In *Waves on Beaches and the Resulting Sediment Transport*, ed. R.E. Meyer pp413-56. New York, Academic Press
- Goring, D.G. 1978 *Tsunamis—The Propagation of Long Waves onto a Shelf*. Ph.D. Thesis, W. M. Keck Laboratory of Hydraulics and Water Resources, California Institute of Technology, Pasadena, California.
- Hornung H.G. & Killen P. 1976 A Stationary Oblique Breaking Wave for Laboratory Testing of Surfboards. *J. Fluid Mech.* 78, 459-480.
- Ippen, A.T. & Kulin, G. 1954 The Shoaling and Breaking of the Solitary Wave. *Proc. Conf. Coastal. Eng.*, 5th, 27-49
- Ippen, A.T. & Kulin, G. 1955 *Shoaling and Breaking Characteristics of the Solitary Wave*. Hydrodynamics Laboratory, MIT Tech. Rep. 16.
- Jansen, P.C.M. 1986 Laboratory Observations of the Kinematics in the Aerated Region of Breaking Waves. *Coastal Engineering*, 9, 453-477.
- Johnson R.S. 1973 On the Development of a Solitary Wave Moving over an Uneven Bottom. *Proc. Camb. Phil. Soc.*, 73, 183-203.
- Kishi, T. & Saeki, H. 1966 The Shoaling, Breaking and Runup of the Solitary Wave on Impermeable Slopes. *Proc. Conf. Coastal Eng.*, 10th, 433-449
- Kjeldsen, S.P. & Myrhaug, D. 1980 Wave-Wave Interactions, Current-Wave Interactions and the Resulting Extreme Waves and Breaking Waves. *Proc. Conf. Coastal. Eng.*, 17th, 2277-2303.
- Knickerbocker, C.J. & Newell, A.C. 1985 Reflections from Solitary Waves in Channels of Decreasing Depth. *J. Fluid Mech.* 153, 1-16.

- Lang, D.B. 1985 *Laser Doppler Velocity and Vorticity Measurements in Turbulent Shear Layers*. Ph.D. Thesis, Graduate Aeronautical Laboratories California Institute of Technology, Pasadena, California.
- Leibovich, S. & Randall, J.D. 1973 Amplification and Decay of Long Nonlinear Waves. *J. Fluid Mech.* 53, 481-493.
- Longuet-Higgins, M.S. & Cokelet, E.D. 1976 The Deformation of Steep surface Waves on Water I. A Numerical Method of Computation. *Proc. R. Soc. Lond. A.* 350, 1-26.
- Miles, J.W. 1980 Solitary Waves. *Ann. Rev. Fluid Mech.* 12, 11-43
- Miller, R.L. 1970 The Role of Surface Tension in Breaking Waves. *Proc. Conf. Coastal Eng., 12th*, 433-449
- Miller, R.L. 1976 *The Role of Vortices in Surf Zone Prediction: Sedimentation and Wave Forces*. Soc. Econ. Paleontol. Mineralog., Spec. Publ. No. 24, 92-114
- Munk, W.H. 1949 The Solitary Wave and Its Applications to Surf Problems. *Ann. NY Acad. Sci.* 51:376-424.
- Nadaoka, K. & Kondoh, T. 1982 *Laboratory Measurements of Velocity Field Structure in the Surf Zone by LDV*. *Coastal Engineering in Japan.* 25, 125-145.
- Okoye, J.K. 1970 *Characteristics of Transverse Mixing Open Channel Flows*. Ph.D. Thesis, W. M. Keck Laboratory of Hydraulics and Water Resources, California Institute of Technology, Pasadena, California.
- Peregrine, D.H. 1967 Long Waves on a Beach, *J. Fluid Mech.* 27, 815-827.
- Peregrine, D.H. 1979 *Mechanics of Breaking Waves - A Review of Euromech 102*. Mechanics of Wave Induced Forces on Cylinders. T. Shaw, Editor. Pitman, London. 379-392.
- Peregrine, D.H. 1983 Breaking Waves on Beaches. *Ann. Rev. Fluid Mech.* 15, 149-178.
- Peregrine, D.H., Cokelet, E.D. & McIver, P. 1980 The Fluid Mechanics of a Wave Approaching Breaking. *Proc. Conf. Coastal Eng., 17th*, 512-528.
- Raichlen, F. 1965 *Wave-Induced Oscillations of Small Moored Vessels*, W.M. Keck Laboratory of Hydraulics and Water Resources, Rep. No. KH-R-10, California Institute of Technology, Pasadena, California.

- Russell, J.S. 1838 Report of the Committee on Waves. *Rep. Meet. Brit. Assoc. Adv. Sci.*, 7th, Liverpool, 1837, 417-496. London: John Murray.
- Russell, J.S. 1845 Report on Waves. *Rep. Meet. Brit. Assoc. Adv. Sci.*, 14th, York, 1844, 311-390. London: John Murray.
- Saeki, H., Hanayasu, S., Ozaki, A. & Takagi, K. 1971 The Shoaling and Run-up Height of the Solitary Wave. *Coastal Engineering in Japan*. 14, 25-42.
- SDK-85, 1978 *SDK-85 System Design Kit User's Manual*. Manual Order Number 9800451B, Intel Corporation.
- Shuto, N. 1973 Shoaling and Deformation of Non-linear Long Waves. *Coastal Engineering in Japan*. 16, 1-12.
- Shuto, N. 1974 Nonlinear Long Waves in a Channel of Variable Section. *Coastal Engineering in Japan*. 17, 1-12.
- Smyth, N.F. 1984 *Part I: Soliton on a Beach and Related Problems, Part II: Modulated Capillary Waves*. Ph.D. Thesis, California Institute of Technology, Pasadena, California.
- Stive, M.J.F. 1980 Velocity and Pressure Field of Spilling Breakers. *Proc. Conf. Coastal Eng.*, 17th, 547-566.
- Street, R.L. & Camfield, F.E. 1966 Observations and Experiments on Solitary Wave Deformation. *Proc. Conf. Coastal Eng.*, 10th, 284-301.
- Svendsen, I.A., Madsen, P.Å. & Hansen, J.B. 1978 Wave Characteristics in the Surf Zone. *Proc. Conf. Coastal Eng.*, 16th, 520-539.
- Synolakis, C.E. 1986 *Runup of Long Waves*. Ph.D. Thesis, W. M. Keck Laboratory of Hydraulics and Water Resources, California Institute of Technology, Pasadena, California.
- Thornton, E.B., Galvin, J.J., Bub, F.L. & Richardson, D.P. 1976 Kinematics of Breaking Waves. *Proc. Conf. Coastal Eng.*, 15th, 461-476.
- Van Dorn, W.G. 1978 Breaking Invariants in Shoaling Waves. *Journal of Geophysical Research*. 83, 2981-2988.
- Vanoni, V.A., Brooks, N.H. & Raichlen, F. 1967 *A 40 meter Precision Tilting Flume*. Tech Memo 67-3, W. M. Keck Laboratory of Hydraulics and Water Resources, California Institute of Technology, Pasadena, California.

Vinje, T. & Brevig, P. 1980 Breaking Waves on a Finite Water Depths. A Numerical Study. Report by The Norwegian Institute of Technology and the Norwegian Hydrodynamic Laboratories.

Yeh, H. Cummins, H.Z. 1964 Localized Fluid Flow Measurements with an He-Ne Laser Spectrometer. *Applied Physics Letters*, 4, 176-178.

LIST OF SYMBOLS

a	Shoaling(decay) parameter
C	Wave celerity
E	Total specific energy wave per unit width
g	Acceleration of gravity
G	Arbitrary time series
G_{bp}	Arbitrary time series bandpassed
\hat{G}	Arbitrary time series lowpassed
\hat{G}_j	Arbitrary time series lowpassed with $N_w=j$
h	Still water depth
h_b	Still water depth at breaking
H_b	Maximum amplitude of wave at breaking
h_o	Still water depth offshore
H_o	Initial offshore amplitude
i,j	Integers
ℓ_v	Length scale for vorticies
m,n	Integers
N_w	Window width of discrete filter
Q	Volume per unit width
S	Slope of beach
t	Time
t_i	Time at i_{th} sample

\bar{t}_v	Average time for a vortex to pass a point at speed \bar{u}_v
T	Window width for filter
u	Horizontal velocity
u'_{rms}	Turbulence intensity in horizontal velocity
\bar{u}_v	Average horizontal translating velocity of vortex
w	Vertical velocity
W	Data validity weight function
x	Horizontal coordinate
x_0	Horizontal distance from shoreline to beach toe
z	Vertical coordinate
Δt	Sample period
λ	Wavelength of sodium light, standard for optical quality
ξ	Wave plate trajectory
ξ_{max}	Maximum excursion of wave plate
ζ	Surface elevation
ζ_{max}	Maximum surface elevation
ζ_r	Amplitude of reflected wave

APPENDIX A

CONVERSION FACTORS

<i>To Convert</i>	<i>To</i>	<i>Multiply By</i>
inches (in.)	millimeters (mm)	25.400
inches (in.)	meters (m)	0.025400
foot (ft.)	meters (m)	0.304800
cubic feet (ft ³)	cubic meters (m ³)	0.028317
gallon (gal.)	cubic meters (m ³)	0.003785
pounds per square inch (psi)	megapascals (MPa)	0.006895
horsepower (hp=550 ft-lbf/s)	newton-meter per second (N·m/s)	745.700
rounds per minute (rpm)	hertz (Hz)	0.016667
gallons per minute (gpm)	cubic meters per second (m ³ /s)	0.00006309

APPENDIX B

MEASUREMENT LOCATIONS

The measurement locations are grouped according to series. A series always contains velocity measurements at a single x location. Wave gage records occur at arbitrary locations within a given series. For convenience we repeat some of the information from Table 5.1 here.

Table B.1 Wave parameters.

Case	Type of Breaker	h_0 (cm)	$\frac{H_0}{h_0}$	S
2	Spilling	27.65	0.4	0.0062
3	Plunging	43.25	0.2	0.0192

The first character of a series designation is the letter S or P, which indicates either the spilling or plunging case respectively. The next two characters of the series designation indicate the location of the LDV to the nearest meter in relation to the scale attached to the wave tank. The fourth character is a letter which makes the designation unique for series in which the first three characters are identical. The last two characters are digits identifying the a given run within a series. The wave gage positions are given at meter locations which were read from the scale attached to the wave tank. Positional information in the coordinate system used for the data presentation can

be determined from the following equation:

$$\frac{x}{h_0} = -(a + b x_w), \quad (\text{B.1})$$

where x_w is the wave gage location in meters as listed and the coefficients a and b are given in Table B.2.

Table B.2 Wave gage location coefficients.

Case	a	b
spilling	24.72	3.617
plunging	-35.11	2.312

Series: S19A

$$\frac{h}{h_0} = 0.587$$

$$\frac{x}{h_0} = -94.17$$

Run #	z/h	Wave Gages (meters)		
		1	2	3
0	-0.802			
1	-0.802			
2	-0.572			
3	-0.572			
4	-0.387			
5	-0.387			
7	-0.203			
8	-0.203			
9	-0.203			
10	-0.203			
11	-0.203			
12	-0.203			
13	-0.018			
14	-0.018			
15	-0.018			
16	0.105			
17	0.105			
18	0.105			
19	0.105			
20	0.105			
21	0.105			
22	0.105			
23	0.105			
24	0.228			
25	0.228			
26	0.228			
27	0.228			
28	0.228			
29	0.228			

Series: S19A

$$\frac{h}{h_o} = 0.587$$

$$\frac{x}{h_o} = -94.17$$

Run #	z/h	Wave Gages (meters)		
		1	2	3
30	0.228			
31	0.228			
32	0.290			
33	0.290			
34	0.290			
35	0.290			
36	0.290			
37	0.290			
38	0.290			
39	0.290			
40	0.352			
41	0.352			
42	0.352			
43	0.352			
44	0.352			
45	0.352			
46	0.352			
47	0.352			
48	0.352			
49	0.352			
50	0.352			
51	0.352			
52	0.413			
53	0.413			
54	0.413			
55	0.413			
56	0.413			
57	0.413			
58	0.413			
59	0.413			

Series: S19A

$$\frac{h}{h_0} = 0.587$$

$$\frac{x}{h_0} = -94.17$$

Run #	z/h	Wave Gages (meters)		
		1	2	3
60	0.413			
61	0.413			
62	0.413			
63	0.413			
64	0.413			
65	0.413			
66	0.413			
67	0.413			
68	0.413			
69	0.413			
70	0.413			
71	0.413			

Series: S20A

$$\frac{h}{h_0} = 0.609$$

$$\frac{x}{h_0} = -97.78$$

Run #	z/h	Wave Gages (meters)		
		1	2	3
0	-0.815	20.200		
1	-0.666	20.200		
2	-0.488	20.200		
3	-0.310	20.200		
4	-0.132			
5	-0.014			
6	0.105			
7		20.200		
8		20.200		
9		20.200		
10		20.200		
11		20.200		
12		20.200		
13		20.200		
14	0.105	22.000	16.800	
15	0.105	22.000	16.800	
16	0.224	21.800	16.600	
17	0.224	21.800	16.600	
18	0.224	21.800	16.600	
19	0.224	21.800	16.600	
20	0.342	21.600	16.400	
21	0.342	21.600	16.400	
22	0.342	21.600	16.400	
23	0.342	21.600	16.400	
24	0.342	21.600	16.400	
25	0.342	21.600	16.400	
26	0.342	21.600	16.400	
27	0.461	21.400	16.200	
28	0.461	21.400	16.200	
29	0.461	21.400	16.200	

Series: S20A

$$\frac{h}{h_o} = 0.609$$

$$\frac{x}{h_o} = -97.78$$

Run #	z/h	Wave Gages (meters)		
		1	2	3
30	0.461	21.400	16.200	
31	0.461	21.400	16.200	
32	0.461	21.400	16.200	
33	0.461	21.400	16.200	
34	0.461	21.400	16.200	
35	0.461	21.400	16.200	
36	0.461	21.400	16.200	
37	0.580	21.200	16.000	
38	0.580	21.200	16.000	
39	0.580	21.200	16.000	
40	0.580	21.200	16.000	
41	0.580	21.200	16.000	
42	0.580	21.200	16.000	
43	0.580	21.200	16.000	
44	0.580	21.200	16.000	
45	0.580	21.200	16.000	
46	0.580	21.200	16.000	

Series: S20B

$$\frac{h}{h_0} = 0.602$$

$$\frac{x}{h_0} = -95.97$$

Run #	z/h	Wave Gages (meters)		
		1	2	3
0	-0.822	19.700		
1	-0.623	19.700		
2	-0.623	19.700		
3	-0.441	19.700		
4	-0.259	19.700		
5	-0.259	19.700		
6	-0.137			
7	-0.137			
8	-0.137			
9	-0.016	15.800		
10	-0.016	15.800		
11	-0.016	15.600		
12	-0.016	15.600		
13	-0.016	15.600		
14	-0.016	15.600		
15	0.106	15.400		
16	0.106	15.400		
17	0.106	15.200		
18	0.106	15.200		
19	0.227	15.000		
20	0.227	15.000		
21	0.227	15.000		
22	0.227	15.000		
23	0.349	14.800		
24	0.349	14.800		
25	0.349	14.800		
26	0.349	14.800		
27	0.349	14.800		
28	0.349	14.800		
29	0.349	14.800		

Series: S20B

$$\frac{h}{h_0} = 0.602$$

$$\frac{x}{h_0} = -95.97$$

Run #	z/h	Wave Gages (meters)		
		1	2	3
30	0.349	14.800		
31	0.470			
32	0.470			
33	0.470			
34	0.470			
35	0.470			
36	0.470			
37	0.470			
38	0.470			
39	0.409			
40	0.409			
41	0.409			
42	0.409			
43	0.409			
44	0.409			
45	0.409			
46	0.409			

Series: S21A

$$\frac{h}{h_0} = 0.627$$

$$\frac{x}{h_0} = -111.53$$

Run #	z/h	Wave Gages (meters)		
		1	2	3
0	-0.938	36.270		21.000
1	-0.938	36.270		21.000
2	-0.780	36.270		21.000
3	-0.780	36.270		21.000
4	-0.595	36.000		21.000
5	-0.595	36.000		21.000
6	-0.422	34.000	21.000	
7	-0.422	33.750	21.000	
8	-0.249	33.750	21.000	
9	-0.249	33.750	21.000	
10	-0.134	33.500	21.000	
11	-0.018	33.000	23.800	
12	0.097	33.000	23.800	
13	0.097	32.500	20.600	
14	0.212	32.500	20.600	
15	0.270	32.000	20.400	
16	-0.249	32.000	20.400	
17	-0.307	31.500	20.200	
18	0.359	31.500	20.200	
19	0.359	31.500	20.200	
20	0.359			
21	0.359			
22	0.443	31.000	20.000	
23	0.443	31.000	20.000	
24	0.443	31.000	20.000	
25	0.559	30.500	19.800	
26	0.559	30.500	19.800	
27	0.674	30.000	19.600	
28	0.674	30.000	19.600	
29	0.732	29.500	19.400	

Series: S21A

$$\frac{h}{h_0} = 0.627$$

$$\frac{x}{h_0} = -111.53$$

Run #	z/h	Wave Gages (meters)		
		1	2	3
30	0.732	29.500	19.400	
31	0.789	29.000	19.200	
32	0.789	29.000	19.200	
33	0.097	28.500	19.000	
34	0.097	28.500	19.000	
35	0.212	28.500	19.000	
36	0.212	28.500	19.000	

Series: S21B

$$\frac{h}{h_0} = 0.609$$

$$\frac{x}{h_0} = -95.97$$

Run #	z/h	Wave Gages (meters)		
		1	2	3
0	-0.913	28.000	20.600	
1	-0.913	28.000	20.600	
2	-0.777	27.500	20.600	
3	-0.777	27.500	20.600	
4	-0.660	27.000	20.600	
5	-0.660	27.000	20.600	
6	-0.543	26.500	20.600	
7	-0.543	26.500	20.600	
8	-0.426	26.000	20.600	
9	-0.309	26.000	20.600	
10		20.600		
11		20.600		
12		20.600		
13		20.600		
14		20.600		
15		20.600		
16		20.600		
17		20.600		
18		20.600		
19		20.600		
21	-0.192	25.500	18.800	
22	-0.192	25.500	18.800	
23	-0.075	25.000	18.600	
24	0.042	25.000	18.600	
25	0.159	24.500	18.400	
26	0.159	24.500	18.400	
27	0.276	24.000	18.200	
28	0.393	24.000	18.200	
29	0.510	23.500	18.000	

Series: S21B

$$\frac{h}{h_0} = 0.609$$

$$\frac{x}{h_0} = -95.97$$

Run #	z/h	Wave Gages (meters)		
		1	2	3
30	0.510	23.500	18.000	
31	0.510	23.500	18.000	
32	0.510	23.500	18.000	
33	0.627	23.000	17.800	
34	0.627	23.000	17.800	
35	0.627	22.800	17.600	
36	0.685	22.800	17.600	
37	0.685	22.600	17.400	
38	0.685	22.600	17.400	
39	0.685	22.400	17.200	
40	0.685	22.400	17.200	
41	0.715	22.200	17.000	
42	0.715	22.200	17.000	
43	0.715	22.200	17.000	
44	0.715	22.200	17.000	
45	0.715	22.200	17.000	
46	0.715	22.200	17.000	

Series: P19A

$$\frac{h}{h_0} = 0.172$$

$$\frac{x}{h_0} = -8.818$$

Run #	z/h	Wave Gages (meters)		
		1	2	3
0	-0.912			
1	-0.912			
2	-0.912			
3	-0.912			
4	-0.912			
5	-0.912			
6	-0.912			
7	-0.912			
8	-0.912			
9	-0.912			
10	-0.674			
11	-0.674			
12	-0.674			
13	-0.674			
14	-0.674			
15	-0.674			
16	-0.674			
17	-0.674			
18	-0.674			
19	-0.674			
20	-0.472			
21	-0.472			
22	-0.472			
23	-0.472			
24	-0.472			
25	-0.472			
26	-0.472			
27	-0.472			
28	-0.472			
29	-0.472			

Series: P19A

$$\frac{h}{h_0} = 0.172$$

$$\frac{x}{h_0} = -8.818$$

Run #	z/h	Wave Gages (meters)		
		1	2	3
30	-0.472			
31	-0.472			
32	-0.472			
33	-0.472			
34	-0.472			
35	-0.472			
36	-0.472			
37	-0.472			
38	-0.472			
39	-0.472			

Series: P20A

$$\frac{h}{h_0} = 0.213$$

$$\frac{x}{h_0} = -11.13$$

Run #	z/h	Wave Gages (meters)		
		1	2	3
0	-0.874			
1	-0.874			
2	-0.874			
3	-0.874			
4	-0.790			
5	-0.790			
6	-0.790			
7	-0.790			
8	-0.790			
9	-0.790			
10	-0.790			
11	-0.790			
12	-0.790			
13	-0.790			
14	-0.627			
15	-0.627			
16	-0.627			
17	-0.627			
18	-0.627			
19	-0.627			
20	-0.627			
21	-0.627			
22	-0.627			
23	-0.627			
24	-0.519	21.000		
25	-0.519	21.000		
26	-0.519	21.000		
27	-0.519	21.000		
28	-0.519	21.000		
29	-0.519	21.000		

Series: P20A

$$\frac{h}{h_0} = 0.213$$

$$\frac{x}{h_0} = -11.13$$

Run #	z/h	Wave Gages (meters)		
		1	2	3
30	-0.519	21.000		
31	-0.519	21.000		
32	-0.302			
33	-0.302			
34	-0.302			
35	-0.302			
36	-0.302			
37	-0.302			
38	-0.302			
39	-0.302			
40	-0.302			
41	-0.302			
42	-0.031			
43	-0.031			
44	-0.031			
45	-0.031			
46	-0.031			
47	-0.031			
48	-0.031			
49	-0.031			
50	-0.031			
51	-0.031			
52	-0.031			
53	-0.031			
54	-0.031			
55	-0.031			
56	0.185			
57	0.185			
58	0.185			
59	0.185			

Series: P20A

$$\frac{h}{h_o} = 0.213$$

$$\frac{x}{h_o} = -11.13$$

Run #	z/h	Wave Gages (meters)		
		1	2	3
60	0.185			
61	0.185			
62	0.185			
63	0.185			
64	0.185			
65	0.185			
66	0.402			
67	0.402			
68	0.402			
69	0.402			
70	0.402			
71	0.402			
72	0.402			
73	0.402			

Series: P20B

$$\frac{h}{h_0} = 0.191$$

$$\frac{x}{h_0} = -9.974$$

Run #	z/h	Wave Gages (meters)		
		1	2	3
0	-0.530			
1	-0.530			
2	-0.530			
3	-0.530			
4	-0.530			
5	-0.530			
6	-0.530			
7	-0.530			
8	-0.530			
9	-0.530			
10	-0.530			
11	-0.530			
12	-0.530			
13	-0.530			
14	-0.530			
15	-0.530			
16	-0.530			
17	-0.530			
18	-0.530			
19	-0.530			
20	-0.530			
21	-0.530			
22	-0.530			
23	-0.530			
24	-0.530			
25	-0.530			
26	-0.530			
27	-0.530			
28	-0.530			
29	-0.530			

Series: P20B

$$\frac{h}{h_0} = 0.191$$

$$\frac{x}{h_0} = -9.974$$

Run #	z/h	Wave Gages (meters)		
		1	2	3
30	-0.048	22.500		
31	-0.048	22.500		
32	-0.048	22.500		
33	-0.048	22.500		
34	-0.048	22.500		
35	-0.048	22.500		
36	-0.048	22.500		
37	-0.048	22.500		
38	-0.048	22.500		
39	-0.048	22.500		
40	-0.289			
41	-0.289			
42	-0.289			
43	-0.289			
44	-0.289			
45	-0.289			
46	-0.289			
47	-0.289			
48	-0.289			
49	-0.289			

Series: P20C

$$\frac{h}{h_0} = 0.191$$

$$\frac{x}{h_0} = -9.974$$

Run #	z/h	Wave Gages (meters)		
		1	2	3
0	-0.870			
1	-0.870			
2	-0.870			
3	-0.870			
4	-0.870			
5	-0.870			
6	-0.870			
7	-0.870			
8	-0.870			
9	-0.870			
10	-0.870			
11	-0.870			
12	-0.870			
13	-0.870			
14	-0.870			
15	-0.711			
16	-0.711			
17	-0.711			
18	-0.711			
19	-0.711			
20	-0.711			
21	-0.711			
22	-0.711			
23	-0.711			
24	-0.711			

Series: P21A

$$\frac{h}{h_0} = 0.260$$

$$\frac{x}{h_0} = -13.44$$

Run #	z/h	Wave Gages (meters)		
		1	2	3
0	-0.708	34.000	26.000	
1	-0.708	34.000	26.000	
2	-0.440	33.500	25.500	
3	-0.440	33.500	25.500	
4	-0.173	33.000	25.000	
5	-0.173	33.000	25.000	
6	-0.173	33.000	25.000	
7	-0.173	33.000	25.000	
8	-0.039	32.500	24.500	
9	-0.039	32.500	24.500	
10	-0.039	32.500	24.500	
11	-0.039	32.500	24.500	
12	0.139	32.000	24.000	
13	0.139	32.000	24.000	
14	0.139	32.000	24.000	
15	0.139	32.000	24.000	
16	0.139	32.000	24.000	
17	0.139	32.000	24.000	
18	0.139	32.000	24.000	
19	0.139	32.000	24.000	
20	0.317	31.500	23.500	
21	0.317	31.500	23.500	
22	0.317	31.500	23.500	
23	0.317	31.500	23.500	
24	0.317	31.500	23.500	
25	0.317	31.500	23.500	
26	0.317	31.500	23.500	
27	0.317	31.500	23.500	
28	0.317	31.500	23.500	
29	0.317	31.500	23.500	

Series: P21A

$$\frac{h}{h_0} = 0.260$$

$$\frac{x}{h_0} = -13.44$$

Run #	z/h	Wave Gages (meters)		
		1	2	3
30	0.317	31.500	23.500	
31	0.317	31.500	23.500	
32	0.496	31.000	23.000	
33	0.496	31.000	23.000	
34	0.496	31.000	23.000	
35	0.496	31.000	23.000	
36	0.496	31.000	23.000	
37	0.496	31.000	23.000	
38	0.496	31.000	23.000	
39	0.496	31.000	23.000	

Series: P21B

$$\frac{h}{h_0} = 0.239$$

$$\frac{x}{h_0} = -12.29$$

Run #	z/h	Wave Gages (meters)		
		1	2	3
0	-0.690	29.500	20.500	
1	-0.690	29.500	20.500	
2	-0.690	29.500	20.500	
3	-0.690	29.500	20.500	
4	-0.690	29.500	20.500	
5	-0.690	29.500	20.500	
6	-0.690	29.500	20.500	
7	-0.690	29.500	20.500	
8	-0.690	29.500	20.500	
9	-0.690	29.500	20.500	
10	-0.690	29.500	20.500	
11	-0.690	29.500	20.500	
12	-0.530	29.000		
13	-0.530	29.000		
14	-0.530	29.000		
15	-0.530	29.000		
16	-0.530	29.000		
17	-0.530	29.000		
18	-0.530	29.000		
19	-0.530	29.000		
20	-0.530	29.000		
21	-0.530	29.000		
22	-0.530	29.000		
23	-0.530	29.000		
24	-0.337	28.500	20.500	
25	-0.337	28.500	20.500	
26	-0.337	28.500	20.500	
27	-0.337	28.500	20.500	
28	-0.337	28.500	20.500	
29	-0.337	28.500	20.500	

Series: P21B

$$\frac{h}{h_o} = 0.239$$

$$\frac{x}{h_o} = -12.29$$

Run #	z/h	Wave Gages (meters)		
		1	2	3
30	-0.337	28.500	20.500	
31	-0.337	28.500	20.500	
32	-0.337	28.500	20.500	
33	-0.337	28.500		
34	-0.144	28.000	20.500	
35	-0.144	28.000		
36	-0.144	28.000		
37	-0.144	28.000		
38	-0.144	28.000		
39	-0.144	28.000		
40	-0.144	28.000	20.500	
41	-0.144	28.000	20.500	
42	-0.144	28.000	20.500	
43	-0.144	28.000	20.500	
44	0.146	27.500	20.500	
45	0.146	27.500	20.500	
46	0.146	27.500	20.500	
47	0.146	27.500	20.500	
48	0.146	27.500	20.500	
49	0.146	27.500	20.500	
50	0.146	27.500	20.500	
51	0.146		20.500	
52	0.146		20.500	
53	0.146		20.500	
54	0.339	27.000	20.500	
55	0.339	27.000	20.500	
56	0.339	27.000	20.500	
57	0.339	27.000	20.500	
58	0.339	27.000	20.500	
59	0.339	27.000	20.500	

Series: P21B

$$\frac{h}{h_o} = 0.239$$

$$\frac{x}{h_o} = -12.29$$

Run #	z/h	Wave Gages (meters)		
		1	2	3
60	0.339	27.000	20.500	
61	0.339	27.000	20.500	
62	0.339	27.000	20.500	
63	0.339	27.000	20.500	

Series: P21C

$$\frac{h}{h_0} = 0.239$$

$$\frac{x}{h_0} = -12.29$$

Run #	z/h	Wave Gages (meters)		
		1	2	3
0	-0.338	20.500		
1	-0.338	20.500		
2	-0.338	20.500		
3	-0.338	20.500		
4	-0.338	20.500		
5	-0.338	20.500		
6	-0.338	20.500		
7	-0.338	20.500		
8	-0.338	20.500		
9	-0.338	20.500		
10	-0.338	20.500		
11	-0.338	20.500		
12	-0.338	20.500		
13	-0.338	20.500		
14	-0.338	20.500		
15	-0.338	20.500		
16	-0.338	20.500		
17	-0.338	20.500		
18	-0.338	20.500		
19	-0.338	20.500		
20	-0.338	20.500		
21	-0.338	20.500		
22	-0.338	20.500		
23	-0.338	20.500		
24	-0.338	20.500		
25	-0.338	20.500		
26	-0.338	20.500		
27	-0.338	20.500		
28	-0.338	20.500		
29	-0.338	20.500		

Series: P21C

$$\frac{h}{h_0} = 0.239$$

$$\frac{x}{h_0} = -12.29$$

Run #	z/h	Wave Gages (meters)		
		1	2	3
30	-0.338	20.500		
31	-0.338	20.500		
32	-0.338	20.500		
33	-0.338	20.500		
34	-0.338	20.500		
35	-0.338	20.500		
36	-0.338	20.500		
37	-0.338	20.500		
38	-0.338	20.500		
39	-0.338	20.500		
40	-0.338	20.500		
41	-0.338	20.500		
42	-0.338	20.500		
43	-0.338	20.500		
44	-0.338	20.500		
45	-0.338	20.500		
46	-0.338	20.500		
47	-0.338	20.500		
48	-0.338	20.500		
49	-0.338	20.500		
50	-0.338	20.500		
51	-0.338	20.500		
52	-0.338	20.500		
53	-0.338	20.500		
54	-0.338	20.500		
55	-0.338	20.500		
56	-0.338	20.500		
57	-0.338	20.500		
58	-0.338	20.500		
59	-0.338	20.500		

Series: P21D

$$\frac{h}{h_o} = 0.248$$

$$\frac{x}{h_o} = -12.86$$

Run #	z/h	Wave Gages (meters)		
		1	2	3
1	-0.689			
2	-0.689			
3	-0.689			
4	-0.689			
5	-0.689			
6	-0.508			
7	-0.508			
8	-0.508			
9	-0.508			
10	-0.508			
11	-0.508			
12	-0.322			
13	-0.322			
14	-0.322			
15	-0.322			
16	-0.322			
17	-0.322			
18	-0.322			
19	-0.322			
20	-0.229			
21	-0.229			
22	-0.229			
23	-0.229			
24	-0.229			
25	-0.229			
26	-0.229			
27	-0.229			
28	-0.229			
29	-0.229			

Series: P21D

$$\frac{h}{h_0} = 0.248$$

$$\frac{x}{h_0} = -12.86$$

Run #	z/h	Wave Gages (meters)		
		1	2	3
30	-0.136			
31	-0.136			
32	-0.136			
33	-0.136			
34	-0.136			
35	-0.136			
36	-0.136			
37	-0.136			
38	-0.136			
39	-0.136			
40	-0.043			
41	-0.043			
42	-0.043			
43	-0.043			
44	-0.043			
45	-0.043			
46	-0.043			
47	-0.043			
48	-0.043			
49	-0.043			
50	0.143			
51	0.143			
52	0.143			
53	0.143			
54	0.143			
55	0.143			
56	0.143			
57	0.143			
58	0.143			
59	0.143			

Series: P21D

$$\frac{h}{h_0} = 0.248$$

$$\frac{x}{h_0} = -12.86$$

Run #	z/h	Wave Gages (meters)		
		1	2	3
60	0.330			
61	0.330			
62	0.330			
63	0.330			
64	0.330			
65	0.330			
66	0.330			
67	0.330			
68	0.330			
69	0.330			
70	0.330			
71	0.236			
72	0.236			
73	0.236			
74	0.236			
75	0.236			
76	0.236			
77	0.236			
78	0.236			
79	0.236			
80	0.236			

Series: P22A

$$\frac{h}{h_0} = 0.310$$

$$\frac{x}{h_0} = -15.87$$

Run #	z/h	Wave Gages (meters)		
		1	2	3
0	-0.755	22.050		
1	-0.755	22.050		
2	-0.632	22.050		
3	-0.632	22.050		
4	-0.483	22.100		
5	-0.483	22.100		
6	-0.334	22.200		
7	-0.334	22.200		
8	-0.184	22.300		
9	-0.184	22.300		
10	-0.035	22.300		
11	-0.035	22.300		
12	-0.035	22.300		
13	-0.035	22.300		
14	0.114	22.400		
15	0.114	22.400		
16	0.263	22.500		
17	0.263	22.500		
18	0.413			
19	0.413			
20	0.562			
21	0.562			
22	0.562			
23	0.562			
24	0.711			
25	0.711			
26	0.860			
27	0.860			
28	1.010			
29	1.010			

Series: P22A

$$\frac{h}{h_0} = 0.310$$

$$\frac{x}{h_0} = -15.87$$

Run #	z/h	Wave Gages (meters)		
		1	2	3
30	1.010			
31	1.010			
32	1.084			
33	1.084			
34	1.084			
35	1.084			
36	1.084			
37	1.084			